LBL-36078
UC-406

REFLECTIVE MASKS FOR EXTREME ULTRAVIOLET LITHOGRAPHY

KHANG BAO NGUYEN
Ph.D. Thesis

ELECTRICAL ENGINEERING AND COMPUTER SCIENCES DEPARTMENT
University of California

MATERIALS SCIENCES DIVISION
Lawrence Berkeley Laboratory
University of California
Berkeley, CA 94720

MAY 1994

This work was supported by the Director, Office of Energy Research, Office of Basic Sciences, Materials Sciences Division, of the U.S. Department of Energy under Contract No. DE-AC03-76SF00098.

DISCLAIMER

DISCLAIMER

Portions of this document may be illegible in electronic image products. Images are produced from the best available original document.

Reflective Masks for Extreme Ultraviolet Lithography

by

Khanh Bao Nguyen

B. S. (California Institute of Technology) 1987
M. S. (University of California at Berkeley) 1990

A dissertation submitted in partial satisfaction of the
requirements for the degree of
Doctor of Philosophy

in

Engineering – Electrical Engineering and Computer Sciences

in the

GRADUATE DIVISION
of the
UNIVERSITY of CALIFORNIA at BERKELEY

Committee in charge:

Professor David T. Attwood, Chair
Professor T. K. Gustafson
Professor Andrew R. Neureuther
Professor Roger W. Falcone

1994

Reflective Masks for Extreme Ultraviolet Lithography

by

Khanh Bao Nguyen

Abstract

Reflective Masks for Extreme Ultraviolet Lithography

by

Khanh Bao Nguyen

Doctor of Philosophy in Engineering –
Electrical Engineering and Computer Sciences

University of California at Berkeley
Professor David T. Attwood, Chair

Extreme ultraviolet lithographic masks are made by patterning multilayer reflective coatings with high normal incidence reflectivity. Masks can be patterned by depositing a patterned absorber layer above the coating or by etching the pattern directly into the coating itself. Electromagnetic simulations carried out as a part of this thesis research showed that absorber-overlayer masks have superior imaging characteristics compared to etched masks. Images of absorber masks are less sensitive to variations in incident angles and pattern profiles compared to those of their etched counterparts.

In an EUVL absorber overlayer mask, defects can occur on the mask substrate, in the reflective coating, and in the absorber pattern. Electromagnetic simulations showed that substrate defects cause the most severe image degradation. To validate the simulation results, a printability study of substrate defects for absorber overlayer masks was conducted. Results showed that the printability of 25 nm high substrate defects are roughly comparable to that of defects in optical lithography.

Simulations also indicated that the manners in which the defects are covered by multilayer reflective coatings can have very significant effects on their printabilities. Coverage profiles that result in large lateral spreading of defect geometries amplify the printability of the defects by increasing their effective sizes.

The coverage profiles of Mo/Si coatings deposited above programmed defects of different sizes were studied by atomic force microscopy and transmission electron microscopy. Results showed that the lateral spreading of the defect geometry is proportional to the defect's height. The presence of undercut at the edges of the defects also increases the magnitude of the lateral spreading. Reductions in defect heights were observed for 0.15 μm wide defect lines.

A long-term study of Mo/Si coating reflectivity revealed that Mo/Si coatings with Mo as the top layer suffer significant reductions in reflectivity over time. The cause of this was determined to be oxidation of the top Mo layer. Fortunately, it was also found that the high reflectivity can be maintained by simply having Si as the top layer of the multilayer coating.

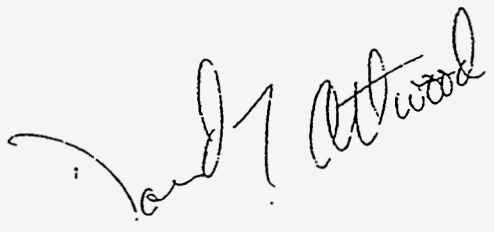

To
my parents,

Kính tặng bố mẹ,

Công cha như núi Thái Sơn,
Nghĩa mẹ như nước trong nguồn chảy ra.

Table of Contents

Acknowledgments

At the completion of this thesis, I can now look back and try to thank all those who have made this possible. I will try to express my gratitude, but it is my hope that, in the coming years, I will be able to express my appreciations in deeds, for words are often too feeble for the task.

I feel fortunate to have been guided through my graduate years by Dr. T. K. Gustafson and Dr. David Attwood. Their kindness and patience smoothed over the rough moments in my time at Cal. My graduate career began in optical neural networks and finished in lithography. All the while, Prof. T. K. Gustafson encouraged me to pursue my own interests and was supportive my choices.

In the three years that we worked together, I learnt many things from Prof. Attwood, among them the importance of asking the right questions, of focusing one's effort on the appropriate problems, and of communicating the results effectively. I appreciate his constant concern for my progress, and for providing me with an environment that encouraged my growth as a researcher. I am also indebted to him for his time and efforts in carefully going over my thesis and helping me to whip it into shape.

Professor Andrew Neureuther was always generous with his time. His energy was an inspiration and his influence on my research was most significant. Indeed, my interest in studying mask defects began with his analogy of "the Princess and the Pea."

Through Professor Neureuther, I had the opportunity to meet Michael Yeung and Alfred Wong, two graduate students who were instrumental to my thesis research. Michael was a patient source of answers for my questions on electromagnetic simulations. Alfred was the author of the current version of TEMPEST and later became a teammate in an always-contending intramural basketball team.

I would like to express my thanks to Professors Roger Falcone and William Oldham for serving on my committee and for reading my thesis. The perspectives they provided and the advices they gave were invaluable to my progress. I am also grateful to Professor Jeffrey Bokor for his encouragements and his continuing interest in my work.

A large part of my thesis research involved the study of multilayer reflective coatings. This work was possible only thanks to the generosity of the multilayer research group at the Center for X-ray Optics at the Lawrence Berkeley Laboratories. I am grateful for the help that James Underwood and Jeff Kortright have provided me during the course of my studies. My thanks also go to Eric Gullikson for his time and patience in showing me the workings of the reflectometer. Much of my work would have been impossible with that wonderful tool. The technical support provided by Paul Denham was instrumental. His help allowed me to complete my numerous depositions in a timely manner, and his experiences enabled me to understand the real workings of the sputtering chamber.

I am also indebted to Eric Anderson for providing many e-beam patterned samples under short notice, to Larry Muray for the SEM training, to Frank Ogletree for AFM training, and to Tai D. Nguyen for TEM and many useful discussions on multilayer coatings.

I am grateful for the many happy memories during my time at LBL, and for them I have many to thank – Pat Butler, Mary Holloway, Eric Essman, and of course my fellow graduate students and dining companions – Raul Beguiristain, Ken Goldberg, Xiang Lu, Tai Nguyen, Sharon Oh, Marybeth Rice, Regina Soufli, Simonetta Turek, Chris Walton, and Max Wei.

Special thanks are owed to my Japanese colleagues whose generosity made possible the experiments reported in chapter 6 – Dr. Hiroo Kinoshita, Tsuneyuki Haga, Tsutomu Mizota from NTT. Their gracious hospitality made my visit to Japan into one of the happiest and memorable occasions in my graduate career.

This thesis, of course, is only the latest step in a continuing academic pursuit that began with the support and encouragements of my parents. It is to them that this work is dedicated. They are my foundation, and no mere words can ever express my gratitude for their faith in me. I can only hope that they will be able to derive some happiness from my continuing efforts.

In addition to my parents, my sisters Kim and Lisa, with their love and care, have sustained me through my thesis years. Thank you, Kim, for the back-to-school clothes, the red–pockets, the numerous care packages. Years from now, I hope that you will look back and remember that these words were written just prior to birth of your first child, and I hope that I will have been as good an uncle as you are an older sister. To Lisa, my younger sister, my sometimes-confidante and fashion consultant, your affection made home a warmer place. I am glad that we have grown closer as we grow up. Best wishes in your academic pursuits.

For the past two years, my aunt's family have been my home-away-from-home. Their place was my haven from the exciting but sometimes exhausting environment of Berkeley. Thank you, bac Anh, anh Vuong, chi Thanh, chi Trang, Richard, anh Tuan, chi Truc, and Be, Xi, be Ri and Bin.

Of course, no scientific graduate career is complete without many long, late nights spent in front of a computer screen or in a cold laboratory with noisy machineries. During these nights, I look forward to nothing more than a long distance phone call from San Diego. Thank you, Thanh, for always being there. Your voice across that cold telephone line was my sustenance. I regret that I am not more eloquent. There is a poem here somewhere, but I am afraid I have lost it under all these equations.

Introduction

Lithography has been a major enabling technology for the advances in semiconductor manufacturing for the past 20 years. Lithography determines the minimum feature size on a chip, thereby affecting the packing density and speed of the devices on it. Innovations in lithography have allowed the wiring ground rule to be reduced by a factor of $\sqrt{2}$ approximately every three years. This capability, together with clever device engineering and circuit layout, has lead to the quadrupling of memory capacity with each new generation of semiconductor circuits.

During this period, optical lithography has been the industry's technology of choice and is expected to remain so through at least the 0.25 μm-design-rule generation[1]. Industry roadmaps project production starts for circuits with 0.18 μm minimum feature size between the years 2001 and 2004 and for those with 0.12 μm minimum feature size between the years 2004 and 2008 [1, 2]. With enhancement techniques such as phase-shifting masks and off-axis illumination, optical/deep ultraviolet (DUV) lithography may be extendible to the 0.18 μm design rule [3, 4]. For the 0.12 μm design rule and beyond, however, a new lithographic technique is expected to emerge as the dominant technology.

Among the lithographic candidates for the 0.12 μm generation are proximity x-ray lithography (PXRL) [5], electron beam lithography (cell-projection and SCALPEL) [6-8], and ion beam lithography [9, 10]. In the last few years, advances in x-ray optical technology have enabled high resolution imaging at soft x-ray and EUV wavelengths [11]. The ability to perform diffraction limited imaging at EUV wavelengths has

presented a new candidate for 100 nm lithography and beyond — extreme ultraviolet lithography (EUVL). EUVL is a reduction imaging technique that uses reflective optics and masks that are coated with multilayer reflective coatings. Reduction imaging eases the requirements on the e-beam mask writing tools. In addition, the reflective mask fabricated on a thick substrate, is a significant advantage for EUVL. Masks on thick substrates should be less susceptible to distortion, thus making wafer level overlay more manageable.

While the reflective mask on a thick substrate promises better wafer level overlay and less stringent requirements on the mask writing tools, it also poses many questions that must be answered. An EUVL mask is made by patterning a multilayer reflective coating with high normal incidence reflectivity. While Mo/Si multilayer reflective coatings with 63% reflectivity can be routinely deposited, coatings on EUVL optics and masks must maintain their high reflectivities over long operating lifetimes. A study carried out in the course of this thesis research showed that Mo/Si coatings with Mo as the top layer suffer significant reduction in reflectivities over time. The cause for this was determined to be oxidation of the top Mo layer. Fortunately, it was also found that the high reflectivity can be maintained by simply having Si as the top layer of the coating. The results of this study are reported in chapter 3.

It is also possible that imperfections in the mask patterning process and the final topographies of the masks can have significant effects on the resulting images. Masks can be patterned by depositing a patterned absorber layer above the coating or by etching a pattern directly into the coating itself. This can be done either by wet etching or by reactive ion etching (RIE). Absorber overlayer masks can also be patterned by lift-off. With any patterning technique, however, some variations in the absorber profiles may occur, thus affecting the imaging characteristics of the mask. For absorber overlayer masks, the images may also vary for different absorber materials and absorber thicknesses. In addition, since the absorber layers and the etched multilayer coatings have finite thicknesses, shadowing effects may also cause the aerial images to vary for different incident angles. Initial imaging experiments have shown that both types of masks can be imaged to 0.1 μm resolution. However, experiments have not been able to discern more subtle effects that may arise from patterning imperfections and mask topographies.

In order to answer some of these questions, electromagnetic simulation was used to study how the aerial images of absorber overlayer masks and etched masks vary with incident

angles, absorber profiles and etched stack profiles. The effects of different absorber materials and thicknesses were also studied. The results, described in chapter 2, showed that images from absorber overlayer masks are insensitive to variations in incident angles and absorber profiles. Images from etched masks, however, were found to be quite sensitive to these variations.

Since masks must be free of printable defects, the capability to inspect and repair mask defects are important for any mask technology. In order to determine the requirements for defect inspection and repair, printability studies are usually conducted to provide information on the magnitude of linewidth variations caused by defects of different sizes.

To this end, a printability study of EUVL mask defects for absorber overlayer masks was conducted in the course this thesis research. In an EUVL absorber overlayer mask, defects can occur on the substrate, in the reflective coating, and in the absorber pattern. Absorber defects can be repaired by ion-beam processes [12]. However, there is no repair technique for substrate and coating defects. In addition, electromagnetic simulations, described in chapter 4, showed that substrate defects would cause more severe image degradation than coating and absorber defects. Due to these considerations, substrate defects were the subject of the printability study described in chapter 6.

Simulations also revealed that the manners in which the defects are covered by multilayer reflective coatings can have very significant effects on defect printabilities. Coverage profiles that result in large lateral spreadings of defect geometries amplify the printability of the defects by increasing their effective sizes.

In order to obtain some information on the coverage profiles over defects on EUVL masks, a study of the profiles of sputtered-deposited Mo/Si multilayer coatings was conducted. Mo/Si coatings were deposited above programmed defects of different sizes. The coverage profiles were studied by observing the defects with an atomic force microscope (AFM) before and after the coatings were deposited. AFM measurements provided quantitative informations on the lateral spreading of substrate defects. Transmission electron microscopy (TEM) was also used to study the samples in cross-sections. TEM images showed clearly how the coverage profiles evolved during the coating deposition process. The results of this study are in chapter 5.

Hopefully the results obtained during the course of this thesis research will provide a basis for future discussions on mask specifications of EUVL.

References

1. *Semiconductor Technology Workshop, Working Group Reports*, 154 pages (Semiconductor Industry Association, San Jose, California, 1992).

2. G.E. Sommargren, and R. Hostetler, "Point diffraction interferometry at soft x-ray wavelengths," *Soft X-ray Projection Lithography* (Monterey, CA, USA), OSA *Proceedings*, vol. 18, A.M. Hawryluk, and R.H. Stulen ed., pages 100-104 (Optical Society of America, Washington, D. C., USA, 1993).

3. M.D. Levenson, "Wavefront engineering for photolithography," Physics Today, (July), pages 28-36 (1993).

4. T.A. Brunner, "Rim phase-shift mask combined with off-axis illumination: a path to 0.5λ/NA geometries," *Optical/Laser Microlithography VI* (San Jose, CA, USA), *SPIE Proceedings*, vol. 1927, D. Cuthbert ed., pages 54-62 (The International Society for Optical Engineering, Bellingham, Washington, USA, 1993).

5. H.I. Smith, and M.L. Schattenburg, "X-ray lithography, from 500 to 30 nm: X-ray nanolithography," IBM Journal of Research and Development, 37(3), pages 319-330 (1993).

6. J.A. Liddle, H.A. Huggins, S.D. Berger, J.M. Gibson, *et al.*, "Mask fabrication for projection electron-beam lithography incorporating the SCALPEL technique," Journal of Vacuum Science & Technology B (Microelectronics Processing and Phenomena), 9(6), pages 3000-4 (1991).

7. S.D. Berger, J.M. Gibson, R.M. Camarda, R.C. Farrow, *et al.*, "Projection electron-beam lithography: a new approach," Journal of Vacuum Science & Technology B (Microelectronics Processing and Phenomena), 9(6), pages 2996-9 (1991).

8. Y. Sakitani, H. Yoda, H. Todokoro, Y. Shibata, *et al.*, "Electron-beam cell-projection lithography system," Journal of Vacuum Science & Technology B (Microelectronics Processing and
Phenomena), 10, pages 2759-63 (1992).

9. U. Behringer, and H. Engelke, "Intelligent design splitting in the stencil mask technology used for electron- and ion-beam lithography," Journal of Vacuum Science & Technology B (Microelectronics Processing and Phenomena), 11(6), pages 2400-3 (1993).

10. H. Loschner, G. Stengl, A. Chalupka, J. Fegerl, *et al.*, "Projection ion beam lithography," Journal of Vacuum Science & Technology B (Microelectronics Processing and Phenomena), 11(6), pages 2409-15 (1993).

11. N.M. Ceglio, "Revolution in X-ray optics," Journal of X-ray science and technology, 1(1), pages 7-78 (1989).

12. D.M. Tennant, L.A. Fetter, L.R. Harriott, A.A. MacDowell, *et al.*, "Defect repair for soft x-ray projection lithography masks," Journal of Vacuum Science and Technology B, 10(6), pages 3134-3140 (1992).

Chapter 1

Extreme Ultraviolet Lithography — An Overview

Extreme ultraviolet lithography (EUVL) is a new approach to providing a high resolution lithographic capability for the fabrication of future microelectronic circuits. It is an extension of current optical/DUV projection techniques to shorter wavelengths and was made possible by recent advances in soft x-ray and EUV optics [1]. EUV lithography is a reduction imaging technique that uses reflective masks on thick substrates that are resistant to distortion. Reduction imaging with masks on thick substrates should make more manageable the requirements on wafer level overlay and pattern placement accuracy for the writing tool.

At EUV wavelengths, diffraction-limited imaging provides 0.1 μm resolution with 1 μm depth of focus. The wavelength and numerical aperture combinations satisfying this level of performance are shown figure 1.1 [2-5]. This figure was obtained from the relations for resolution and depth of focus of a diffraction-limited optical system,

$$R = k_1 \frac{\lambda}{NA}$$
$$DOF = k_2 \frac{\lambda}{NA^2} \qquad (1)$$

where λ is the operating wavelength, and NA is the numerical aperture of the imaging system. The factors k_1 and k_2 are constants whose values depend on system and processing parameters such as resist performance, illumination characteristics, and mask

geometry. In figure 1.1, k_1 was taken to be 0.7 and k_2 to be 1 — both values achievable in today's processes [6-8]. In order to achieve 0.1 μm resolution with 1 μm depth-of-focus under these conditions, the wavelength must be less than ~ 20 nm and the numerical aperture less than 0.14.

Since the reflective mask is the major topic of this thesis, discussions of mask issues are deferred to later chapters. An overview of the current state of EUVL technology is presented in this chapter, highlighting some of the recent works and outlining the necessary advances in order for EUVL to become a viable manufacturing technology.

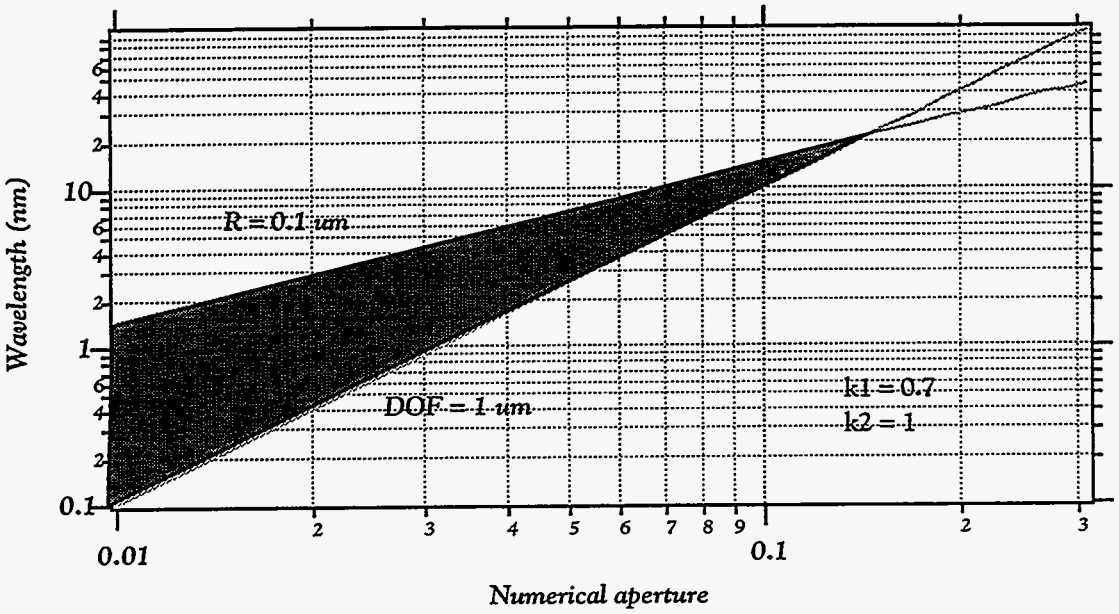

Figure 1.1. Combinations of numerical aperture and wavelength for 0.1 μm resolution and 1 μm depth-of-focus, with k_1 = 0.7 and k_2 = 1. The maximum wavelength is ~ 20 nm and the maximum NA is ~ 0.14.

1.1 EUVL System

1.1.1. Imaging System

Figure 1.2 is a diagram of an extreme utltraviolet lithographic system [2, 3, 9]. The system uses reflective optics coated with multilayer reflective coatings [10, 11]. It is a reduction imaging system utilizing step-and-scan exposure. In a step-and-scan system, the optics image a ring-field of millimeters width and centimeters length onto the wafer.

The entire mask pattern is exposed by scanning the mask and wafer relative. At the end of the scan, the wafer is moved to a new exposure field and the process repeated.

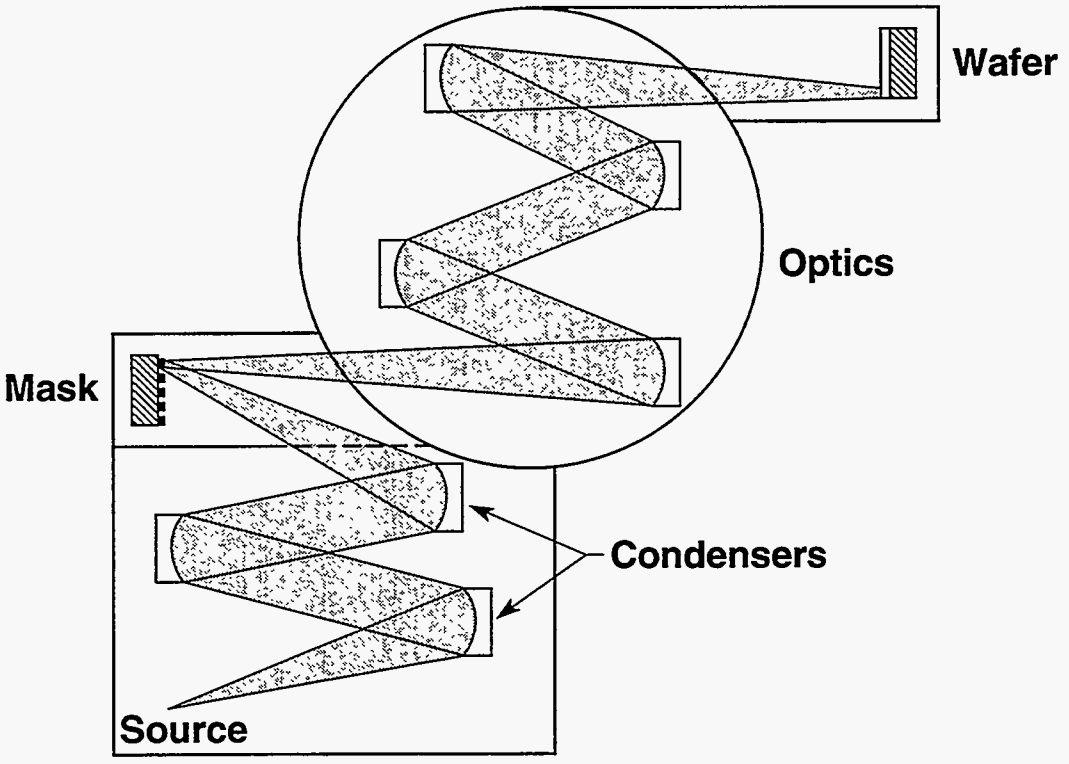

Figure 1.2. A diagram of an extreme ultraviolet lithography system (EUVL) showing its main components — source, condensers, reflective mask, imaging optics and wafer stage. The system is operated under vacuum (courtesy of N. Ceglio, LLNL).

The radiation source for an EUV system can either be a laser-produced plasma (LPP) or an electron storage ring (ESR) [12-14]. The condenser system is a critical component, necessary to provide enough power for adequate wafer throughput. Masks will be made up of absorber patterns deposited on multilayer reflective coatings above thick substrates that are thermally and mechanically stable. Imaging optics need to be precisely figured to provide diffraction-limited performance at EUV wavelengths. In addition, the number of optics needs to be minimized so that wafer throughput is maximized. In order to keep the number of optics to three or four in an optical system with 0.1 μm resolution over a ring-field of sufficient size, mirrors with slight asphericity would have to be used [15, 16]. The resist process is of course an integral part of any lithographic technique and will be the subject of section 1.1.4.

Reflective optics are needed because the index of refraction is close to unity and absorption is high in the EUV wavelength region. Refractive imaging at EUV

wavelengths is not possible because it would require very thick lenses with high absorption. The effect of EUV refractive indices on imaging is discussed in more detail in section 1.2.

Within the constraints of resolution and depth-of-focus, the choice of the operating wavelength is determined by many factors — the availability of high reflectivity coatings, resist performance and optical system performance. Hawryluk and Ceglio [4] have performed an analysis showing that the choice of wavelength is also influenced by considerations of thermal distortion of the optics and source power.

Reflective coating reflectivity is an extremely important parameter for high wafer throughput since the power deliverable to wafers scales as R^N where R is the reflectivity per surface and N is the number of reflections. In order to achieve 0.1 μm resolution over field sizes of 6-8 cm^2, at least 3–4 imaging optics are required even with the use of some aspherics in a ring-field step-and-scan system [15]. The required number of condenser optics is estimated to be at least three [9, 17], bringing the total number of reflections to seven or eight.

	Number of Mirrors		
Reflectivity	7	8	9
0.5	0.09	0.05	0.02
0.55	0.18	0.10	0.06
0.6	0.34	0.20	0.12
0.65†	0.60	0.39	0.25
0.7	1.00	0.70	0.49

Table 1.1. The effect of mirror reflectivity and the number of reflections on throughput, normalized to a system with 7 reflections from mirrors with 0.7 reflectivity, corresponding to a system with the estimated minimum number of reflections, and Mo/Si reflective coatings operating at their maximum theoretical reflectivities. Current maximum achievable peak reflectivity for a Mo/Si coating is 0.65.

Table 1.1 illustrates the impact of mirror reflectivity on throughput. The throughput values in the table are normalized to that of a 7-reflection system with 0.7 mirror reflectivity, corresponding to a system with the estimated minimum number of required reflections with Mo/Si reflective coatings operating at their maximum theoretical

reflectivities [16, 17]. Table 1.1 shows that a reduction of reflectivity from 0.65 to 0.6 results in a 50% reduction in throughput in a 7-mirror system. Currently, the maximum reported reflectivity for Mo/Si coatings at 13 nm is 0.65 [18]. High reflectivity mirrors are also necessary to reduce the thermal loading on the mirrors and prevent mirror distortions during exposure. This is an important consideration since the requirements for surface figure error will be very stringent for EUVL optics [19, 20].

The dependence of throughput and thermal loading on multilayer reflectivity provide strong motivations for choosing operating wavelengths with the highest reflectivity mirrors. Since the highest reflectivity is currently achieved with Mo/Si multilayer reflective coatings operating around 13 – 14 nm, most of the reported imaging experiments were performed at this wavelength [21-26].

The operating wavelength must also be chosen with considerations for resist performance. Resist materials are highly absorbing in the 13 nm wavelength region, resulting in significant sidewall slope in the developed images even for 60 nm thick resists [27-32]. The sloping sidewalls would make it difficult to maintain the ± 10% critical dimension (CD) control required in IC processing during the subsequent pattern transfers. Surface imaging resist, to be discussed in more detail in section 1.1.4, may provide a solution to this problem [33] .

In the meantime, works on reflective coatings at wavelengths shorter than 13 nm are being carried out by many researchers[10, 11]. Recent imaging experiments at 7 nm using a 2-mirror Schwarzschild system coated with Ru/B_4C multilayer coatings showed that deeper resist penetration can be achieved at shorter wavelengths [34, 35]. However, coating reflectivity per surface for Ru/B_4C at 7 nm, around 15%, is too low for acceptable throughput. More recently, 60% reflectivity has been reported for Mo/Be coatings at 11.5 nm, thus providing another possible choice of operating wavelength [36].

Since absorption in the soft x-ray and EUV region generally decreases with wavelengths [37-39], more layers are required for optimum reflectivity at shorter wavelengths. The larger number of bilayers results in a narrowed reflection bandwidth or cone of acceptance angle at a given wavelength. This effectively reduces the numerical aperture of the optical system, broadens the point spread function and reduces the achievable resolution. This effect has been reported by Berreman [40] and Watanabe [41]. The reduction in resolution, while small at 13 nm wavelength, increases for shorter

wavelengths and is quite severe for imaging at 4.5 nm.

The choice for a step-and-scan system is driven by throughput and optical fabrication considerations. The number of reflections in the optical system must be minimized since every additional reflection results in a 30–40% reduction in throughput. The mirrors in the system should have only small aspheric departures to ease their fabrications. An optical design study by Jewell et al. [16], for example, shows that these conditions may be satisfied in a ring-field scanning design with four mirrors.

The precise tracking of reticle and wafer stage in a reduction step-and-scan system is a very challenging task [42]. In a stepper, the wafer stage needs to move only to a precise position, and the important performance number is the step-and-settle time. In a step-and-scan system, both the mask and wafer must move in exact synchronism and their velocities must be constant during the active part of the scan. The SVGL Micrascan® is an example of such a system [42].

With a step-and-scan system, a large field size can be achieved with relatively few imaging elements. In addition, the system performs an integration in the scan direction, thus easing the requirements on illumination uniformity. Focus may also be adjustable during the scan [42].

1.1.2. Optical Tolerance Requirements and Metrology of EUVL Optics

Since the required optical tolerances for an optical system scales with wavelength, the requirements on surface figure control for EUVL are very severe. For near-diffraction-limited systems, the optical tolerances can be set by considering the ratio between the maximum intensity of the aberrated point-spread-function compared to the unaberrated one. This ratio $i(P)$ can be expressed as [43],

$$i(P) \sim 1 - \frac{4\pi^2}{\lambda^2}\left[\frac{\iint_A \{W(x,y)\}^2 dxdy}{A} - \left\{\frac{\iint_A W(x,y)dxdy}{A}\right\}^2\right] \qquad (2)$$

where $W(x, y)$ is the wavefront aberration as a function of coordinates on the pupil.

Both integrations are performed over the pupil area A.

A Strehl ratio of 0.8 is often considered to be an acceptable performance level for a diffraction limited system [44]. This ratio is reached for wavefront aberration variance of $\lambda^2/197$, thus requiring the root-mean-square departure of the wavefront from the reference sphere centered on the diffraction focus to be less than $\lambda/14$ [43]. This is also called the Marechal condition and corresponds to a maximum peak-to-peak wavefront variation of $\lambda/5$. If the only aberration is defocus, then the Strehl tolerance limit requires a maximum of $\lambda/4$ peak-to-peak wavefront aberration. This was the case considered by Lord Rayleigh to arrive at his quarter-wavelength rule [44].

Assuming that errors on different mirrors are independent, hence adding in quadrature, and each mirror contributes equally to the total wavefront error σ_T, the allowed wavefront error from each mirror σ can be written as,

$$\sigma_T^2 \cong N\sigma^2,$$
$$\sigma \cong \frac{\sigma_T}{\sqrt{N}} \qquad (3)$$

where N is the number reflections. At 13 nm, the Marechal condition requires that the total rms wavefront error be less than 1 nm. For $N = 4$, each reflection can contribute no more than 0.5 nm rms error to the wavefront. Hence surface figure error on the mirror must be less than 0.25 nm rms.

This level of accuracy is beyond the capability of visible light interferometry which has an accuracy of about $\lambda_{visible}/100$ under ideal conditions. For $\lambda_{visible}$ of 633 nm, this is a factor of 25 from what is required [45], thus necessitating the development of "at-wavelength" interferometry to provide the required measurement accuracy. A common-path x-ray point diffraction interferometer is currently being constructed at Lawrence Berkeley Laboratory for this purpose [19, 45].

1.1.3. EUV Sources

Source power requirements for EUVL depend on a number of parameters. For a fixed required wafer throughput, the required source power depends on,

(1) collection efficiency of the condenser system
(2) reflectivity of multilayer mirrors
(3) number of mirrors in the imaging system
(4) resist sensitivity
(5) stepper overhead time

It also depends on other parameters, including the number of vacuum windows in the system, whether or not a pellicle would be needed on the mask (see chapter 2), and how well the reflection peaks of the different mirrors can be aligned to each other [34, 46].

Estimates by Early [47] indicate that between approximately 500 mW would be needed at the mask plane for satisfactory wafer throughput. The leading candidates for providing the desired power are electron storage rings (ESR) and laser plasma sources (LPS) [12-14, 48-57].

Electron storage rings involve well-understood processes, provide high photon flux into a broadband of wavelengths and can simultaneously drive many wafer printers. Many synchrotrons have been built for proximity x-ray lithography around the world. Arguments against them, however, are their large footprints and buy-in costs.

Laser plasma sources are smaller and could fit more easily into existing facilities. They are also modular sources. Modularity means that each printer has its own source, and when the source needs to be refurbished, only one printer must be taken off production so that wafer throughput is reduced by only a fraction of the total output. If an electron storage ring with many printers connected to it needs to be refurbished, wafer printing would be temporarily halted for the entire fab. The modularity and small footprints for laser-plasma sources may make it easier for companies to invest in EUVL on a trial basis, to obtain a few steppers to evaluate their performances, thus easing the introduction of EUVL.

Issues to be addressed for LPS are the availability and reliability of high-power laser drivers, and target debris. Recent experimental results have demonstrated conversion efficiencies from laser power to EUV power in a 2.3% BW at 13 nm of 2% [55]. For a condenser system with 0.2 sr collection solid angle [17, 58], a laser power of 800 W is required to provide 500 mW at the mask . Works on providing such lasers are being carried out at Lawrence Livermore National Laboratory [48] and TRW. An additional difficulty with laser plasma sources is the control of target debris generated by laser illumination. Target debris can contaminate and damage the condenser optics, thus reducing the time-between-repair and increasing the cost-of-ownership for EUV lithography. It is a problem that is receiving much attention from researchers in the field [51, 54].

Power outputs from three electron storage rings currently in operation are presented here for comparison with laser-plasma sources — Helios built by Oxford Instruments, Inc. for IBM Advanced Lithography Facility at East Fishkill, Aurora built by Sumitomo Heavy Industries in Japan, and CAMD at Louisiana State. Helios and Aurora use superconducting magnets, while CAMD uses conventional magnets. With the parameters provided in Table 1.2, the power outputs from bending magnets in these storage rings can be calculated using well-verified formulas [59].

Though the full expression for bending magnet power output is somewhat complicated (see Appendix A), the photon flux from a bending magnet can be expressed as,

$$F_B(photons\ /\sec) = 2.457x10^{16} E(GeV) I(A) \theta(mrad) G_1(\omega/\omega_c) \frac{\Delta\omega}{\omega}, \qquad (4)$$

$G_1(y)$ is given in terms of modified Bessel function of the second kind $K_{5/3}$,

$$G_1(y) = y\int_y^\infty K_{5/3}(y')dy' \qquad (5)$$

where,

y = $h\omega/h\omega_c$

θ = horizontal collection angle

$\frac{\Delta\omega}{\omega}$ = collection bandwidth

ε_c = $\frac{h\omega_c}{2\pi}$

= critical energy of the storage ring, the energy that

divides the emitted power spectrum into two equal halves

= $0.665E^2(GeV)B(T)$ in units of keV.

E = energy of the storage ring (GeV)

B = magnetic field of the bending magnet (Tesla)

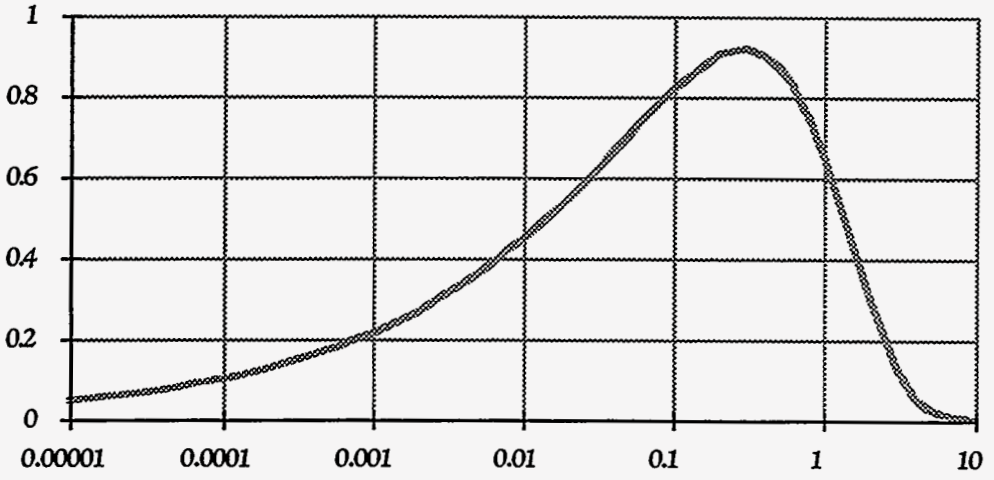

$$y = \omega/\omega_c = \varepsilon/\varepsilon_c$$

Figure 1.3. The function $G_1(y)$, where y is the ratio of the photon energy to the critical photon energy.

The power outputs from these storage rings were calculated for bandwidths of 3% and horizontal collection angle of 50 milliradians. The results tabulated in Table 1.2 show the power outputs at wavelengths suitable for EUVL, at 4.5 nm, 7 nm, and 13 nm. Since Helios, Aurora and CAMD were built with proximity printing in mind, power outputs were optimized for 1 nm wavelength. Even so, they are still capable of providing 60 mW to 200 mW in a 3% BW with 50 mrad collection angle at 13 nm wavelength. In order to collect 500 mW, a collection angle of 125-400 mrad is needed. Various condenser designs have been proposed to achieve this [12, 57].

Table 1.2. Power output from bending magnets for Helios, Aurora and CAMD.

	Helios (Oxford Ins.)	Aurora (Sumitomo)	CAMD (Maxwell-Brobeck)
Energy (GeV)	0.7	0.65	1.2
Current (mA)	200	300	400
Magnetic Field (T)	4.5	4.3	1.37
Power output (mW/50 mrad-3% BW)			
4.5 nm	210	300	725
7 nm	140	200	500
13 nm	62.5	82.5	210

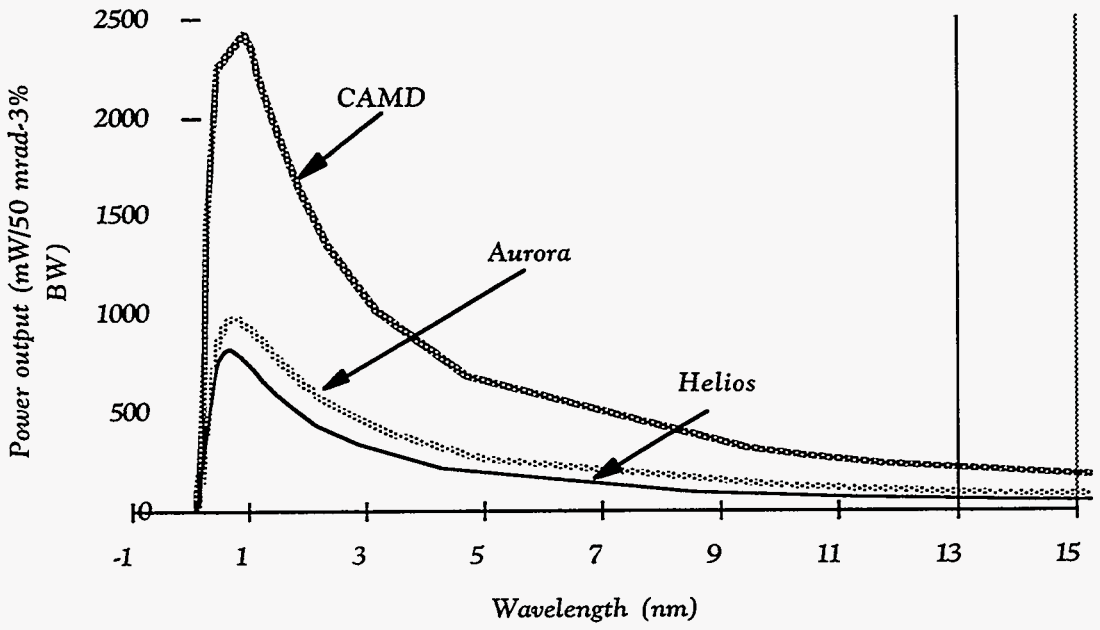

Figure 1.4. Power outputs from bending magnets in two electron storage rings built for proximity x-ray lithography. Power output was calculated for a 50 mrad horizontal collection angle.

1.1.4. Resist

The requirements for EUVL resists, as they are for any resists, are high sensitivity and contrast, high resolution, good linewidth control, low defect density and good etch resistance [60]. For EUVL, the resist's resolution must be at least 0.12 μm since that is the intended insertion point for the technology. The requirement on resolution places a proportional requirement on edge roughness and linewidth control. In order that the linewidth varies by no more than 10% with 3σ statistical confidence (i.e. 99.74% confidence), linewidth variance must be no more than 4 nm.

The depth-of-focus for EUVL is estimated to be ± 0.5 μm at 0.12 μm resolution for 13 nm illumination. Spin-coating of resist produces thickness variations over topography ranging from 0.3–0.7 μm. Other contributions to focus errors include substrate bowing, substrate thickness non-uniformity and wafer position placement error. These considerations suggest that a planarizing layer is likely to be necessary for EUVL [33].

Since significant losses will occur due to reflections from as many as seven surfaces with 60%–70% reflectivities, a resist with high sensitivity is required for high wafer throughput. Estimates for the required sensitivity range from 2 to 10 mJ/cm^2 [2, 9, 47] .

The high absorption at EUV wavelengths is an important limiting factor for EUVL resists, resulting in sloping resist sidewalls and poor critical dimension (CD) control in subsequent pattern transfers [28]. The 1/e absorption depths (63.2% absorption) for ten polymers that are representatives of common resist materials were calculated by Taylor et al. [33]. Their results showed that the 1/e depths at 13 nm for these materials are between 0.1–0.25 μm. If the topographies of future semiconductor devices are assumed to be 200 nm high [33], resists must be at least ~ 0.5 μm thick for sufficient step coverage (smoothing over step), low defect density (pinholes) and etch resistance. Thus a conventional single layer resist process is not likely to be usable for EUVL.

Current high resolution imaging experiments sidestep this problem by using very thin imaging layers of ~ 70 nm in both single layer and tri-layer processes [21, 22]. Such thin layers, however, have marginal etch resistance and suffer from large pinhole densities [32]. In addition, trilevel resists are not favored by industry for fear that the complexity of the process would reduce yield and increase cost [61].

In order to overcome the problems resulting from high absorption, surface imaging by silylation has been attempted by researchers at AT&T. The results show moderate sensitivity of ~ 35 mJ/cm^2 and reasonable resolution/CD control [62]. Surface imaging is well-suited for EUVL since it takes advantage of high resist absorption to confine the exposed region to a thin layer at the surface of the resist. A diagram of possible surface imaging schemes for EUVL is shown in figure 1.5. Since there is no planarizing film with good imaging properties at the present time, it seems likely that a bilayer resist structure would be required [33]. Imaging experiments with a self-assembled monolayer film have also been reported with resolutions of 0.25 μm at 50 mJ/cm^2 [63]. In addition to alleviating the absorption problem, surface imaging is insensitive to substrate reflection and may yield high resolution due to the steep resist sidewalls that result from the use of anisotropic plasma etching.

Chemically amplified resists have been found to have excellent sensitivities in the range of 2 mJ/cm^2 to 10 mJ/cm^2. However, they suffer from marginal resolution and high absorption [27, 31, 32, 64]. The chemical amplification process results from photogenerated acids that catalyze many subsequent chemical events, effectively increasing the quantum efficiency of the resist. As a result, resist linewidths vary with concentration of the acidic species, thus requiring tight controls of post-exposure processes and environmental conditions [61, 65].

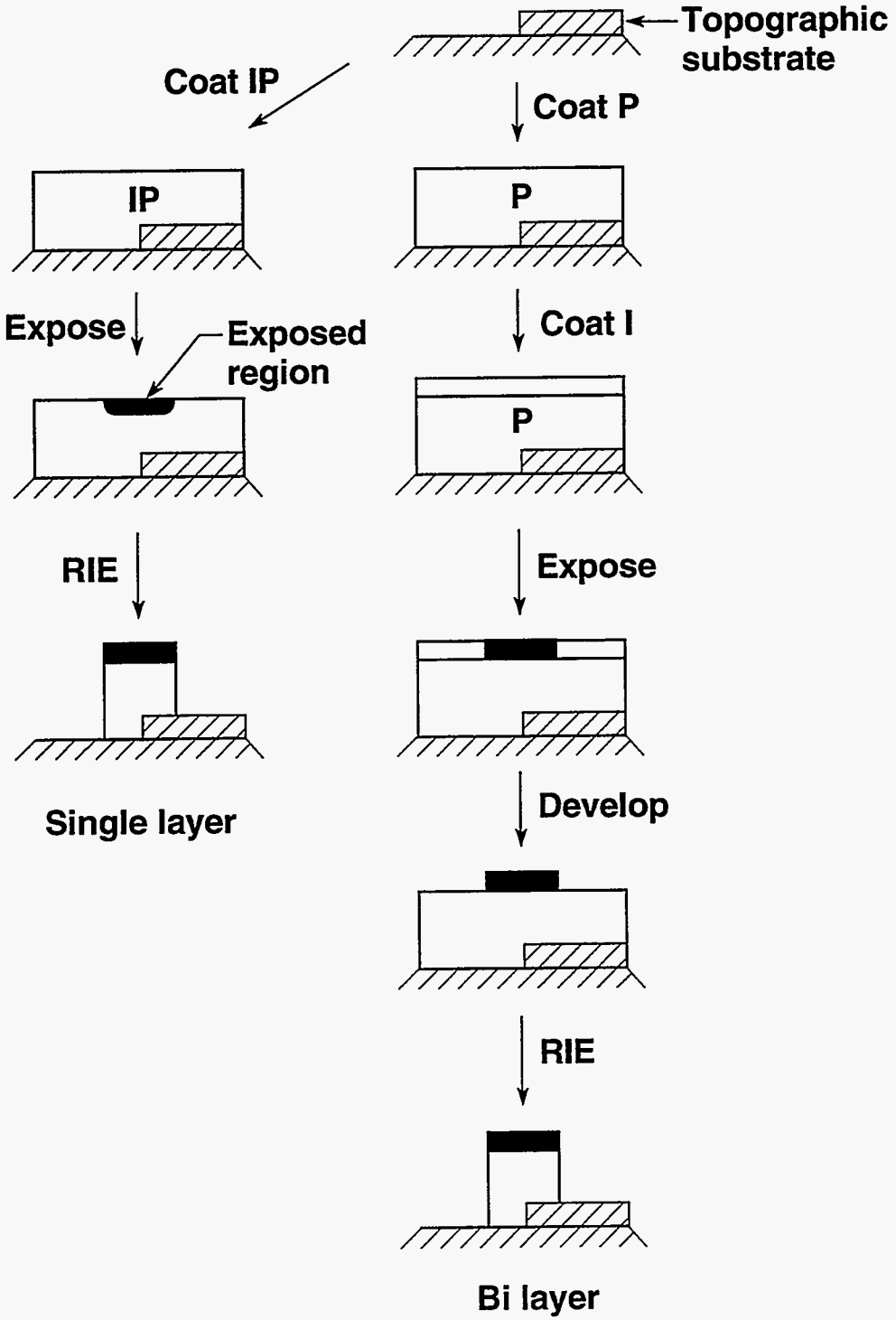

Figure. 1.5. Schematic of the single layer and bilayer surface imaging resist process. In a single layer, the planarizing layer (IP) is also the imaging layer. In a bilayer process, an imaging layer (I) is added above the planarizing layer (P) (Courtesy of G. Taylor, AT&T [33]).

1.2 Multilayer Coatings

The capability to deposit multilayer coatings with high normal incidence reflectivity is one of the most important enabling technology for extreme ultraviolet lithography [66-70]. Multilayer coatings with high normal incidence reflectivity have made possible diffraction-limited EUV imaging with spherical and near-spherical optics, thus opening the possibility of large-field reduction EUV lithography for integrated circuits. This section presents a brief description of multilayer reflective coatings — their effects on soft x-ray/EUV imaging, operating principles and fabrication techniques.

Before the advent of multilayer reflective coatings, reflective soft x-ray/EUV imaging was performed only at glancing incidence since reflectivity at near-normal incidence for single layer coatings is very low. This low reflectivity is a consequence of near-unity refractive indices in the EUV wavelength region for all materials, which in turns results from the fact that the energies of x-ray and EUV radiation are above the resonances of bound electrons in all elements.

The refractive index, n, in the soft x-ray/EUV region is commonly written as,

$$\begin{aligned} n &= 1 - \delta(\lambda) - i\beta(\lambda) \\ &= 1 - \frac{N_a r_e \lambda^2}{2\pi}(f_1 + if_2) \end{aligned} \tag{6}$$

where N_a is the number of atoms per unit volume, r_e is the classical electron radius, and $(f_1 + if_2)$ is the atomic scattering factor which gives the scattering amplitude of an atom relative to that of a free electron. Henke, Gullikson and colleagues have compiled tables of atomic scattering factor in the soft x-ray/ EUV wavelength region [39]. The values are derived from best fits to available absorption data (f_2) measured over a broad energy range for elements from hydrogen to plutonium. The real part (f_1) is then determined using Kramers-Kronig techniques.

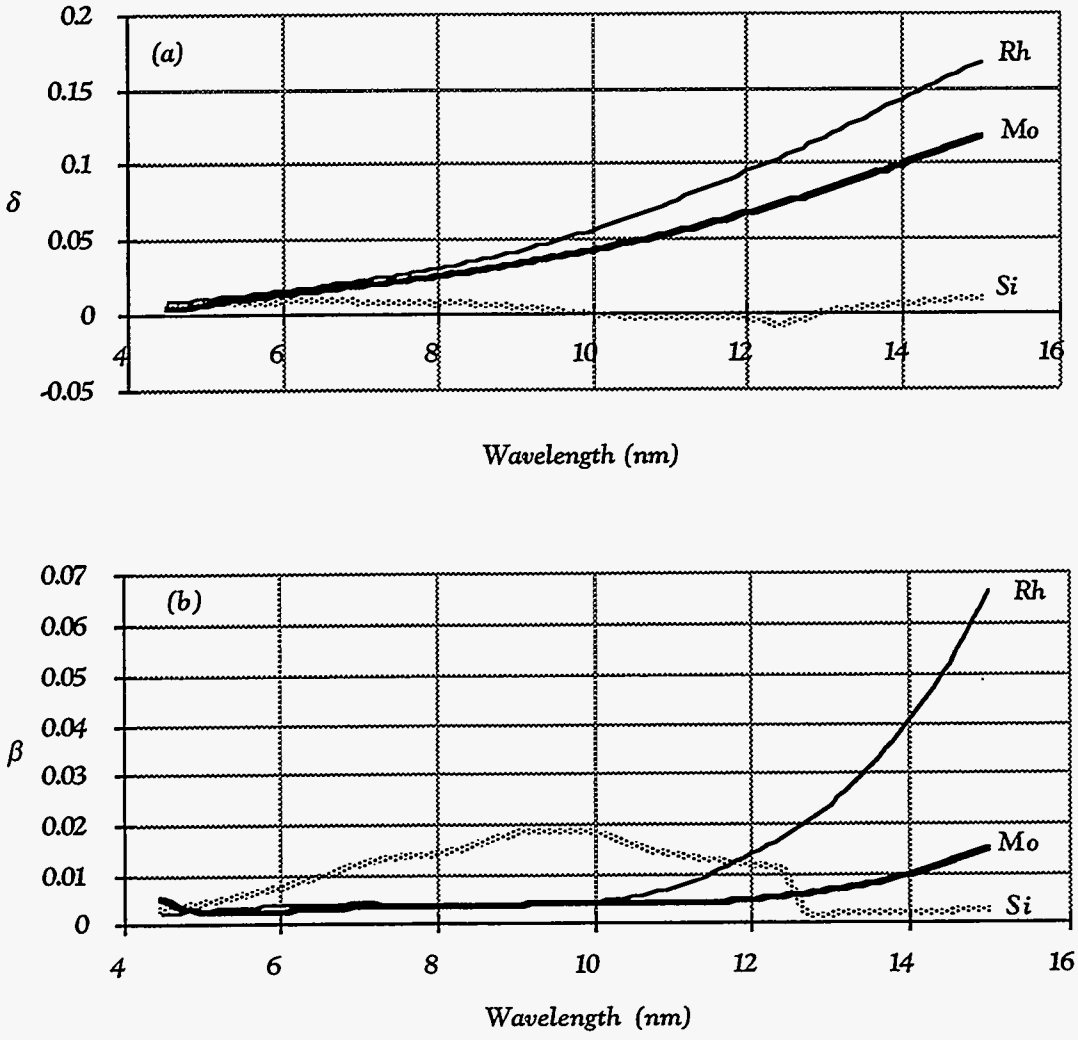

Figure 1.6. Index of refraction for Si, Mo, Rh between 4.5 nm and 15 nm, (a) the real part δ, (b) the imaginary part β.

Figure 1.6 shows the values of δ and β for Mo, Si and Rh for wavelengths between 4.5 nm and 15 nm, i.e. between the carbon-K edge and the silicon-L edge. Mo and Si are the materials of choice for high normal incidence reflectivity at 13–14 nm. Rh is a common coating for glancing incidence mirrors in EUV. At normal incidence, reflectivity in vacuum for a single coating is given as,

$$\frac{I}{I_o} = |r|^2 = \left|\frac{1-n}{1+n}\right|^2 \cong \frac{(\delta^2+\beta^2)}{4} \tag{7}$$

With the values of δ and β in figure 1.6, single coating reflectivities range from 10^{-2} to 10^{-4} between 4.5 nm and 15 nm, thus motivating the need for multilayer reflective coatings.

At glancing incidence, high reflectivity can be obtained with single-coating since the waves are evanescent in the reflective medium. However, high resolution imaging at glancing incidence requires optics that are sections of conics. Even though designs exist for high resolution glancing-incidence imaging systems such as the Wolter-type optics [71], conics surfaces are very difficult to fabricate, resulting in large surface figure errors that limit the resolution of the system.

The use of multilayer coatings to increase normal-incidence reflectivity allows near-normal incidence imaging with high throughput. This makes possible diffraction-limited imaging at EUV wavelengths with spherical and near-spherical optics and makes the optical fabrication process manageable. However, optical fabrication and testing remain one of the most daunting challenges for EUVL.

1.2.1. Multilayer Principles

Multilayer coatings consist of repeating alternating layers of two materials with different refractive indices. The combination typically consists of a high Z, high refractive index, high absorption material and a low Z, lower refractive index and lower absorption spacer material. It can be thought of as either a two-dimensional crystal with large lattice spacing or an interference coating with very small spacing.

The enhancement in reflectivity results from constructive interference of weak reflections from the many interfaces of the multilayer coating. Neglecting refraction, the condition for constructive interference is given by the Bragg equation,

$$m\lambda = 2(d_A + d_B)\sin\theta, \tag{10}$$

where d_A and d_B are thickness of each layer of material A and B and θ is the angle of incidence as measured from the glancing incidence (normal incidence is 90°). Correction for refraction results in the expression [72],

$$m\lambda = 2(d_A + d_B)\sin\theta_m\left(1 - \frac{\delta}{\sin^2\theta_m}\right), \qquad (11)$$

where θ_m is the angle of the m^{th} reflection peak. Note that for normal incidence (θ = 90°), the d-spacing is $\lambda/2$, and d_A and d_B are approximately $\lambda/4$. In practice, the high-Z layer is made somewhat thinner than the low-Z layer to reduce absorption loss. Γ, the ratio of the high-Z layer thickness to stack thickness $d_A/(d_A+d_B)$, is typically 0.4 for Mo/Si coatings.

The fabrication of x-ray multilayer reflective coatings has been attempted since the 1920s [73]. Recent improvements in the quality of these coatings were made possible by the advances in vacuum deposition techniques pioneered by Eberhard Spiller [66, 67] at IBM Watson Research Center and Troy Barbee at Stanford University [74]. In order to maximize the reflectivity, material combinations are chosen for large differences in their indices of refraction, low absorption, low inter–diffusion between layers, low interlayer roughness, and low film stress.

Figure 1.8 shows the calculated reflectivity of a Mo/Si reflective coating with 40 bilayers and 7-nm period. The interfaces between the materials were assumed to be perfectly sharp. The highest reflectivity that has been reported experimentally for Mo/Si is ~ 65% [75]. Differences between the measured and predicted reflectivity is largely due to interfacial roughness and interfacial mixing of the layered materials.

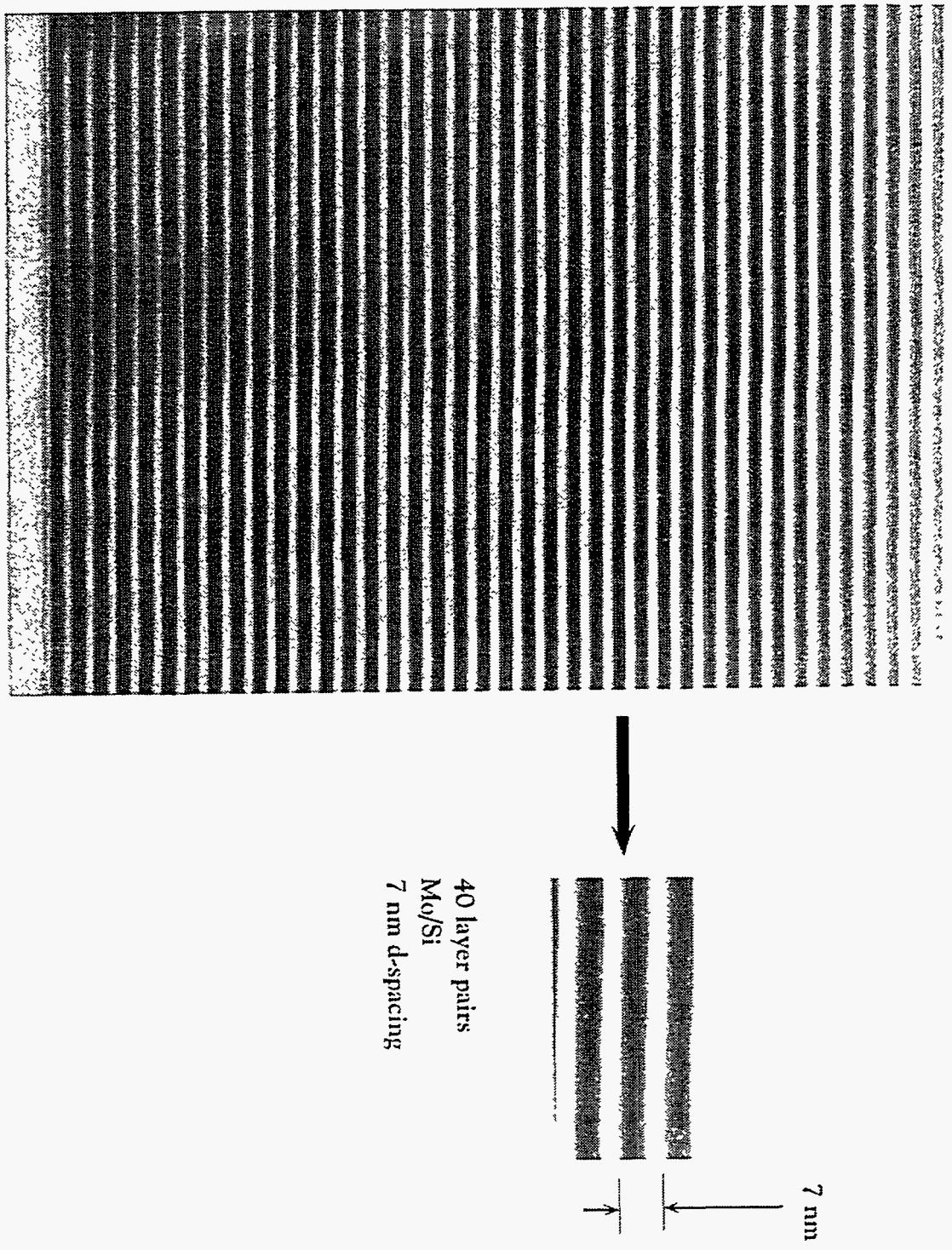

Figure 1.7. A multilayer reflective coating as imaged by transmission electron microscopy. The coating consists of 40 bilayers of Mo/Si with bilayer spacing of 7 nm. d_{Mo}/d_{Si} is ~ 2/3 (TEM taken by Tai D. Nguyen, LBL).

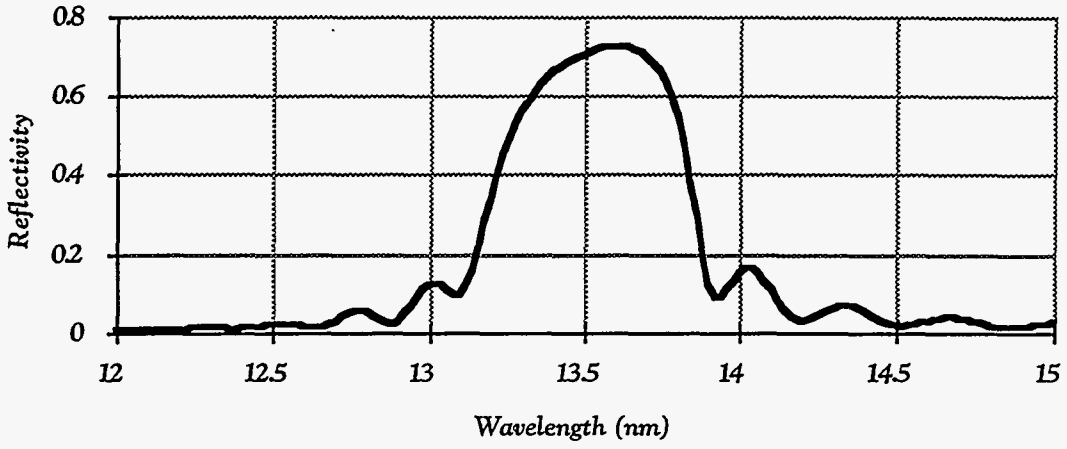

Figure 1.8. Reflectivity from an ideal multilayer coating as calculated with Fresnel theory of reflection and Henke optical constants. The coating consists of 40 bilayers of Mo/Si with 7 nm d-spacing. d_{Mo}/d_{Si} is 2/3. The top layer is Mo.

1.2.2. Multilayer Deposition Process

For my thesis research, multilayer coating deposition was performed using a planar magnetron sputtering [76] system at the Center for X-ray Optics, Lawrence Berkeley Laboratory. In this system, the substrates to be coated rotate on a table above the magnetron sputtering sources. The deposition rates are controlled by varying the rotation speed of the substrate table and the power to the sputtering targets. Powers to the sources are accurately controlled with stable precision power supplies. Either rf or dc sputtering is used, depending on the materials. The alternating layer structure is built up as the table rotates, moving the substrates sequentially over the targets. The system is operated at a base pressure of ~ $1x10^{-6}$ torr. Sputtering is performed in argon at 2.5×10^{-3} torr.

The d-spacings of the coatings are determined by measuring x-ray diffraction with a Cu Kα source and fitting the reflection peaks to Bragg's equations [72]. The positions of the reflection peaks represent the statistical average for the d-spacing throughout the stack and the widths of the peaks yield information on the spacing variance.

1.3 Conclusion

Extreme ultraviolet lithography is a promising technique capable of providing 0.1 μm resolution with 1 μm depth-of-focus. It is a reduction imaging technique based on a thick stable reflective mask that promises to make the wafer level overlay requirements more manageable. Due to its short operating wavelengths, EUVL may be extendible over a number of future generations of semiconductor devices.

Before it can become a viable commercial technology, however, significant advances are required in many key areas. Perhaps the most critical challenge for EUVL is the fabrication of optics to the required tolerances for diffraction-limited imaging and holding to this tight figure requirement during exposure. Resist is another key area requiring advances. Much work also remains to be done in the area of mask fabrication and defect inspection/repair. This will be the topic of the remainder of my thesis.

References

1. N.M. Ceglio, "Revolution in X-ray optics," Journal of X-ray science and technology, 1(1), pages 7-78 (1989).

2. D.L. White, J.E. Bjorkholm, J. Bokor, L. Eichner, R.R. Freeman, T.E. Jewell, W.M. Mansfield, A.A. MacDowell, L.H. Szeto, D.W. Taylor, D.M. Tennant, W.K. Waskiewicz, D.L. Windt, and O.R. Wood II, "Soft x-ray projection lithography," Solid State Technology, (July), pages 37-42 (1991).

3. R.H. Stulen, and R.R. Freeman, "Developing a soft x-ray projection lithography tool," AT&T Technical Journal, (Nov/Dec), pages 37-48 (1991).

4. A.M. Hawryluk, and N.M. Ceglio, "Wavelength considerations in soft x-ray projection lithography," Applied Optics, 32(34), pages 7062-7067 (1993).

5. H. Kinoshita, K. Kurihara, Y. Ishii, and Y. Torii, "Soft x-ray reduction lithography using multilayer mirrors," Journal of Vacuum Science and Technology B, 7(6), pages 1648-1651 (1989).

6. R.F. Pease, "Limits of Ultraviolet Lithography," *Soft X-ray Projection Lithography* (Monterey, CA, USA), *OSA Proceedings*, vol. 18, A.M. Hawryluk, and R.H. Stulen ed., pages 6-9 (Optical Society of America, Washington, D. C., 1993).

7. H. Sewell, and A.R. Reinberg, "Resolution in microlithography," Microelectronic Engineering, **11**, pages 153-159 (1990).

8. S. Okazaki, "Resolution limits of optical lithography," Journal of Vacuum Science and Technology B, **9**, pages 2829-2834 (1991).

9. N.M. Ceglio, and A.M. Hawryluk, "Soft x-ray projection lithography system design," *Soft x-ray projection lithography* (Monterey, CA, USA), *OSA Proceedings*, vol. 12, J. Bokor ed., pages 5-10 (Optical Society of America, Washington, D. C., USA, 1991).

10. J.B. Kortright, D.G. Stearns, and D.L. Windt, ed., *Physics of X-ray Multilayer Structures (Jackson Hole, Wyoming, USA, March 2-5, 1992)*, OSA Technical Digest Series, vol. 7, 186 pages (Optical Society of America, Washington, D. C., 1992).

11. J. Kortright, D. Stearns, and E. Ziegler, ed., *Physics of X-ray Multilayer Structures (Jackson Hole, Wyoming, USA, March 14-17, 1994)*, OSA Technical Digest Series, vol. 6, 188 pages (Optical Society of America, Washington, D. C., 1994).

12. J.B. Murphy, D.L. White, A.L. MacDowell, and O.R. Wood II, "Synchrotron radiation sources and condensers for projection x-ray lithography," Applied Optics, **32**(34), pages 6920-6929 (1993).

13. K.B. Nguyen, and D.T. Attwood, "Source issues relevant to x-ray lithography," *Soft X-ray Projection Lithography, Topical Meeting* (Monterey, CA, USA), *OSA Proceedings*, vol. 12, J. Bokor ed., pages 62-67 (Optical Society of America, Washington, D. C., 1991).

14. W.T. Silfvast, M.C. Richardson, H. Bender, A. Hanzo, V. Yanovsky, F. Jin, and J. Thorpe, "Laser-produced plasmas for soft x-ray projection lithography," Journal of Vacuum Science and Technology B, **10**(6), pages 3126-3133 (1992).

15. T.E. Jewell, "Reflective system design study for soft x-ray projection lithography," Journal of Vacuum Science and Technology B, 8(6), pages 1519-1523 (1990).

16. T.E. Jewell, K.P. Thompson, and J.M. Rodgers, "Reflective optical designs for soft x-ray projection lithography," *Current Developments in Optical Design and Optical Engineering* (San Diego, CA, USA), *SPIE Proceedings*, vol. 1527, pages 163-173 (SPIE, Bellingham, Washington, USA, 1991).

17. G.E. Sommargren, and L.G. Seppala, "Condenser optics, partial coherence, and imaging for soft x-ray projection lithography," Applied Optics, 32(34), pages 6938-6944 (1993).

18. D.G. Stearns, R.S. Rosen, and S.P. Vernon, "Multilayer mirror technology for soft x-ray ojection lithography," Applied Optics, 32(34), pages 6952-6960 (1993).

19. D. Attwood, G. Sommargren, R. Beguiristain, K. Nguyen, J. Bokor, N. Ceglio, K. Jackson, M. Koike, and J. Underwood, "Undulator radiation for at-wavelength interferometry of optics for extreme ultraviolet lithography," Applied Optics, 32(34), pages 7022-7031 (1993).

20. H.I. Smith, and M.L. Schattenburg, "X-ray lithography, from 500 to 30 nm: X-ray nanolithography," IBM Journal of Research and Development, 37(3), pages 319-330 (1993).

21. J.E. Bjorkholm, J. Bokor, R.R. Freeman, J. Gregus, T. Jewell, W.M. Mansfield, A.A. MacDowell, E.L. Rabb, W.T. Silvast, L.H. Szeto, D.M. Tennant, W.K. Waskiewicsz, D.L. White, D.L. Windt, O.R. Wood II, and J.H. Bruning, "Reduction imaging at 14 nm using multilayer-coated optics: printing of features smaller than 0.1 μm," Journal of Vacuum Science and Technology B, 8(6), pages 1509-1513 (1990).

22. D.W. Berreman, J.E. Bjorkholm, L. Eichner, R.R. Freeman, T.E. Jewell, W.M. Mansfield, A.A. MacDowell, M.L. O'Malley, E.L. Raab, W.T. Silvast, L.H. Szeto, D.M. Tennant, W.K. Waskiewicz, D.L. White, D.L. Windt, and O.R. Wood II, "Using tri-level resists for high-resolution soft x-ray projection lithography," Applied Physics Letters, 56(22), pages 2180-2182 (1990).

23. H. Kinoshita, K. Kurihara, T. Mizota, T. Haga, Y. Torii, H. Takenaka, and Y. Ishii, "Soft x-ray reduction lithography using a reflection mask," *Soft x-ray projection lithography* (Monterey, CA), *OSA Proceedings*, vol. 12, J. Bokor ed., pages 11-15 (Optical Society of America, Washinton, D. C., 1991).

24. H. Kinoshita, K. Kurihara, T. Mizota, T. Haga, H. Takenaka, and Y. Torii, "Large-area, high-resolution pattern replication, by the use of a two-aspherical-mirror system," Applied Optics, **32**(34), pages 7079-7083 (1993).

25. D.A. Tichenor, G.D. Kubiak, M.E. Malinowski, R.H. Stulen, S.J. Haney, K.W. Berger, L.A. Brown, W.C. Sweatt, J.E. Bjorkholm, R.R. Freeman, M.D. Himel, A.A. MacDowell, D.M. Tennant, O.R. Wood II, T.E. Jewell, W.M. Mansfield, W.K. Waskiewicz, D.L. White, and D.L. Windt, "Soft x-ray projection lithography experiments using Schwarzchild imaging optics," Applied Optics, **32**(34), pages 7068-7071 (1993).

26. D.A. Tichenor, G.D. Kubiak, M.E. Malinowski, R.H. Stulen, S.J. Haney, K.W. Berger, L.A. Brown, R.R. Freeman, W.M. Mansfield, O.R. Wood II, D.M. Tennant, J.E. Bjorkholm, T.E. Jewell, D.L. White, D.L. Windt, and W.K. Waskiewicz, "Soft x-ray projection imaging using a laser-plasma source," *Soft x-ray projection lithography* (Monterey, CA), *OSA Proceedings*, vol. 12, J. Bokor ed., pages 54-57 (Optical Society of America, Washington, D. C., 1991).

27. G.D. Kubiak, E.M. Kneedler, R.Q. Hwang, M.T. Schulberg, and K.W. Berger, "Characterization of chemically amplified resists for soft x-ray projection lithography," Journal of Vacuum Science and Technology B, **10**(6), pages 2593-2599 (1992).

28. W.M. Mansfield, O.R. Wood II, R. D'Souza, and A.R. Neureuther, "Effects of absorption on resist performance in soft x-ray projection lithography," *Soft X-ray Projection Lithography* (Monterey, CA, USA), *OSA Proceedings*, vol. 12, J. Bokor ed., pages 129-131 (Optical Society of America, Washington, D. C., 1991).

29. G.D. Kubiak, E.M. Kneedler, K.W. Berger, R.H. Stulen, J.E. Bjorkholm, W.M. Mansfield, and H. Windischmann, "Resist characterization at soft x-ray wavelengths," *Soft X-ray Projection Lithography* (Monterey, CA, USA), *OSA Proceedings*, vol. 12, J. Bokor ed., pages 124-128 (Optical Society of America, Washington, D. C., 1991).

30. G.D. Kubiak, R.Q. Hwang, M.T. Schulberg, D.A. Tichenor, and K. Early, "Chemically amplified soft x-ray resists: sensitivity, resolution, and molecular desorption," Applied Optics, 32(34), pages 7036-7043 (1993).

31. K. Early, D.M. Tennant, D.Y. Jeon, P.P. Mulgrew, A.A. MacDowell, and O.R. Wood II, "Characterization of AZ PN114 resist for high resolution using electron-beam and soft x-ray projection lithography," Journal of Vacuum Science and Technology B, 10(6), pages 2600-2605 (1992).

32. K. Early, D.M. Tennant, D.Y. Jeon, P.P. Mulgrew, A.A. MacDowell, O.R. Wood II, G.D. Kubiak, and D.A. Tichenor, "Characterization of AZ PN114 resist for soft x-ray projection lithography," Applied Optics, 32(34), pages 7044-7049 (1993).

33. G.N. Taylor, R.S. Hutton, D.L. Windt, and W.M. Mansfield, "Resist schemes for soft x-ray lithography," *X-ray/EUV Optics for Astronomy, Microscopy, Polarimetry and Projection Lithography , SPIE Proceedings*, vol. 1343, R.B. Hoover, and A.B. Walker ed., pages 258-273 (The International Society of Optical Engineering (SPIE), Bellingham, WA, USA, 1990).

34. J.B. Kortright, E.M. Gullikson, and P.E. Denham, "Masked deposition techniques for achieving multilayer period variations required for short-wavelength (68 Å) soft x-ray imaging optics," Applied Optics, 32(34), pages 6961-6968 (1993).

35. O.R. Wood II, and A.A. MacDowell, personal communications (1993).

36. D. Makowiecki, C. Alford, K. Skulina, J. Kortright, R. Soufli, E. Gullikson, and J. Underwood, "Beryllium/Molybdenum Multilayers for Normal Incidence reflectivity," *Physics of X-ray Multilayer Structures* (Jackson Hole, Wyoming, USA), OSA *Technical Digest*, pages (Optical Society of America, 1994).

37. R.B. Leighton, *Principles of Modern Physics*, , pages 421-435 (McGraw-Hill Book Company, Inc., New York, USA, 1959).

38. A.H. Compton, and S.K. Allison, *X-rays in Theory and Experiment*, 2nd ed., in , pages 288-292 (D. Van Nostrand Company, Inc.,, New York, USA, 1935).

39. B.L. Henke, E.M. Gullikson, and J.C. Davis, "X-ray interactions: photoabsorption, scattering, transmission, and reflection at E=50-30000 eV, Z=1-92," Atomic Data and Nuclear Data Tables, **54**(2), pages 181-342 (1993).

40. D.W. Berreman, "Multilayer reflecting x-ray optical systems: chromatic vigneting by narrow reflection bands," Applied Optics, **30**(19), pages 1741-1745 (1991).

41. Y. Watanabe, M. Suzuki, N. Mochizuki, M. Niibe, and Y. Fukuda, "Optical design for soft x-ray projection lithography," Japanese Journal Of Applied Physics, **30**(11B), pages 3053-3057 (1991).

42. F. Zernike, and D.N. Balburt, "Ultraprecise scanning technology," *X-ray/EUV Optics for Astronomy, Microscopy, Polarimetry, and Projection Lithography* (San Diego, CA, USA), vol. 1343, pages 241-244 (SPIE, Bellingham, Washington, 1990).

43. M. Born, and E. Wolf, *Principles of Optics*, 6th ed., in , pages 468-473 (Pergamon Press, Elmsford, NY, USA, 1984).

44. W.T. Welford, *Aberrations of optical systems*, , pages 241-260 (Adam Hilger, Ltd., Accord, MA, USA, 1986).

45. G.E. Sommargren, and R. Hostetler, "Point diffraction interferometry at soft x-ray wavelengths," *Soft X-ray Projection Lithography* (Monterey, CA, USA), *OSA Proceedings*, vol. 18, A.M. Hawryluk, and R.H. Stulen ed., pages 100-104 (Optical Society of America, Washington, D. C., USA, 1993).

46. D.P. Gaines, G.E. Sommargren, S.P. Vernon, and R.E. English, "X-ray characterization of a three-element condenser design for SXPL," *Soft X-ray Projection Lithography* (Monterey, CA, USA), *OSA Proceedings*, vol. 18, A.M. Hawryluk, and R.H. Stulen ed., pages 66-69 (Optical Society of America, Washington, D. C., 1993).

47. K. Early, and W.H. Arnold, "Cost of ownership for SXPL," *Soft X-ray projection lithography* (Monterey, CA, USA), *OSA Proceedings*, vol. 18, A.M. Hawryluk, and R.H. Stulen ed., pages 14-22 (Optical Society of America, Washington, D. C., USA, 1993).

48. L.A. Hackel, R.J. Beach, C.B. Dane, and L.E. Zapata, "Laser driver for soft x-ray projection lithography," Applied Optics, 32(34), pages 6914-6919 (1993).

49. R.L. Kauffman, and D.W. Phillion, "X-ray production efficiency at 130 Å from laser-produced plasmas," *Soft x-ray projection lithography* (Monterey, CA, USA), OSA *Proceedings*, vol. 12, J. Bokor ed., pages 68-71 (Optical Society of America, Washington, D. C., 1991).

50. R.L. Kauffman, D.W. Phillion, and R.C. Spitzer, "X-ray production ~13 nm from laser-produced plasmas for projection x-ray lithography applications," Applied Optics, 32(34), pages 6897-6900 (1993).

51. G.D. Kubiak, K.W. Berger, S.J. Haney, P.D. Rockett, and J.A. Hunter, "Laser plasma sources for SXPL: production and mitigation of debris," *Soft X-ray Projection Lithography* (Monterey, CA, USA), OSA *Proceedings*, vol. 18, A.M. Hawryluk, and R.H. Stulen ed., pages 127-131 (Optical Society of America, Washington, D. C., 1993).

52. M. Richardson, W.T. Silvast, H.A. Bender, A. Hanzo, V.P. Yanovsky, F. Jin, and J. Thorpe, "Characterization and control of laser plasma flux parameters for soft x-ray projection lithography," Applied Optics, 32(34), pages 6901-6910 (1993).

53. P.D. Rockett, J.A. Hunter, R. Kensek, R.E. Olson, G.D. Kubiak, and K.W. Berger, "XUV conversion efficiency in a low-intensity KrF laser plasma for projection lithography," *Soft X-ray Projection Lithography* (Monterey, CA, USA), OSA *Proceedings*, vol. 12, J. Bokor ed., pages 76-81 (Optical Society of America, Washington, D. C., 1991).

54. W.T. Silfvast, H. Bender, A.M. Eligon, D. O'Connell, A. Hanzo, and M.C. Richardson, "Laser plasma source characterization for SXPL," *Soft X-ray Projection Lithography* (Monterey, CA, USA), OSA *Proceedings*, vol. 18, A.M. Hawryluk, and R.H. Stulen ed., pages 117-126 (Optical Society of America, Washington, D. C., 1993).

55. R.C. Spitzer, R.L. Kauffman, T. Orzechowski, D.W. Phillion, and C. Cerjan, "X-ray production from laser produced plasma for SXPL applications," *Soft X-ray Projection Lithography, Topical Meeting* (Monterey, CA, USA), OSA *Proceedings*, vol. 18, A.M. Hawryluk, and R.H. Stulen ed., pages 142-145 (Optical Society of America,

Washington, D. C., 1993).

56. R.C. Spitzer, R.L. Kauffman, T. Orzechowski, D.W. Phillion, and C. Cerjan, "Soft X-ray production from laser produced plasma for lithography applications," Journal of Vacuum Science and Technology B, 11(6), pages 2986-2989 (1993).

57. D.L. White, "A high efficiency condenser for laser plasma sources and ringfield masks," *Soft X-ray Projection Lithography* (Monterey, CA), OSA *Technical Digest*, pages 23-26 (Optical Society of America, Washington D. C., 1993).

58. N.M. Ceglio, A.M. Hawryluk, and G.E. Sommargren, "Front-end design issues in soft x-ray projection lithography," Applied Optics, 32(34), pages 7050-7056 (1993).

59. K.J. Kim, *Characteristics of synchrotron radiation*, *Physics of Particle Accelerators*, M. Month, and M. Dienes ed., , pages 565 (American Institute of Physics, New York, USA, 1989).

60. L.G. Thompson, C.G. Willson, and M.J. Bowden, ed., *Introduction to Microlithography*, ACS Symposium Series, M.J. Comstock ed., vol. 219, 363 pages (American Chemical Society, Washington, D. C., 1983).

61. G.R. Misium, M. Tipton, and C.M. Garza, "Surface imaging lithography at 248 nm," Journal of Vacuum Science and Technology B, 8(6), pages 1749-1753 (1990).

62. G.D. Kubiak, "Summary of U. S. activities in EUV lithography: resists," *U.S.–Japan Workshop on EUV Lithography, Technical Digest* (Mt. Fuji, Japan), pages (Japanese Society for Synchrotron Research, Japanese Society of Applied Physics, 1993).

63. A.A. MacDowell, J.M. Calvert, T.S. Koloski, and O.R.I. Wood, "New surface imaging resist technology for SXPL," *Soft X-ray Projection Lithography* (Monterey, CA, USA), OSA *Proceedings*, vol. 18, A.M. Hawryluk, and R.H. Stulen ed., pages 87-93 (Optical Society of America, Washington, D. C., 1993).

64. B.M. Lum, A.R. Neureuther, and G.D. Kubiak, "Modelling EUV SXPL," *Soft X-ray Projection Lithography* (Monterey, CA, USA), OSA *Proceedings*, vol. 18, A.M. Hawryluk, and R.H. Stulen ed., pages 54-58 (Optical Society of America, Washington,

D. C., 1993).

65. E. Reichmanis, L.F. Thompson, O. Nalamasu, A. Blakeney, and S. Slater, "Chemically amplified resists for deep-UV lithography: A new processing paradigm," Microlithography World, (Nov/Dec), pages 7-13 (1992).

66. E. Spiller, "Reflective multilayer coatings for far uv region," Applied Optics, **15**(10), pages 2333-2338 (1976).

67. E. Spiller, A. Segmuller, J. Rife, and R.-P. Haelbich, "Controlled fabrication of multilayer soft x-ray mirrors," Applied Physics Letters, **37**(11), pages 1048-1050 (1980).

68. A.V. Vinogradov, and B.Y. Zeldovich, "X-ray and far uv multilayer mirrors: principles and possibilities," Applied Optics, **16**(1), pages 89-93 (1977).

69. J.H. Underwood, T.W. Barbee, and D.L. Shealy, "X-ray and extreme ultraviolet imaging using layered synthetic microstructures," *High Resolution Soft X-ray Optics, Proceedings of the SPIE* (Brookhaven , NY), vol. 316, pages 79-89 (The International Society for Optical Engineering, 1981).

70. J.H. Underwood, and T.W. Barbee Jr., "Layer synthetic microstructures as Bragg diffractors for X-rays and extreme ultraviolet: theory and predicted performance," Applied Optics, **20**(17), pages 3027-3034 (1981).

71. H. Wolter, "Mirror systems with glancing incidence as image-producing optics for x-rays," Ann. Phys., **10**, pages 94 (1952).

72. R.W. James, *The optical principles of the diffraction of x-rays*, 664 pages (Ox Bow Press, Woodbridge, CT, USA, 1962).

73. J.H. Underwood, and D.T. Attwood, "The renaissance of x-ray optics," Physics Today, (April), pages 44-51 (1984).

74. T.W. Barbee, "Sputtered layered synthetic microstructure dispersion elements," *Low Energy X-ray Diagnostics* (Monterey, CA, USA), vol. 75, D. Attwood, and B. Henke ed., pages 131-145 (American Institute of Physics, NY, NY, USA, 1981).

75. D.G. Stearns, R.S. Rosen, and S.P. Vernon, "Multilayer mirror technology for soft x-ray projection lithography," Applied Optics, 32(34), pages 6952-6959 (1993).

76. R. Parsons, *Sputter deposition processes*, *Thin Film Processes II*, J.L. Vossen, and W. Kern ed., , pages 177-208 (Academic Press, San Diego, CA, USA, 1991).

Chapter 2

EUV Lithographic Masks — Fabrication Process and Optimal Geometry

2.1 Masks for EUVL

Extreme ultraviolet lithography is being developed for integrated circuits with 0.12 μm design rules [1, 2]. While the exposure system is the technology driver, all support technologies must be developed concurrently for they are important to the acceptance of a new technology. Mask cost is a significant component of the cost of ownership for lithography [3] and could be a decisive factor in influencing the choice of lithographic technology.

The making of lithographic masks requires appropriate resolution, good control of linewidth variations (CD control), precise pattern placement from mask to mask (pattern placement and overlay) and defect control. For the 0.12 μm generation, these requirements will pose serious challenges to all aspects of mask making — lithography, metrology, defect detection and repair. An overlay accuracy of 35 - 50 nm, or roughly ± 15% of the minimum feature size, will be required on the wafer. This is the total error budget that includes the contributions from mask critical dimension (CD) errors, lithographic alignment errors and all other process errors. Typically 25% of this error

budget is allocated to mask–making [4, 5].

The current specification for CD control on a 5X mask is roughly 10% of the wafer linewidth, i.e. a 0.5 μm process on wafers requires a 2.5 μm process on masks with 50 nm CD control, i.e. 2% CD control on the mask. This requirement is driven by yield analysis and would be even more stringent for a 1X process [5, 6].

Currently, 6" mask blanks are used for 5X systems. For the 0.12 μm generation, chip sizes are projected to be 7 cm^2 for memories and 10 cm^2 for microprocessors, requiring field sizes of 37 x 37 mm^2 [2]. For 5X systems, masks will be 18.5 x 18.5 cm^2, thus may require 8" mask blanks that are defect-free.

Compared to other lithographic techniques capable of 0.12 μm resolution, one advantage of EUVL is its masks. An EUVL mask would be a reflective reduction mask patterned on a thick substrate. Reduction imaging eases the requirements on CD control on the mask and pattern placement accuracy of the mask writing tools. The thick substrate should be resistant to distortion, thus making the wafer level overlay requirements more manageable.

An EUVL mask blank is made up of the mask substrate and the reflective coating. Since the turnaround time in today's mask shops is under 24 hours [7], future EUVL mask blanks must be already multilayer-coated and inspected for defects before they are delivered to the mask-making facilities.

The density of defects in the reflective coatings deposited in a controlled environment has yet to be fully characterized. As will be shown in chapter 4, defects in the substrate and reflective coating of an EUVL mask may result in distortions of the resist image even for subresolution defects of a few nanometers thick [8, 9]. The first printability study of substrate defects in EUVL masks is reported in chapter 6.

Since the mask is the first element to be illuminated by the condenser system and will be subjected to a considerable heat load, the thermal requirements for mask substrate materials have been the subject of some preliminary studies [10, 11]. Mask substrates must also have low rms roughness to ensure high reflectivity for the coatings deposited on them [12].

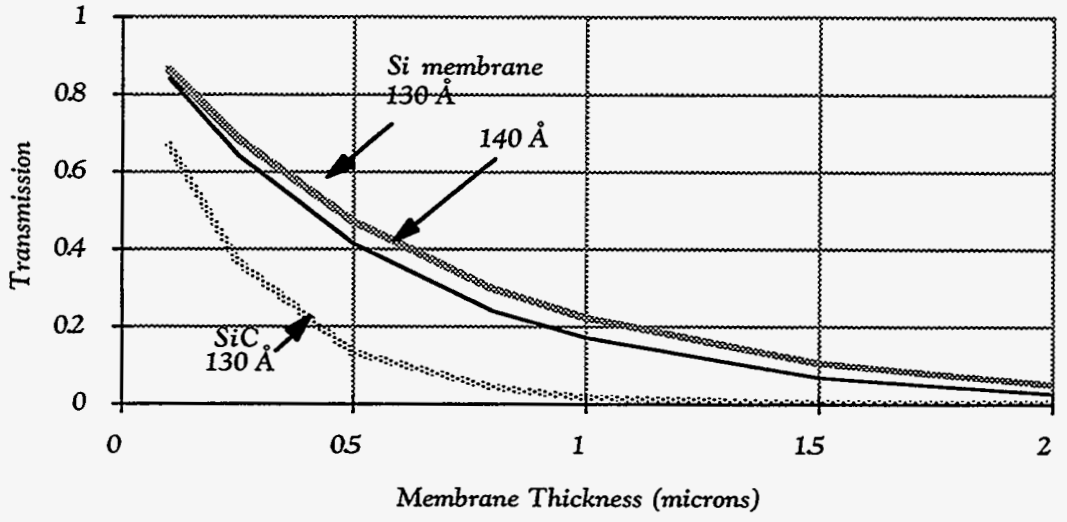

Figure 2.1. Calculated transmission for Si and SiC membranes at 130 – 140 Å. Si is the most transmissive material in this region because its absorption edge is at 125 Å. To obtain 50% transmission, a 0.5 μm membrane is required. For 80% transmission, a 0.15 μm Si membrane is required.

Since mask cost is a significant component of the cost-of-ownership for lithography [3], and the relative ease of mask fabrication is a key advantage for EUVL over other technologies, finished masks need to be kept from being contaminated after they have been inspected and repaired. In optical lithography, a pellicle is used for this purpose. The pellicle is a thin, transparent membrane mounted over the mask to form a sealed, dust-free chamber protecting it from any future contamination. It is mounted at a sufficient stand-off distance from the mask pattern so that particles on the pellicle are kept out of the imaging depth of the optical system. The use of pellicles in optical lithography have increased yield, extended mask lifetime and reduced the cost of mask inspection. Current pellicles for UV i-line steppers (365 nm) are typically 1-3 μm thick and 99% transmissive [13].

Since materials are highly absorptive at EUV wavelengths, it will be a challenge to find a material suitable for use as a pellicle membrane for EUVL masks. The transmission through some membranes are shown in figure 2.1. Transmission is ~ 40% for a 500 nm Si membrane and ~ 80% for a 150 nm Si membrane. In a reflective mask, the radiation would pass through the pellicle twice, thus resulting in a 40% power loss even with the 150 nm membrane and significantly affecting throughput. The absorbed radiation would also produce heating that might reduce the pellicle's useful lifetime. EUVL masks must

also be vacuum compatible thus requiring that the current air-tight pellicle design be modified even if a suitable pellicle material could be found. It may be possible to design a mask holder with a retractable cover that moves out of the way during exposure. Such a holder would be required to not generate particulate contaminants from its moving parts. In spite of these challenges, however, the cost of mask fabrication, inspection and repair is such that some technique to prevent contamination of the finished masks would be required for EUVL.

This chapter is an introduction to EUVL mask technology, containing a survey of current works on EUVL masks and a description of techniques used to fabricate masks for this thesis research. It also includes a comparative study of the imaging performance of two demonstrated mask geometries for EUVL — absorber overlayer masks and etched masks.

2. 2 Mask Fabrication

2.2.1 Survey of Relevant Works

Masks for extreme ultraviolet lithography (EUVL) are made by patterning multilayer reflective coatings. The patterning can be accomplished in many ways - by depositing and patterning an absorber layer over the multilayer coating, by etching the pattern directly into the multilayer coating, and by reducing the reflectivity of selected areas of the multilayer coating by ion bombardment [10, 14-17]. Masks made by all these techniques have been imaged satisfactorily [14, 15]. In 1991, Hawryluk et al. fabricated masks with patterned absorber overlayers on multilayer coatings [16], and Kinoshita et al. performed imaging experiments with etched masks in 1991 [17].

Also in 1991, Tennant et al. conducted a thorough study of the various mask geometries in 1991 [14, 15]. Masks fabricated by etching, by patterning absorber layer and by selective ion-damage were described and their relative merits discussed. Imaging experiments were also performed showing that all three types of reflective masks could be used to image 0.1 μm patterns.

An important disadvantage for etched masks is that their opaque defects cannot be repaired, since there is no technique to spot-deposit high quality multilayer coatings. On

the other hand, techniques have been demonstrated to repair defects in the absorber layer [18, 19].

2.2.2 Mask Fabrication – Thesis Work

A part of my thesis work involved fabricating absorber overlayer masks for EUVL. Mask blanks were Mo/Si multilayer reflective coatings deposited on Si substrates or super-polished flats. The multilayer coatings were deposited by planar magnetron sputtering at CXRO, LBL. Reflectivities of over 60% were routinely achieved with Mo/Si on Si wafer substrates. Slightly higher reflectivities, of ~ 63% [20], were obtained for coatings deposited on optical flats because of the lower rms roughness. The multilayer deposition process will be described in chapter 3 in conjunction with the work on long-term reflectivity characteristics of Mo/Si multilayer coatings.

The absorber patterning was performed with G-line optical lithography using a 4X Canon tool in the Microfabrication Lab at UC Berkeley. The absorber materials, ~ 100 nm of gold above a 2-4 nm Cr sticking layer, were deposited by evaporations and lift-offs. With this process, 1 μm wide absorber lines were routinely produced. A diagram of the mask fabrication process is shown in figure 2.2. Figure 2.3 shows a SEM image of some gold absorber patterns with linewidths ranging from 1 μm to 10 μm deposited above a Mo/Si multilayer reflective coating.

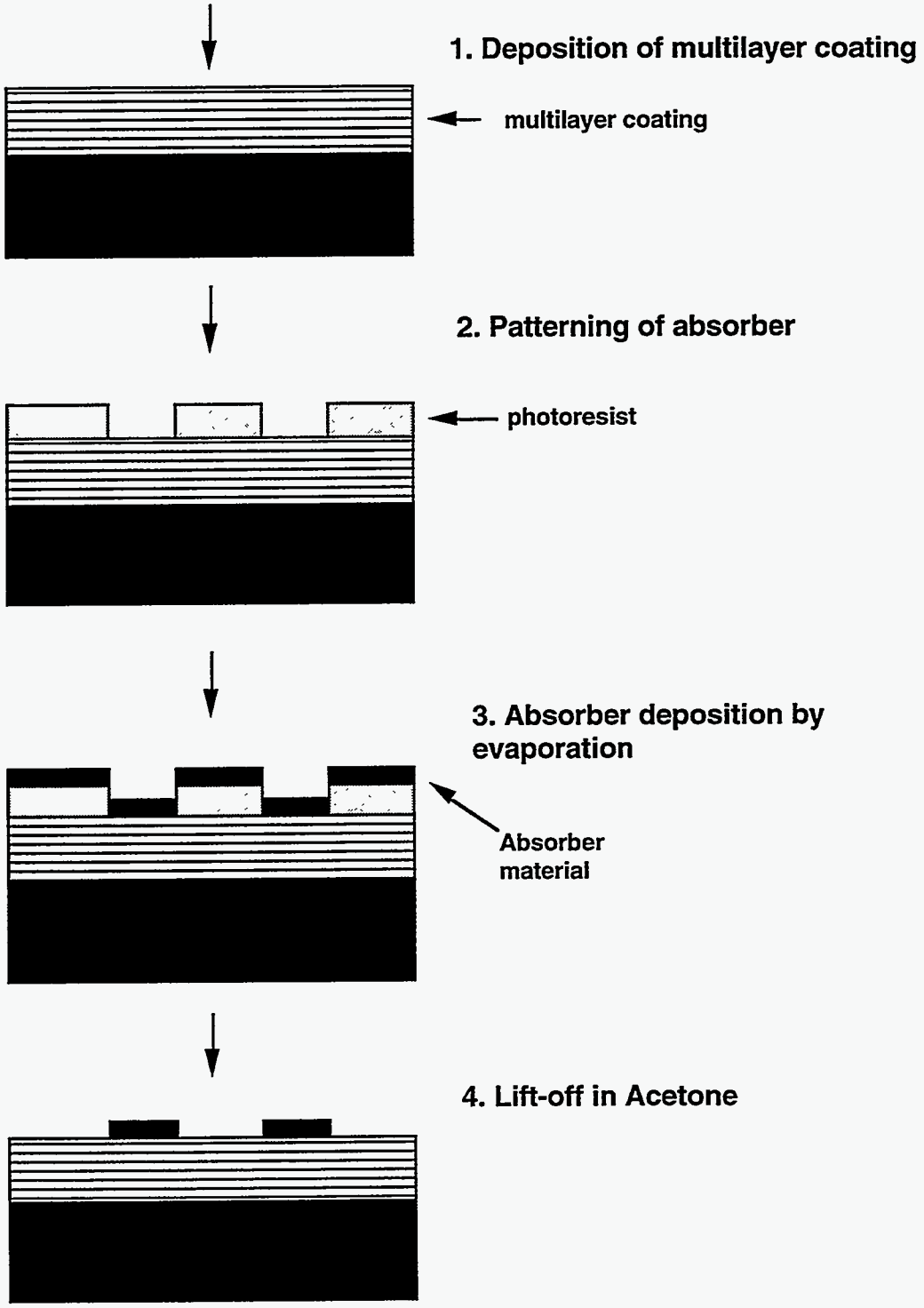

Figure 2.2. Mask fabrication process. The multilayer coatings typically consist of 30 – 40 bilayers of Mo/Si with 7 nm d-spacing. The patterning was performed with a G-line Canon printer in the Microfabrication Laboratory in Cory Hall, UCB. The absorber pattern consists of 100 nm of gold deposited above ~ 4 nm of Cr to enhance adhesion to the Si substrate.

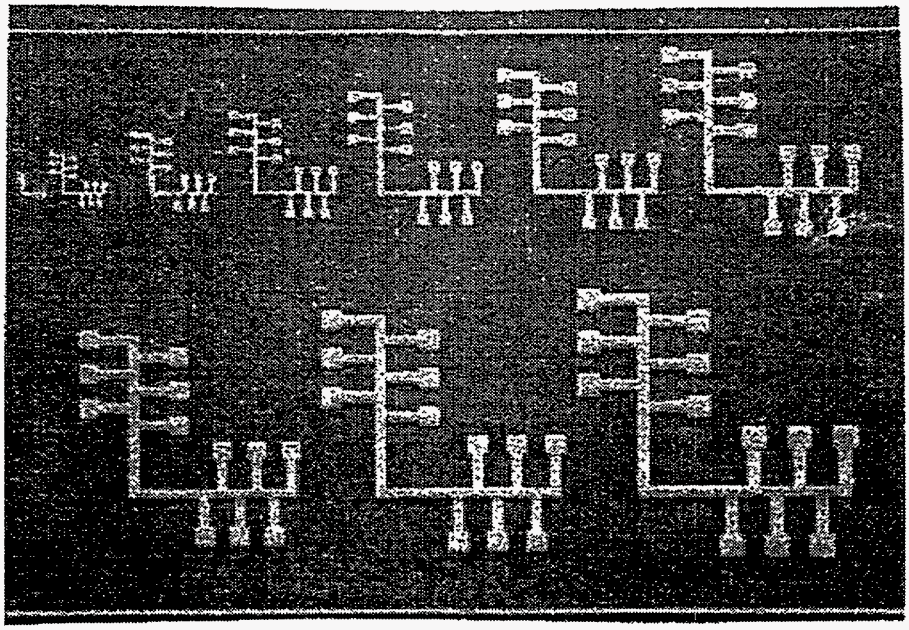

Figure 2.3. 100 nm thick gold absorber patterns deposited on Mo/Si multilayer reflective coatings by evaporation and lift-off. Linewidths range from 10 μm to 1 μm.

2.3 Comparison of Imaging Properties of Absorber Overlayer Masks and Etched Masks

Since a lithographic mask is to be imaged with fidelity onto the wafer, factors that affect its imaging performance must be well understood. In order to compare the imaging performance of etched masks and absorber overlayer masks, aerial images from both types of masks were calculated for different mask topographies.

For the absorber overlayer mask, the mask topography is determined by the absorber layer- its profile, material and thickness. For the etched mask, the topography is determined by the profile and thickness of the etched multilayer coating. At oblique incident illumination, some shadowing effects due to mask topography are expected. Aerial image variations as a function of incident angles were calculated to quantify the effect of shadowing. Aerial image calculations were also performed for different absorber materials, absorber sidewall profiles (for absorber masks) and stack profiles (for etched masks).

2.3.1 Simulation Process

2.3.1 (a) Calculations of Reflected Field and Image Synthesis

The electromagnetic field scattered from the complicated topography of the mask was calculated using TEMPEST, a massively parallel time-domain finite-difference program which runs on a Connection Machine CM-2 [21-24]. This program is the result of a collaborative effort involving many students in Professor Neureuther's research group at UC Berkeley. The current version of TEMPEST was written by Alfred Wong. It accepts inputs of both TE and TM polarizations and off-normal incident illumination. The simulation domain is specified in terms of the layer thicknesses and the refractive indices of the materials in it. Absorbing boundary conditions are applied to the top and bottom boundaries of the domain. To simulate masks with lines and spaces, periodic boundary conditions are applied to the side boundaries. TEMPEST is well-suited to answer questions regarding the effect of topography on images. It is used in this chapter to study the effect of mask topography on images and in chapter 4 to study the effect of defects.

TEMPEST calculates the electromagnetic field by propagating a plane wave of arbitrary intensity profile into the simulation domain according to Maxwell equations discretized in space and time. The time step and node spacing are chosen to ensure convergence and an acceptable degree of accuracy. The propagation process is iterated until the fields converge to the required accuracy set by the user. In these calculations, the accuracy is set to be 2%. At the end of the calculation , TEMPEST outputs the field amplitude in the simulation domain and the reflected field given in terms of its diffracted orders. The field amplitude can be examined to study how the field propagates in the mask structure and to observe the effect of topographies and defects on the field distribution. Diffraction effects can also be seen in the field amplitude plots.

In order to study the effect of different mask topographies on imaging, the aerial image is synthesized from the reflected field by Hopkins's technique which takes the partial coherence of the illumination into account [25]. Two assumptions are made in the image synthesis process. The diffraction efficiency is assumed not to vary with the incident illumination angle over the illumination cone. With this assumption, the aerial image simulation program is able to use diffracted orders from an incident plane wave at one incident angle calculated by TEMPEST to simulate partially coherent illumination. It does so by superimposing the diffracted orders calculated by TEMPEST for one angle over a range of angles, thus simulating an illumination cone. In this study, an aberration-

free 4:1 reduction imaging system operating at 135 Å with numerical aperture (NA) of 0.1 was simulated, giving nominally 0.1 μm resolution. For σ ranging from 0.5 to 1, the illumination cone would be on the order of a degree, and the assumption of constant diffraction efficiency over the illumination cone is quite accurate. The illumination intensity is also assumed to be uniform over the cone.

2.3.1 (b) Application of TEMPEST to soft X-ray/EUV multilayer reflectors

Calculations of reflected fields from multilayer reflective coatings place special demands on TEMPEST. First, the reflective coatings consist of 30 to 40 layer pairs of Mo/Si deposited on a silicon substrate. As a result, the simulation domain for a multilayer coated mask consists of 60 to 80 layers of materials.

In addition, at EUV wavelengths, the refractive index is near unity for all materials and is commonly written as,

$$n = 1 - \delta(\lambda) - i\beta(\lambda) \qquad (1)$$

where δ and β are on the order of 10^{-2} - 10^{-3} in the wavelength region between 4.5 nm and 15 nm (see figure 1.6). To ascertain that the large number of layers and the near-unity refractive indices do not reduce the accuracy of TEMPEST, two sets of calculations were performed.

Since the simulation domain is a rectangular grid of 1024 x 512 nodes, some discretization errors are introduced when the periodic multilayer structure of arbitrary period is mapped onto it. The effect of these errors is investigated by calculating reflectivity from a number of identical planar multilayer structure shifted vertically by increments smaller than one node spacing. With node spacings of approximately $\lambda/15$, the structure was shifted vertically in steps of $\lambda/20$ over a distance of 2λ to observe errors introduced by discretization. Since the structure repeats itself when shifted by one layer pair, the resulting periodic behavior shown in figure 2.4 is expected. While the magnitude of the variations in reflectivity increases with the number of layer pairs, it is less than 2% for a 40 layer-pair structure.

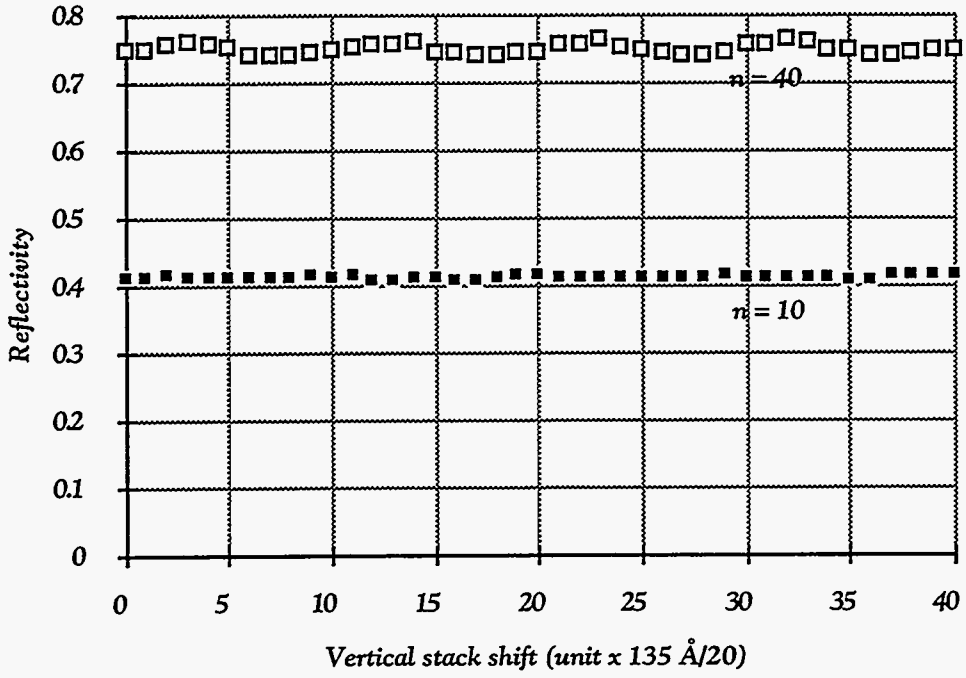

Figure 2.4. Discretization error is estimated by calculating reflectivities for a set of identical planar multilayer structure shifted in vertical position by $\lambda/20$ for a distance of 2λ. Simulation nodes are spaced approximately $\lambda/15$ apart. Results are shown for Mo/Si reflective coatings with 10 bilayers and 40 bilayers. Discretization error for 40 bilayers is 2%.

As another measure of TEMPEST's performance for multilayer structures, calculations of reflectivity versus wavelength for planar Mo/Si coatings consisting of 10, 20, 30, and 40 layer pairs were performed. As shown in figure 2.5, the reflectivities calculated by TEMPEST are approximately 5% lower than those obtained from a technique using Fresnel coefficients . The source of this difference was determined to be the result of the discretization error already discussed above. Discretization errors effectively introduce coating period variations into the simulated coating, thus reducing the calculated reflectivity of the coating.

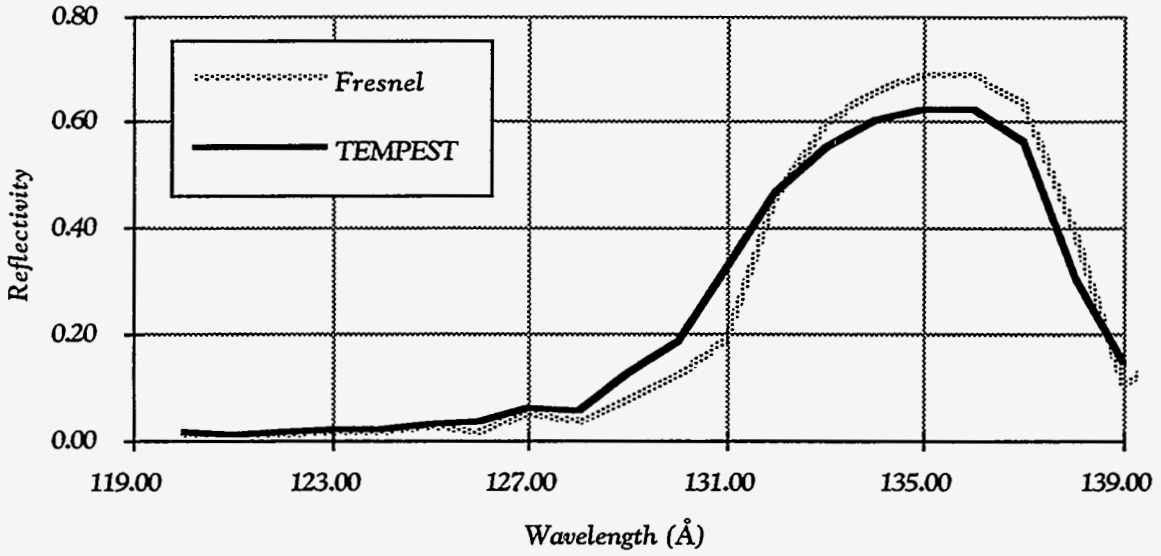

Figure 2.5. Calculations of reflectivity vs. wavelength for planar multilayer structures using TEMPEST and a Fresnel coefficient technique at normal incidence. TEMPEST results are approximately 5% lower than those obtained by Fresnel technique due to discretization errors.

2.3.1 (c) Simulation Geometries

The simulated reflective coatings consisted of 30 or 40 bilayers of Mo/Si on Si substrates. Each Mo and Si layer is 3.5 nm thick. Silicon was the top layer of the multilayer stacks in accordance with experimental results showing reduction in the reflectivity of Mo-topped multilayer coatings by oxidation of the top layer (see chapter 3) [20, 26].

For the absorber overlayer masks, the simulated geometries were 0.4 μm absorber lines-and-spaces over Mo/Si multilayer coatings on the masks. The simulated absorber materials were either gold, germanium, or carbon. The incident angles were varied from normal incidence to 10° off-normal. The absorber profile tilts were varied from vertical to 45°.

For the etched multilayer masks, 0.4 μm etched patterns were simulated for 30-bilayer and 40-bilayer coating with different stack tilts. Incident angles were varied from 0° to 10° off-normal, and stack profile tilts were varied from vertical to 10°.

As was mentioned in section 2.3.1 (a), periodic boundary conditions are used for the left and right boundaries to increase the accuracy of the calculations. As a result, the

features simulated in this study were grouped line-and-spaces. Aberration-free 4:1 reduction imaging was simulated using Hopkins's technique to synthesize the aerial images of these mask geometries.

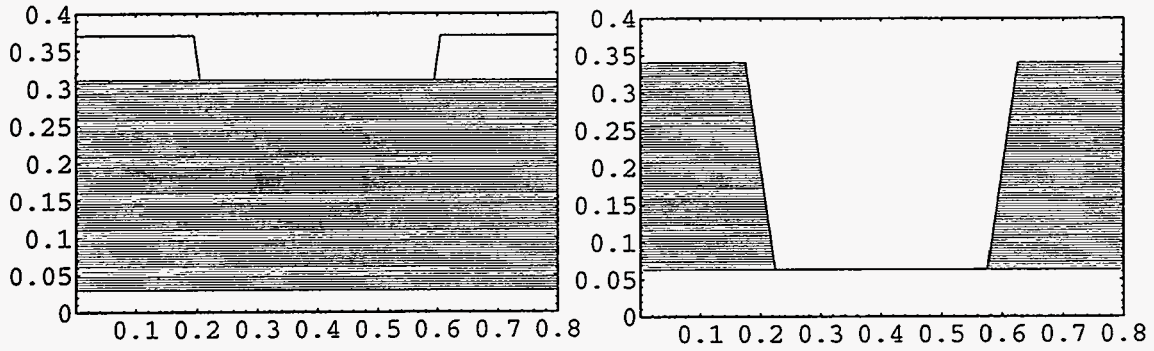

Figure 2.6. Simulated mask geometry (a) absorber overlayer mask consisting of a thin absorber overlayer and (b) etched mask.

2.3.2 Absorber vs. Etched Masks

Absorber overlayer and etched masks were evaluated by comparing their simulated aerial images under a range of incident angles and pattern profile tilts. Images were calculated at normal incident, 5° off-normal and 10° off-normal. Images were also calculated for absorber overlayer masks and etched masks with different pattern profile tilts .

2.3.2 (a) Aerial Images vs. Angles of Incidence

The requirement of high reflectivity at 13.5 nm limits incident angles to a cone of roughly 10° from normal incidence. The reason for this can seen from Bragg's condition,

$$m\lambda = 2d\sin\theta_m \qquad (2)$$

where θ_m is measured from glancing incidence (θ = 90° for normal incidence).

Since the wavelength should be in the range of 13 nm to 14 nm to take advantage of the low absorption near the Si absorption edge, d must increase as θ moves away from normal incidence. Since absorption increases with layer thickness for a given wavelength, the achievable reflectivity is reduced. While Γ, the ratio of the high-Z layer

thickness to layer pair thickness, can be adjusted to optimize R for a given angle of incidence, the achievable peak reflectivity decreases at off-normal incidence angles. This limits the acceptable cone of incidence angle to ~ 10° for operation around 13 nm. The acceptance cone would be even narrower at shorter wavelengths since more layers are required for optimum reflectivity.

Within this illumination cone, variations of aerial images with incident angles were studied. Due to the topography of the absorber layer, the incident field near the edges of the absorber pattern would be partially absorbed either before reaching the reflective coating or upon leaving it. As a result, reduction of image intensity by shadowing was expected for oblique incident.

For the range of incident angles from 0° to 10° off-normal, however, there is no significant difference in the reflected images for masks with 60 nm thick germanium overlayer (figure 2.7). This can be seen in a plot of the intensity of the diffracted orders. For incident angles of less than 10° off-normal and 60 nm absorber layer, the observable differences in the reflected fields for the three incidence angles only appear in the higher diffracted orders. However, in a 4:1 reduction system operating at 13.5 nm with NA = 0.1, NA is approximately 0.025 on the mask's side and only the 3rd and lower orders contribute to the image of the 0.1 μm lines (σ is 1 or less), resulting in nearly identical images for incident angles between 0° and 10° off-normal.

As the absorber layer thickness was increased, however, the effect of shadowing on the aerial image became more noticeable. As the Ge absorber layer thickness was increased from 60 nm to 120 nm to 200 nm, a 4% reduction in peak image intensity was observed, together with some narrowing of the peak width (figure 2.8).

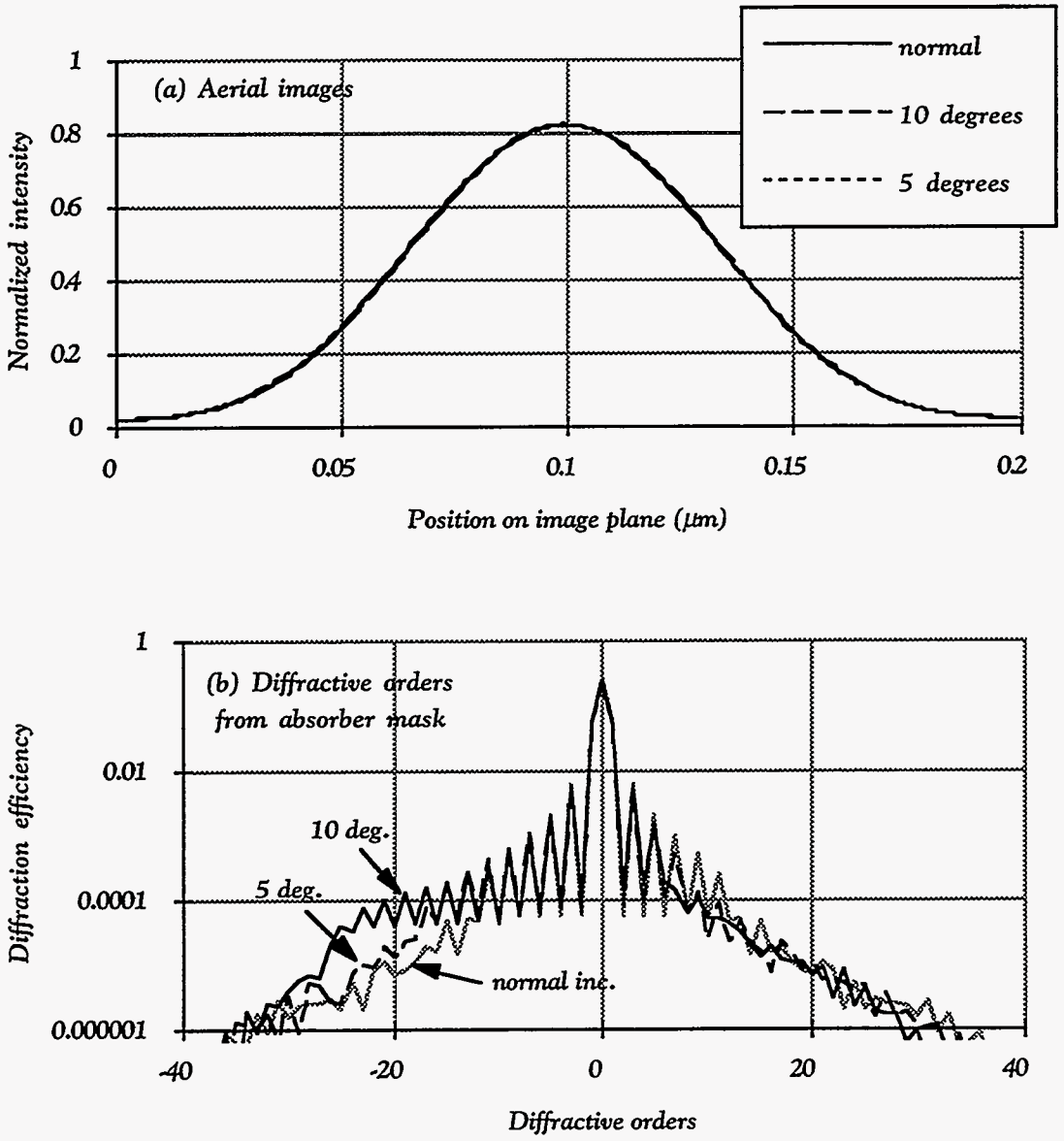

Figure 2.7. (a) Aerial images as a function of incidence angle for absorber overlayer masks at normal incidence, 5° off-normal and 10° off-normal, (b) diffracted harmonics of the reflected field for these illumination conditions.

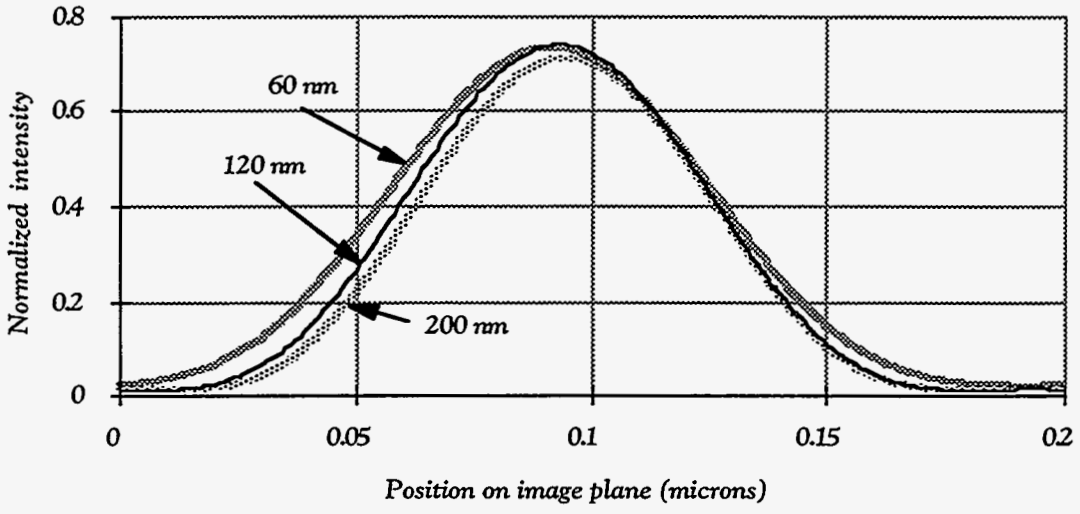

Figure 2.8. Aerial images from absorber overlayer masks as the germanium thickness is increased from 60 nm to 120 nm to 200 nm. Illumination angle is 10° off-normal.

More significant shadowing was observed for etched masks. For etched lines with vertical profile, the normalized peak image intensity decreases from 0.82 at normal incidence to 0.7 at 10° off–normal as shown in figure 2.9. Image intensity variations of this magnitude can produce observable variations in resist linewidths.

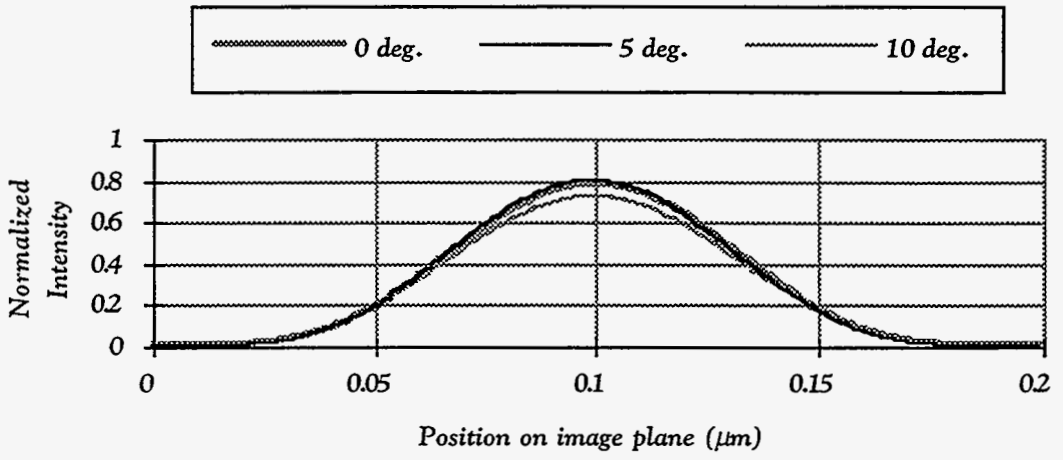

Figure 2.9. Aerial images for etched masks at normal incidence, 5° off-normal and 10° off-normal.

2.3.2 (b) Aerial Images vs. Pattern Profile Tilts

The absorber layer can be patterned by a number of techniques including wet chemical etching, reactive ion etching (RIE), and lift-off. With any technique, however, some variations in the absorber profile may occur. The effect of absorber pattern profile tilts on the reflected images was studied for absorber overlayer masks with 60 nm thick germanium. The midpoint of the absorber layer was kept fixed as the tilt angle of the absorber profile was varied from 0°, or perfectly vertical sidewall, to 45°. The incident illumination angle was 10° off-normal for all cases.

As can be seen in figure 2.11, there was hardly any difference between the reflected images for the 5°, 10°, 25° absorber profile tilts. At 45° absorber tilt, peak image intensity decreased by 3% compared to that at 10° tilt. The relative insensitivity of the reflected image to the absorber profile should allow for less stringent requirements on the absorber deposition and patterning process.

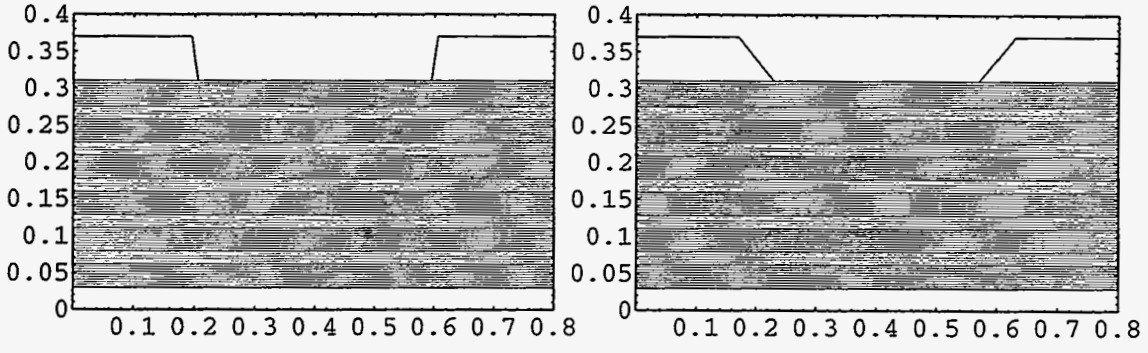

Figure. 2.10. Input profiles for calculations of the effect of absorber tilt. The midpoint of the absorber layer was held fixed while the profile tilt is varied from vertical to 45° tilt.

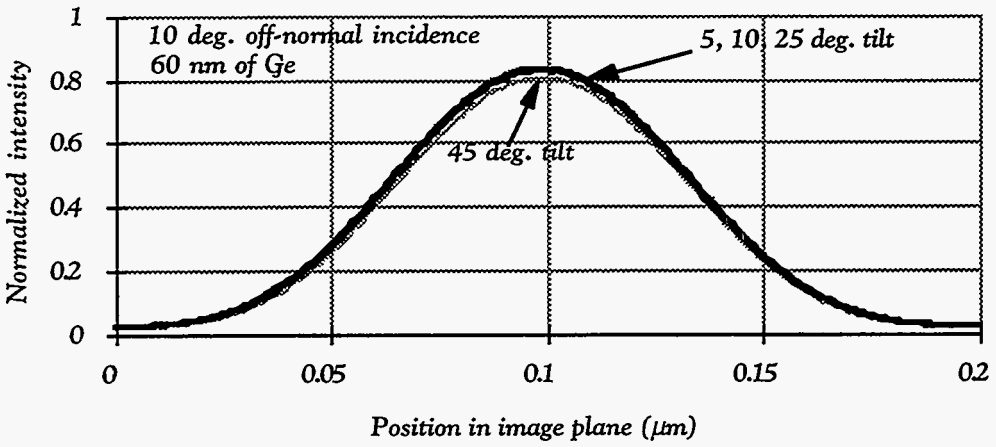

Figure 2.11. Aerial images for absorber overlayer mask (60 nm of Ge) with non vertical absorber profile. The mid-point of absorber layer is held fixed, and the tilt angles are 5°, 10°, 25° and 45°. Peak image intensity is reduced by 3% at 45° absorber tilt.

Profile tilts had a more pronounced effect on images from etched masks. As the etched patterns profile tilts were varied from 0° to 10° , the peak image intensities varied by nearly 10%.

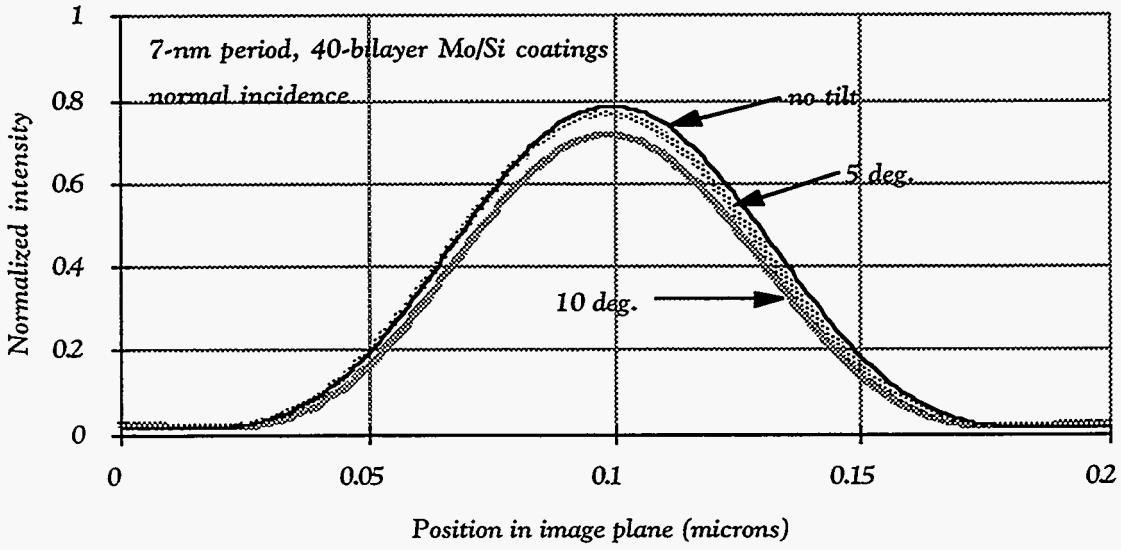

Figure 2.12. Aerial images from etched masks with tilt in stack profiles. Peak image intensities vary by 10% as stack tilt s vary from 0° to 10°.

2.3.3 Aerial Images vs. Absorber Materials

The absorber materials simulated in this study were gold, germanium, and carbon as a stand-in for photoresist. Both gold and germanium can be easily deposited and patterned. Photoresist as absorber, of course, would be the simplest process of all. The optical properties of carbon also resulted in interesting phase-shifting effects on the aerial images. However, some polymer chains may break down under long x-ray exposure.

As shown in figure 2.13, gold has the largest β at 13.5 nm, and hence is the most absorptive of the three materials, while carbon, with the smallest β, is the least absorptive. An absorber thickness of 60 nm for both gold and germanium results in high contrast images. For carbon, β is only roughly 1/5 of that of gold and 1/3 of that of germanium at 13.5 nm wavelength. The aerial image of an absorber overlayer mask with 60 nm of carbon shows sidelobes in the absorber region similar to those seen for attenuated phase shifted masks (figure 2.14(a)). This effect may be used to sharpen line edges, as is currently being used in optical lithography. The aerial image of a mask with a carbon absorber layer of 130 nm shows smaller sidelobes.

These calculations show that a layer of gold, germanium or carbon from 60 nm to 130 nm thick can serve as an effective absorber for a reflective mask. As a result, ease of processing and durability under long x-ray exposure in vacuum should be the determining factors for choosing the absorber material. Tennant et al. have shown that Ge has several processing advantages. It has good adhesion to the coating and can be readily etched by RIE. Ge is also very fine-grain and should result in good CD control [14, 15].

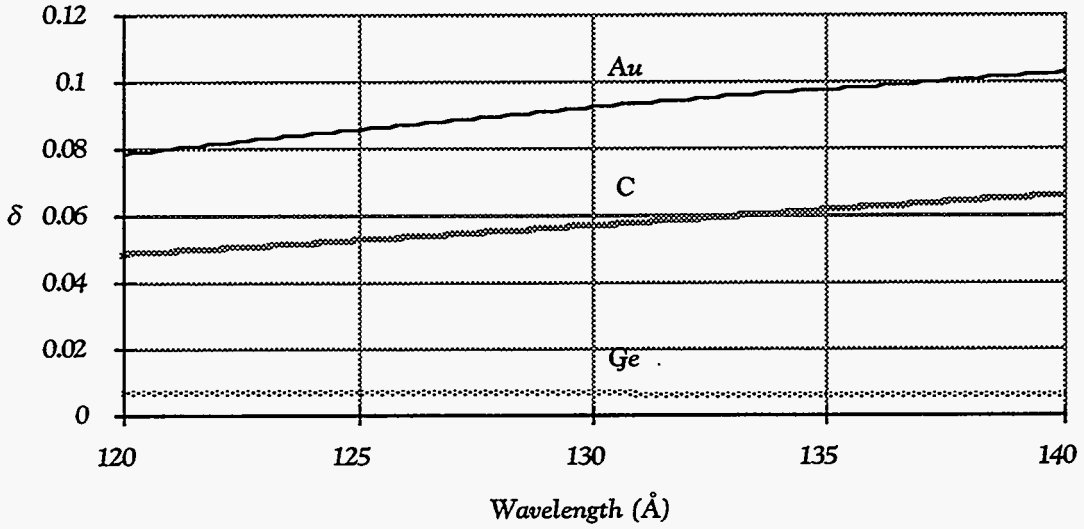

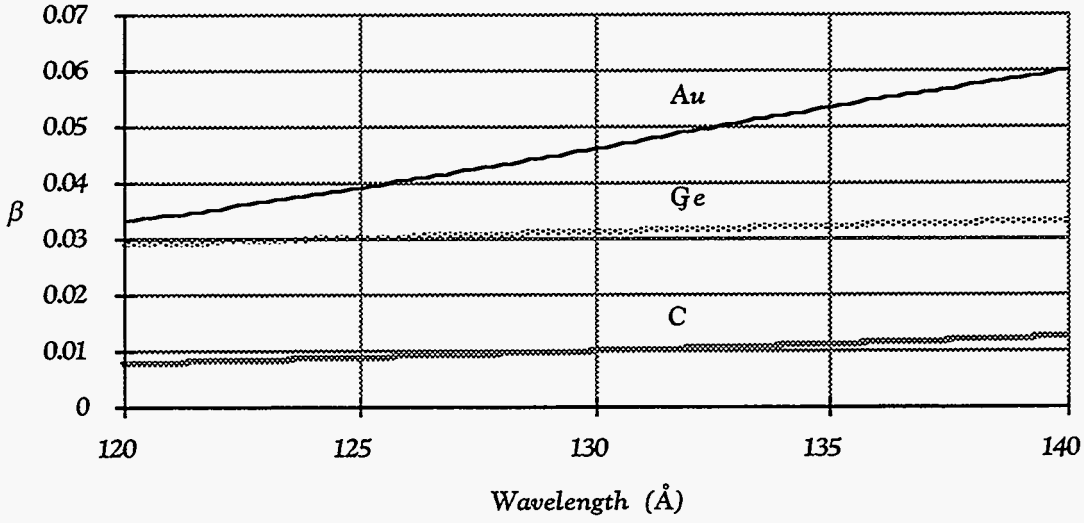

Figure 2.13. Refractive indices of gold, germanium and carbon given in terms of δ and β, where $n = 1 - \delta - i\beta$.

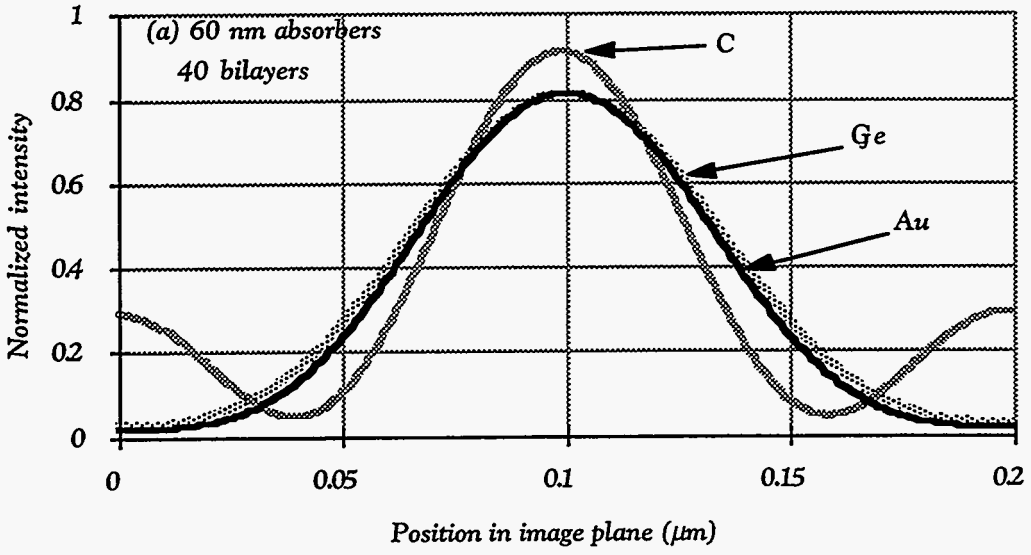

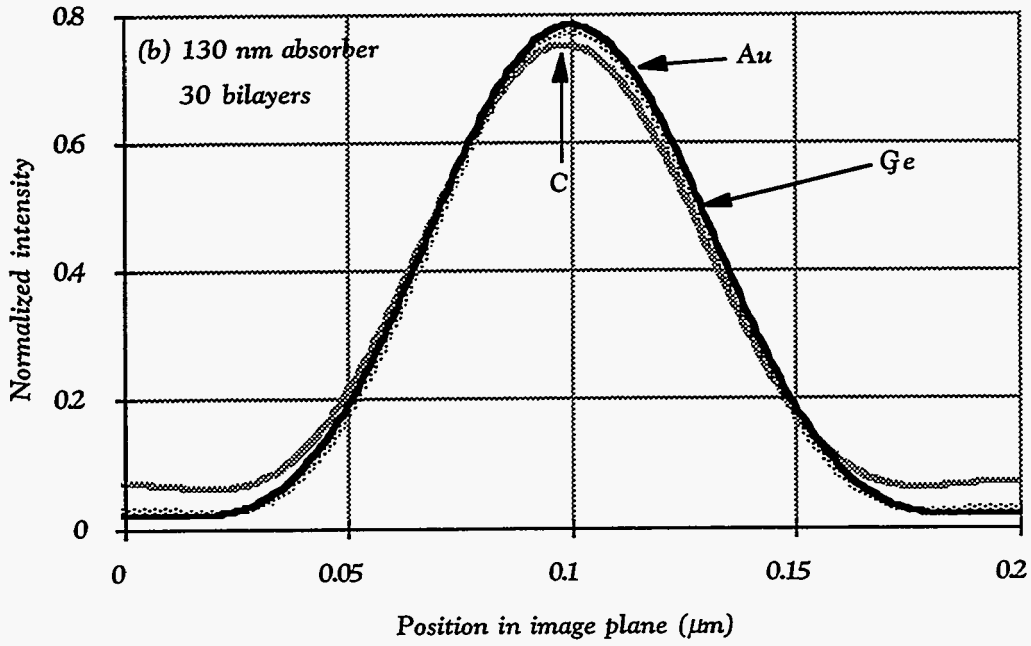

Figure 2.14. Aerial images for gold, germanium and carbon absorbers at (a) 60 nm and (b) 130 nm thickness. The aerial image for the 60 nm carbon mask shows sidelobes similar to those seen on attenuated phase-shift masks.

2.3.4 Diffractive Losses

Diffraction from the edges of the absorber layer can be seen in the field amplitude plots (figure 2.16). To gauge the magnitude of the diffractive losses, images from masks with 30 layer-pair coatings and 40 layer-pair coatings were compared. Since the difference in reflectivity for the two cases is 3%, diffractive losses could render the bottom layers irrelevant, resulting in little difference in the reflected images between 30-layer-pair and 40-layer-pair masks.

Calculated images show a slight increase of about 5% in the peak image intensity for the 40 layer-pair mask compared to the 30 layer-pair one. This shows that the bottom layers still contribute significantly to the reflected image, and that diffractive loss is not the dominant loss mechanism for mask linewidths of 0.4 μm or greater at 13.5 nm. Diffractive losses were found to be not as high as from chrome edges on an optical mask. This is probably because the lossy absorber material (germanium) does not produce high edge currents which re–radiate isotropically.

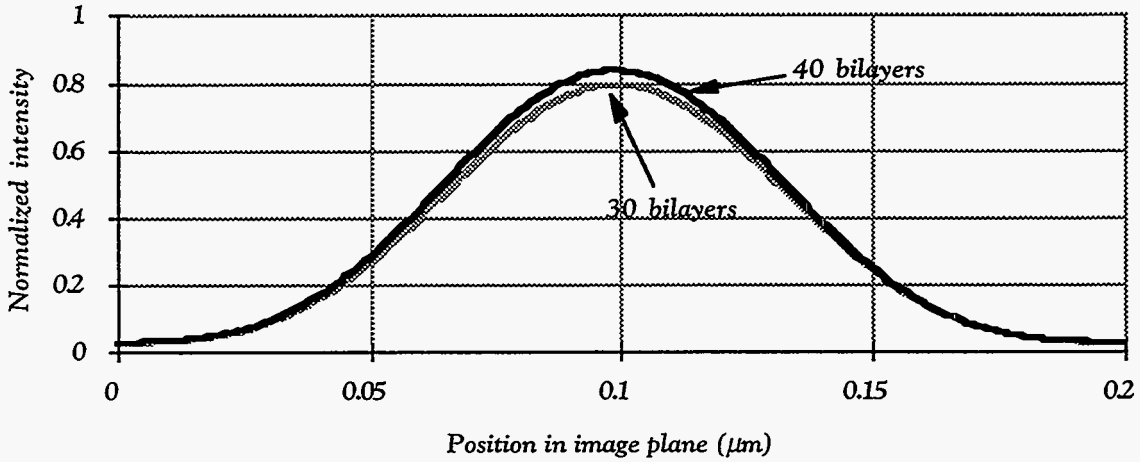

Figure 2.15. Aerial image intensity for Ge absorber mask with 30 bilayers and 40 bilayers. The higher reflectivity of the 40 bilayer coating results in higher peak image intensity.

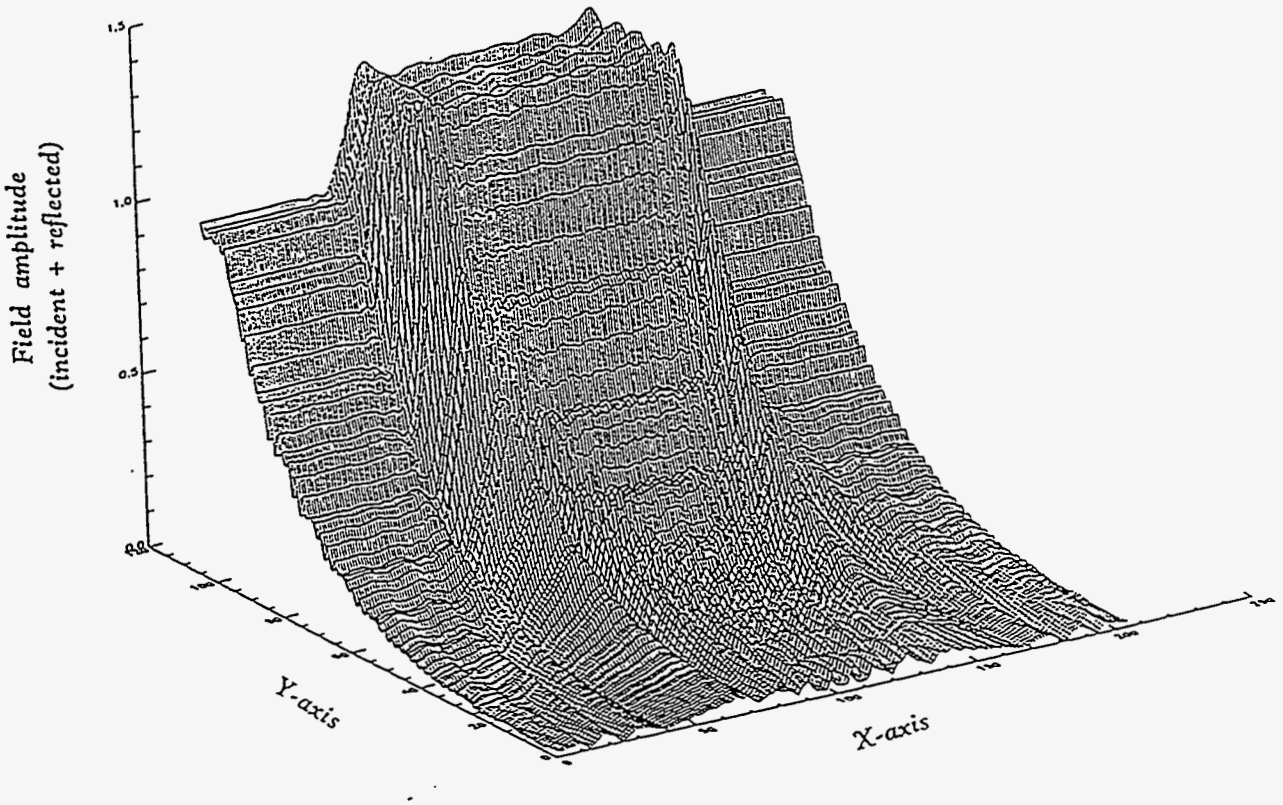

Figure 2.16. The incident and reflected field amplitude in the simulation domain for a Ge absorber mask with 40 bilayers of Mo/Si. The y-axis corresponds to the vertical direction on the mask; x-axis corresponds to the horizontal. The field amplitude decreases with distance traveled into the multilayer coating. The clear area of the mask corresponds to the region of higher field amplitude at the center.

2.3.5 Summary of comparison

In this section, electromagnetic simulations were used to compare the imaging characteristics of absorber layer masks and etched masks. The results show that aerial images from absorber masks are less sensitive to variations in incidence angles and pattern profiles. The higher sensitivity of etched masks to these variations can be explained in part by the thickness of the patterned multilayer stack.

In an absorber mask, the patterning layer is the absorber layer that is between 60 nm and 100 nm thick. In an etched mask, the patterning layer is the multilayer coating itself. At 13 to 14 nm wavelengths, the coatings typically consist of 40 layer pairs of 7 nm d-spacing, hence are approximately 280 nm thick.

The thicker patterning layers on etched masks result in more shadowing at off-normal incidence and larger linewidth variations at a given profile tilt angle. This translates to larger variations in peak image intensity for etched masks. If the absorber layer thickness is increased on an absorber mask, the peak image intensity would also be more sensitive to variations in incidence angles and pattern profiles.

Absorber overlayer masks could be made with a range of absorber materials, including gold, germanium and carbon. The absorber layer only needs to be on the order of 100 nm thick to be effective. With near-normal incident illumination and a thin absorber layer, the absorber overlayer mask is insensitive to both variations in the incident angle and the absorber profile. Diffractive losses were observed through plots of field amplitude in the simulation domain, but were found to have little effect on the aerial image. Absorber overlayer masks also allows for the possibility of built-in attenuated phase shift masks with an appropriate absorber material and absorber thickness.

References

1. G.E. Sommargren, and R. Hostetler, "Point diffraction interferometry at soft x-ray wavelengths," *Soft X-ray Projection Lithography* (Monterey, CA, USA), *OSA Proceedings*, vol. 18, A.M. Hawryluk, and R.H. Stulen ed., pages 100-104 (Optical Society of America, Washington, D. C., USA, 1993).

2. *Semiconductor Technology Workshop, Working Group Reports*, 154 pages (Semiconductor Industry Association, San Jose, California, 1992).

3. K. Early, and W.H. Arnold, "Cost of ownership for SXPL," *Soft X-ray projection lithography* (Monterey, CA, USA), *OSA Proceedings*, vol. 18, A.M. Hawryluk, and R.H. Stulen ed., pages 14-22 (Optical Society of America, Washington, D. C., USA, 1993).

4. R.A. Lawes, "Future developments for optical mask technology," Microelectronic Engineering, **23**, pages 23-29 (1994).

5. J.N. Wiley, and J.A. Reynolds, "Device yield and reliability by specification of mask defects," Solid State Technology, (July), (1993).

6. G. Owen, R.F.W. Pease, N.I. Maluf, R.L. Hsieh, J. Ye, and C.N. Berglund, "A rational argument for the impracticability of 1x reticles," *12th Annual Symposium on Photomask Technology and Management* (Sunnyvale, CA, USA), *Proceedings of SPIE*, vol. 1809, pages 39-48 (SPIE, 1992).

7. A.T. White, "Evolution of photomask industry," *11th Annual Symposium on Photomask Technology and Management* (Santa Clara, CA, USA), *Proceedings of the SPIE*, vol. 1604, pages 2-23 (The International Society for Optical Engineering, 1991).

8. K.B. Nguyen, A.K. Wong, A.R. Neureuther, D.T. Attwood, and T.D. Nguyen, "Aerial images of EUV projection lithography masks with defects in reflective coatings: Electromagnetic simulation," *Soft X-ray Projection Lithography* (Monterey, CA, USA), *OSA Proceedings*, vol. 18, A.M. Hawryluk, and R.H. Stulen ed., pages 47-53 (Optical Society of America, Washington, D. C., USA, 1993).

9. K.B. Nguyen, A.K. Wong, A.R. Neureuther, and D.T. Attwood, "Effects of absorber topography and multilayer coating defects on reflective masks for soft X-ray/EUV projection lithography," *Electron-Beam, X-Ray, and Ion-Beam Submicrometer Lithographies for Manufacturing III* (San Jose, CA, USA), *Proceedings of the SPIE*, vol. 1924, D.O. Patterson ed., pages 418-34 (The International Society for Optical Engineering, Bellingham, WA, 1993).

10. A.M. Hawryluk, N.M. Ceglio, and D.P. Gaines, "Reflection mask technology for x-ray projection lithography," Journal of Vacuum Science and Technology B, 7(6), pages 1702-1704 (1989).

11. A.M. Hawryluk, and N.M. Ceglio, "Wavelength considerations in soft x-ray projection lithography," Applied Optics, 32(34), pages 7062-7067 (1993).

12. D.L. Windt, W.K. Waskiewicz, J. Griffith, and J.E. Bjorkholm, "Surface finish requirements for SXPL optics," *Soft X-ray Projection Lithography* (Monterey, CA), *OSA Proceedings*, pages 32-34 (Optical Society of America, Washington, D. C., 1993).

13. Micro Lithography Inc., product literatures, (Sunnyvale, CA 94089)

14. D.M. Tennant, J.E. Bjorkholm, R.M. D'Souza, L. Eichner, R.R. Freeman, J.Z. Pastalan, L.H. Szeto, O.R. Wood II, T.E. Jewell, W.M. Mansfield, W.K. Waskiewicz, D.L. White, D.L. Windt, and A.A. MacDowell, "Reflective mask technologies and imaging results in soft x-ray projection lithography," Journal of Vacuum Science and Technology B, 9(6), pages 3176-3183 (1991).

15. D.M. Tennant, J.E. Bjorkholm, L. Eichner, R.R. Freeman, T.E. Jewell, A.A. MacDowell, J.Z. Pastalan, L.H. Szeto, W.K. Waskiewicz, D.L. White, D.L. Windt, and O.R. Wood II, "Comparison of reflective mask technologies for soft x-ray projection lithography," *BACUS Symposium on Photomask Technology , SPIE Proceedings*, vol. 1604, pages 91-104 (The International Society of Optical Engineering (SPIE), Bellingham, WA, 1991).

16. A.M. Hawryluk, N.M. Ceglio, D.W. Phillion, D.P. Gaines, R. Browning, R.F. Pease, D. Stewart, and N. Economou, "Reflection mask technology for soft x-ray

projection lithography," *Soft x-ray projection lithography* (Monterey, CA), vol. 12, J. Bokor ed., pages 45-50 (Optical Society of America, 1991).

17. H. Kinoshita, K. Kurihara, T. Mizota, T. Haga, Y. Torii, H. Takenaka, and Y. Ishii, "Soft x-ray reduction lithography using a reflection mask," *Soft x-ray projection lithography* (Monterey, CA), *OSA Proceedings*, vol. 12, J. Bokor ed., pages 11-15 (Optical Society of America, Washinton, D. C., 1991).

18. D.M. Tennant, L.A. Fetter, L.R. Harriott, A.A. MacDowell, P.P. Mulgrew, W.K. Waskiewicz, D.L. Windt, and O.R. Wood II, "Defect repair for soft x-ray projection lithography masks," Journal of Vacuum Science and Technology B, **10**(6), pages 3134-3140 (1992).

19. A.M. Hawryluk, and D. Stewart, "Repair of opaque defects on reflection masks for soft x-ray projection lithography," Journal of Vacuum Science and Technology B, **10**(6), pages 3182-3185 (1992).

20. K.B. Nguyen, E.M. Gullikson, and J.H. Underwood, "Top layer oxidation in Mo/Si multilayer x-ray mirror," *Materials Aspects of X-ray Lithography* (San Francisco, CA, USA), *Materials Research Society Symposium Proceedings*, vol. 306, G.K. Celler, and J.R. Maldonado ed., pages 135-144 (Materials Research Society, Pittsburg, PA, USA, 1993).

21. J.K. Gamelin, *Simulation of Topography Scattering for Optical Lithography with the Connection Machine*, Master's Thesis, University of California, Berkeley (1989).

22. R. Guerrieri, K.H. Tadros, J. Gamelin, and A.R. Neureuther, "Massively parallel algorithms for scattering in optical lithography," IEEE Transactions on CAD, **10**(9), pages 1091-1100 (1991).

23. A.K. Wong, R. Guerreri, and A.R. Neureuther, "Massively parallel electromagnetic simulation for photolithographic applications," IEEE Transactions on CAD, , (to be published).

24. A.K. Wong, *Two-dimensional electromagnetic simulation of topography scattering and diffraction for optical lithography*, Master Thesis, University of California, Berkeley (1992).

25. H.H. Hopkins, "On the diffraction theory of optical images," Proceedings of the Royal Society, London, Series A, **217**, pages 408-432 (1953).

26. J.H. Underwood, E.M. Gullikson, and K. Nguyen, "Tarnishing of Mo/Si multilayer x-ray mirrors," Applied Optics, **32**(34), pages 6985-6990 (1993).

Chapter 3

Oxidation of Mo/Si Multilayer Mirrors

3.1 Introduction

Multilayer coatings with high normal-incidence reflectivity are critical components for EUV lithography [1]. In an EUVL lithographic tool, Mo/Si multilayer coatings with reflection peaks near 130 Å would be used on all reflective surfaces - condensers, reflective masks, and optics. As a result, the power delivered to the wafer and wafer throughput are proportional to R^N, where R is the reflectivity of each mirror and N is the number of reflecting surfaces in the system.

Theoretically, the peak reflectivity from a Mo/Si multilayer coating could be as high as 72% around 13 nm assuming perfectly sharp interfaces between Mo and Si. However, interfacial roughness and interlayer mixing reduce the achievable peak reflectivity. Currently, normal incidence reflectivity of higher than 60% is routinely achieved and a reflectivity of 65% has been reported [1-3].

To reduce the cost-of-ownership of an EUVL printer, the multilayer coatings in the system must maintain their high reflectivities over a reasonably long period of use. Underwood et al. [4] have reported significant reduction of peak reflectivities for Mo/Si multilayers with molybdenum as the top layer ("Mo-top" multilayers) when they were stored in ambient air. This was the result of oxidation of the top Mo layer to MoO_3 and MoO_2, as shown by electron spectroscopy for chemical analysis (ESCA). Some techniques were tried to recover the reflectivity of the oxidized multilayer. Initial results also showed that Mo/Si coatings with Si as the top layer ("Si-top" multilayers) maintained their high reflectivities over time.

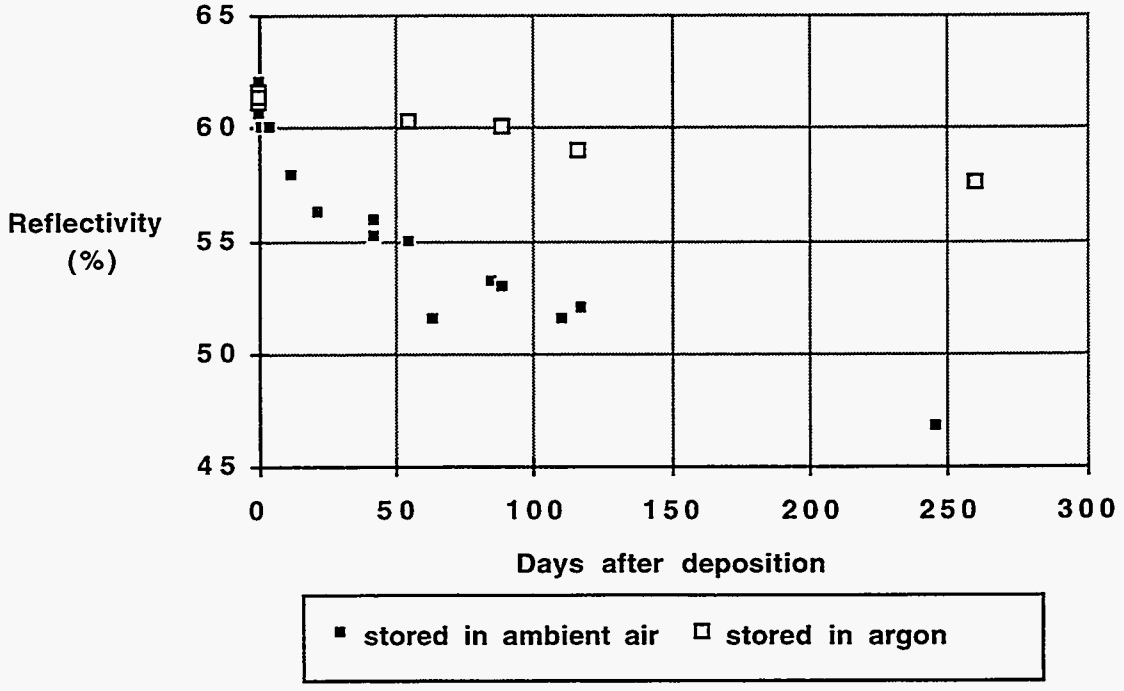

Figure 1. Reduction in peak reflectivity over time for a Mo-top Mo/Si multilayer x-ray mirror stored in air is greater than that stored in argon. Reflectivity of the mirror stored in air decreased by 10% after 100 days.

The chapter contains additional measurements of reflectivity reduction over time for Mo-top multilayers, and descriptions of another reflectivity recovery technique. Results from a detailed study of the reflection characteristics of Si-top Mo/Si multilayers are also reported.

3.2 Experimental Set–up

All multilayer coatings in this study were deposited by planar magnetron sputtering in 2.5 mtorr of argon. The base pressure was typically 10^{-6} torr. The substrates were 3" silicon wafers and General Optics optical flats. Silicon was RF sputtered at 13.56 Mhz at about 0.6 kW, while Mo was DC-sputtered at 250 W. The Si and Mo targets were at the bottom of the chamber, while the substrates were rotated at precise speed over them to control the deposition rate. The substrates were also rotated at approximately 300 rpm about their centers (planetary rotation) to ensure uniform deposition over their entire surfaces. Unless otherwise stated, all coatings consisted of 40 layer pairs of 70 Å-period Mo/Si with reflection peaks between 135 Å and 140 Å.

Normal incidence reflectivities were measured using a reflectometer with a laser-produced-plasma source [5]. The spectral resolution of the reflectometer was set by a high throughput spherical grating monochromator with moderate resolving power ($\lambda/\Delta\lambda$ varies from 100 to 500). All reflectivity measurements was performed at 5° off-normal incidence in wavelength steps of 0.2 Å.

3.3 Determination of Oxidation

Peak reflectivities of two Mo-top multilayer coatings deposited on optical flats in the same deposition run were monitored for over 300 days. The coating stored in air showed sharp reduction in its reflectivity over the first few days and a slower but continuing reduction of its peak reflectivity over the entire period of observation. The coating stored in argon, on the other hand, shows a much smaller and more gradual decrease in its reflectivity (Figure 3.1). This behavior provided indications that the reductions in coating reflectivity were the result of a surface chemical effect.

In order to determine the nature of the surface chemical reaction, we (Underwood et al. [4]) used ESCA to investigate the surface chemical composition of a coating stored in air. The sample was a Mo-top Mo/Si coating with 20 bilayers, d-spacing of 87 Å and $\Gamma \approx$ 0.4. It had been stored in air for over 300 days. A Mg Kα x-ray tube at 1253 eV was the ESCA excitation source. We also used ion beam etching together with ESCA to investigate how the chemical composition varies with depth into the sample. Each

profiling cycle consists of an ESCA scan followed by an etching cycle to expose the lower layers. Each etching cycle is 30 seconds of ion beam sputtering with 1 mA/mm^2 of 2 keV argon ions. The results for 62 etch-and-scan cycles are shown in figure 3.2. The first cycle, corresponding to a scan of the surface layer, is at the bottom of the plots in figure 3.2 and the last cycle is at the top.

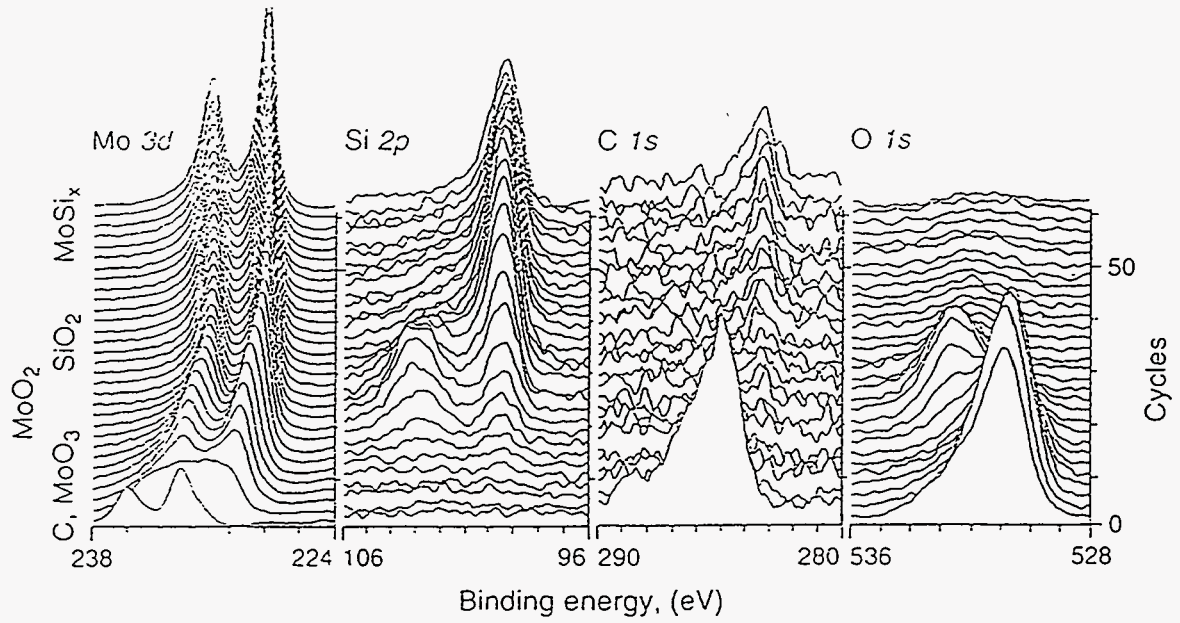

Figure 3.2. ESCA results from a Mo/Si coating with Mo as the top layer shows Mo peak at 232.65 eV on the surface, corresponding to MoO_3. SiO_2 is detected at the Mo/Si boundary as shown by the O 1s peak at 534 eV and the Si 2p peak at 108 eV. The SiO_2 layer also acts as an effective barrier to oxygen diffusion, for no more oxygen can be detected below the silicon dioxide layer.

The electron energy scan of the surface shows a peak in binding energy at 233 eV, corresponding to MoO_3 [6]. The scan also reveals the presence of carbon contamination, as can be seen from the strong C 1s peak at 285 eV. Over the next ten etch-and-scan cycles, the Mo peak shifts toward lower energies, possibly due to the presence of MoO_2. As etching continues, the peak shifts toward 227 eV corresponding to elemental Mo or molybdenum silicide. These results from ESCA show that oxidation of elemental Mo of the top layer to MoO_3 and MoO_2 was the reaction responsible for the reductions in reflectivity of Mo-top multilayers. Calculations show that partial oxidation of the top Mo layer is enough to account for the observed reductions in reflectivity [4].

Another important feature in the ESCA results is the presence of a thin layer of SiO_2, as can be seen from the Si 2p feature at a binding energy of 108 eV and the O 1s feature at a binding energy of 534 eV. Below the SiO_2 layer, no oxygen is detected, demonstrating the well-known fact that SiO_2 serves as an effective barrier to oxygen diffusion.

3.4 Removal of Oxides

For EUVL, the observed 10% reduction in reflectivity would result in a intolerable reduction in wafer throughput. A reduction of reflectivity from 62% to 50% in a system with seven reflective surfaces, for example, would reduce wafer throughput by a factor of four. Clearly, techniques to preserve or recover the high peak reflectivity are needed.

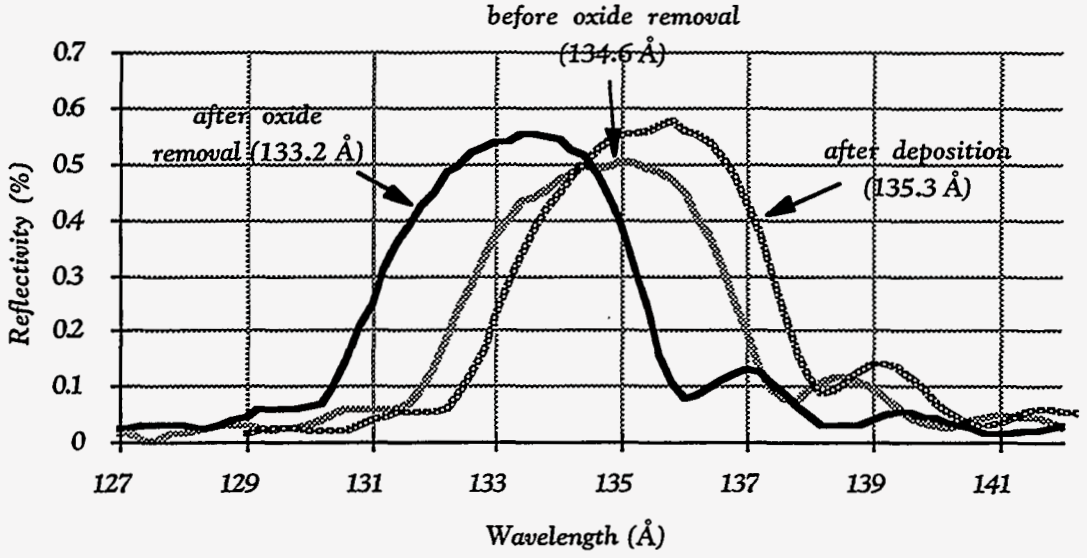

Figure 3.3. High peak reflectivity can be partially restored by removing the oxide layer. Oxide removal increased peak reflectivity of the Mo-top Mo/Si coating from 49% to 55.5%, nearly as high as its reflectivity immediately after deposition (57%).

One approach to recovering the reflectivity is to remove the oxidized molybdenum layer. Some initial cleaning techniques have been attempted by Underwood et al., including rinsing in hot and cold water, in acetone, in alcohol, and in H_2O_2 [4]. The results from these initial experiments suggests that a two-step cleaning process might be more effective in removing the oxide layer. The sample is first immersed in H_2O_2 for 15 minutes to completely oxidize the molybdenum layer. It is then put into boiling water for another 15 minutes to remove the molybdenum oxides.

With this fairly crude technique, we were able to restore the peak reflectivity of a oxidized coating to nearly its reflectivity immediately after deposition. As shown in figure 33, the peak reflectivity of this Mo-top Mo/Si coating was 57% immediately after deposition. After having been stored for 195 days in air, the peak reflectivity was reduced to 50%. After oxide removal with the two-step cleaning process, peak reflectivity is 55.2%.

A prominent feature in figure 3.3 is the 1.5 Å shift in the reflection peak after oxide removal. Since the measurements of reflectivity before and after oxide removal were made within an hour of each other at the same monochromator setting, the shift is not likely to be the result of wavelength calibration errors in the monochromator. It could instead be due to the heating cycle in the oxide removal process, as seems possible from the data for a low temperature heating experiment to be presented in a following section.

3.5 Mo/Si Multilayers with Si as the top layer

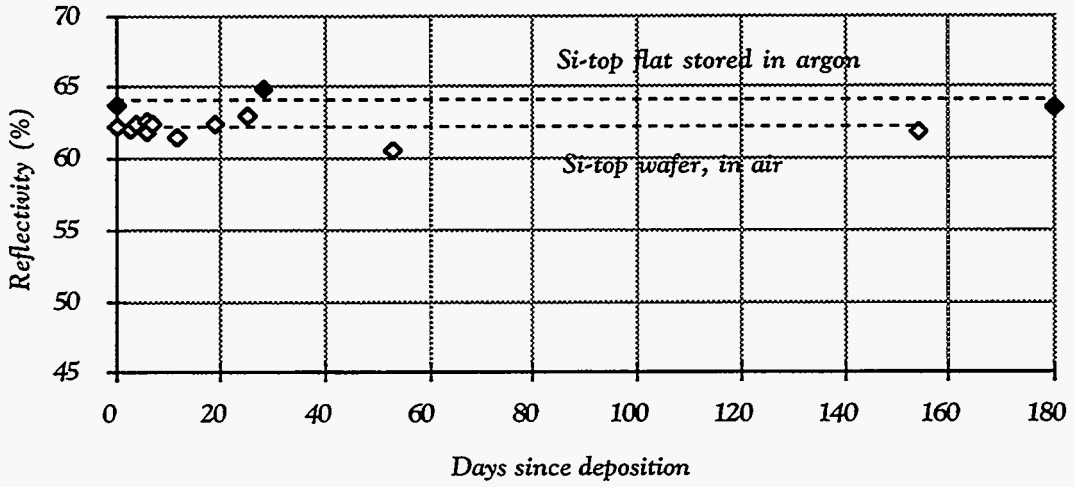

Figure 3.4. Peak reflectivity of Mo/Si mirror with Si as the top layer is nearly constant over 180 days, both for samples stored in air and samples stored in argon. The sample stored in argon was deposited on an optical flat with low rms roughness, and the sample stored in air was deposited on Si wafer substrate. As a result, the reflectivity of the in-argon sample is slightly higher than that of the in-air sample. The dashed lines show the average reflectivity over the measurement period.

It is well-known that when a Si film is exposed to air, a 10 Å to 20 Å native oxide layer quickly forms above the Si film and becomes an effective diffusion barrier against further oxidation. This was observed in the ESCA results in figure 3.2. In light of this fact, Mo/Si reflective coatings with Si as the top layer were deposited and their reflectivities monitored. Figure 3.4 shows that reflectivity of a Si-top Mo/Si coating is roughly constant over the 150 days that it was stored in air.

A careful tracking of reflectivity actually shows reflectivity increasing slightly during the first few days following deposition. Figure 5 shows reflectivity for all samples used in this study. The specifications for all samples are shown in table 1. Reflectivities of all but one of the samples increased between the 1st and 5th days after deposition. Reflectivity measurements were performed on samples with four different top Si layer thicknesses - 20 Å, 38 Å, 50 Å, and 100 Å. As a result, the increases in reflectivity are unlikely to be due to phase matching due to expansions of the top Si layer during the native oxide formation process. The physical basis for this effect is still unclear at this writing and is a problem worth investigating.

Table 1. Sample Description - Mo/Si multilayer coatings, n = 40, d = 70 Å, $\Gamma \sim 0.45$

Sample	Top Layer
93-094	38 Å Si-top
93-095a	38 Å Si-top
93-095b	20 Å Si-top
93-096a	38 Å Si-top
93-096b	100 Å Si-top
93-097a	38 Å Si-top
93-097b	50 Å Si-top

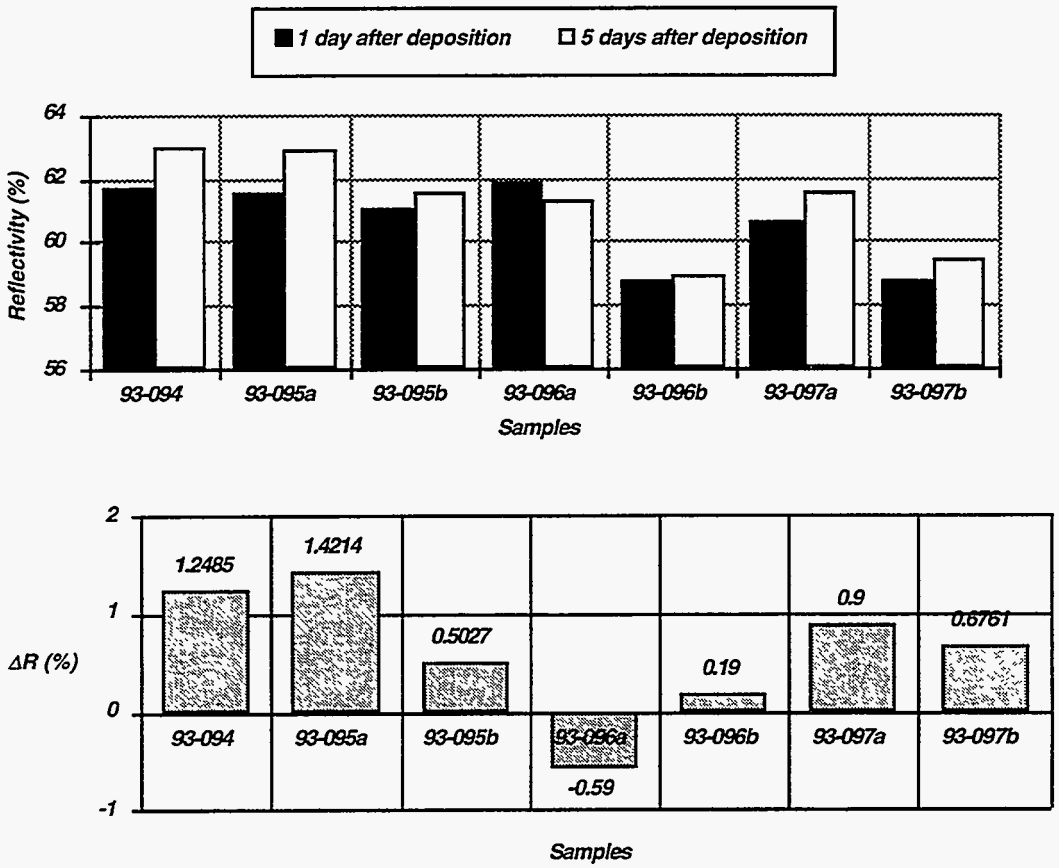

Figure 3.5. Peak reflectivity of Si-top Mo/Si multilayer mirror increased slightly during the few days immediately following deposition for 6 out of 7 samples observed in this study. (a) Reflectivity after 1 and 5 days after deposition; (b) reflectivity changes between 1 and 5 days after deposition.

3.5.1 Varying top Si layer thickness

Since some expansions in the thickness of the top layer occur due to native oxide formation, it is not obvious how thick the top Si layer should be to maximize peak reflectivity. Since the phase matching for reflections from the top Si layer with the rest of the stack is lost due to film expansion during native oxide formation, it is possible that a thinner Si top layer would result in the optimum peak reflectivity. Coatings with different Si top-layer thicknesses were deposited to study the effect the Si top-layer on reflectivity.

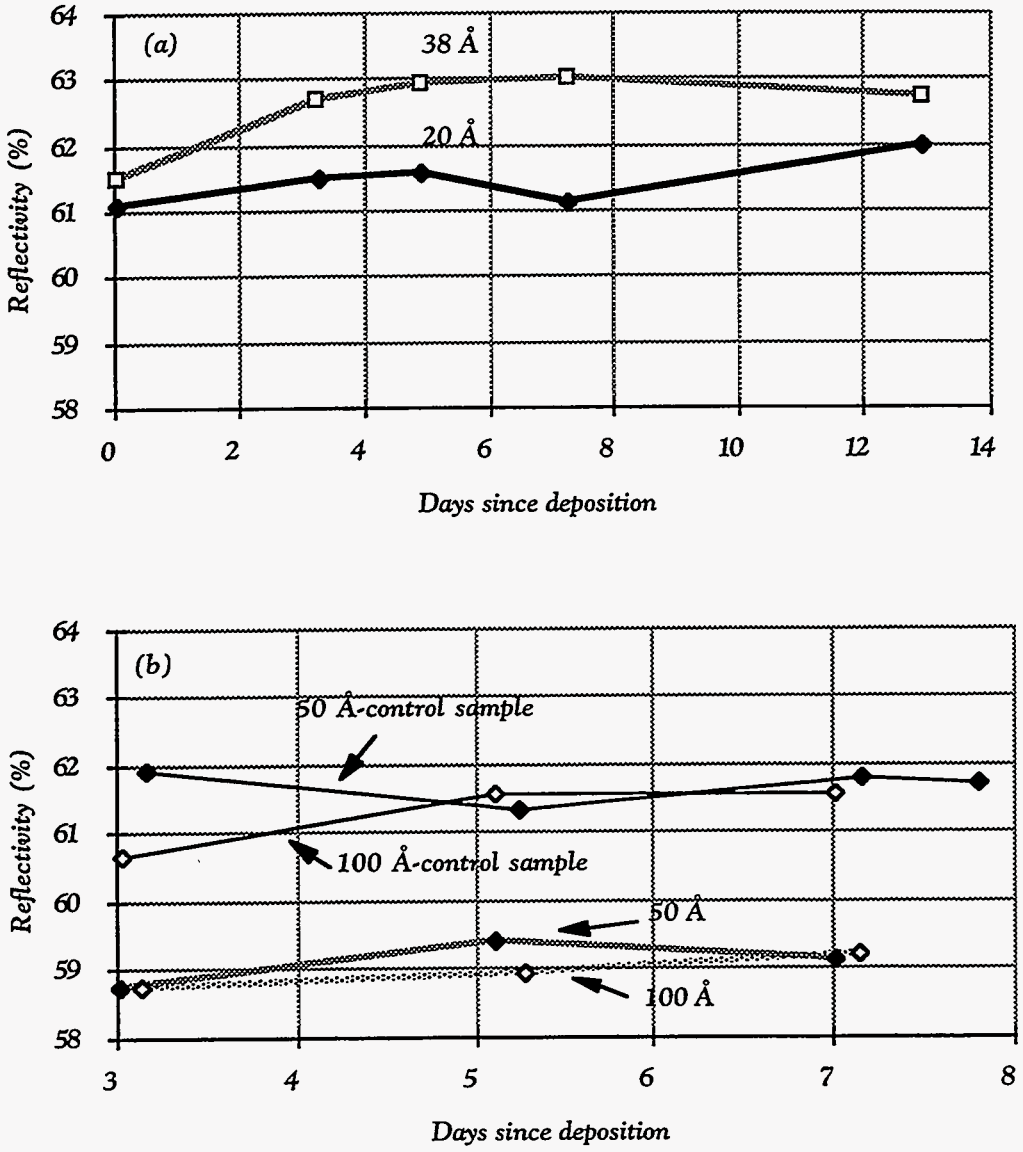

Figure 3.6. Reflectivity for 40 bilayers Si-top Mo/Si multilayer coatings with different top Si layer thickness. The highest reflectivity was achieved with the top Si layer at 38 Å, the same thickness as the rest of the stack (6a). With top Si layer thickness of 20 Å, the peak reflectivity is lowered by roughly 1%. Samples of 38 Å and 20 Å top layer thickness were made in the same deposition run. Results for samples with 50 Å and 100 Å top layer thickness are also shown (6b).

Coatings with initial top Si layer thickness of 20 Å, 38 Å (same as the rest of the stack), 50 Å and 10 Å were deposited. The Si-layer thicknesses were controlled by varying the dwell time of the substrates over the targets. The samples with 20 Å and 38 Å top Si layer thickness were made in the same deposition run to eliminate differences in reflectivity due to run-to-run variations. For each sample with top Si-layer thickness of

50 Å or 100 Å, a control coating with top Si layer thickness of 38 Å, the same as the rest of the stack, was also deposited to allow for estimation of reflectivity difference due to run-to-run variations.

As seen in Figure 3.6(a), peak reflectivity is highest with the top Si-layer of 38 Å, i.e. the same thickness as the rest of the stack. The reflectivity for the coating with 20 Å top Si layer was 61.5%. The reflectivities of coatings with 50 Å and 100 Å top Si-layer thicknesses, shown in figure 3.6(b), were ~59%, or 2% lower than that for the control 38 Å Si-top coatings deposited in the same run.

3.5.2 Effect of moderate heating on reflectivity

For EUVL, the reflecting surfaces of the system, especially the condensers and masks, would experience moderately high incident radiation intensity. Due to absorption, this could translate into slight heating of the coatings. To observe any effect such slight heating might have on the native oxide layer and the multilayer coatings structure, 3 Si-top Mo/Si multilayer mirrors were heated on a hot plate at 36° C continuously for two weeks and their reflectivities measured over this period. The temperature was chosen to illustrate that the heating temperature was quite moderate.

Each sample was observed, unheated, for a few days following deposition. A piece of the coating was then broken off and placed on the hot plate at 36° C. The reflectivity of both the heated and unheated pieces were measured over the next days to observe any differences between them.

The results are similar for both samples, showing a 1.5 Å shift in the reflection peak 1-2 days after heating and no further peak shifts for the following week of continuous heating. This result might be consistent with those reported by Rosen et al. which shows a two-stage process in the interlayer silicide growth, with the strong initial "surge" possibly due to either relaxation in composition of the Mo-rich silicide layer to a more stable silicide or relaxation of residual stresses in the deposited film [7]. Similar shifts in reflection peaks in W/Si and W/C multilayers subjected to slight heating (55°C to 74°C) by wiggler irradiation have been reported by Kortright et al. [8]. A more detailed study of the behavior of multilayer coatings under moderate heating is being conducted at the Center for X-ray Optics to better the understand this effect.

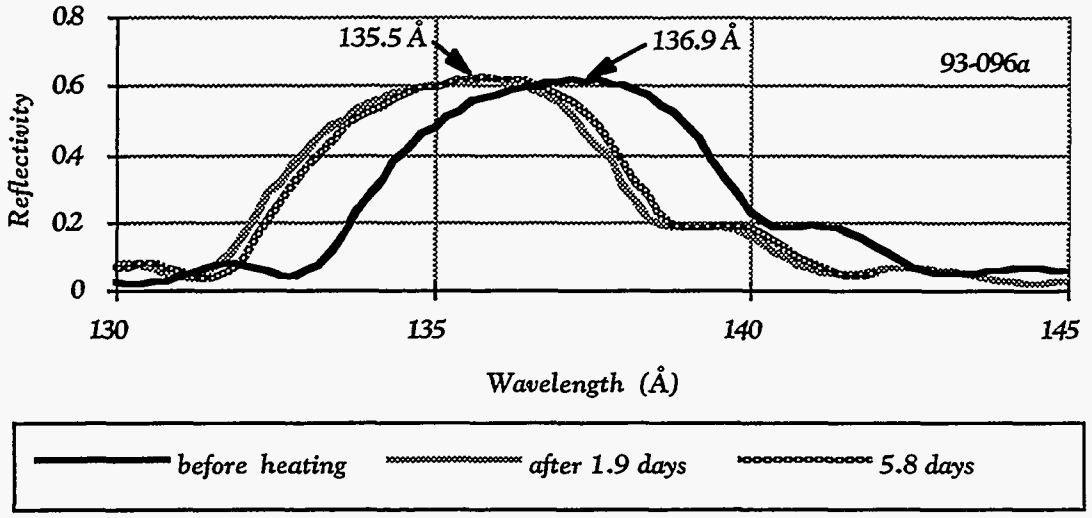

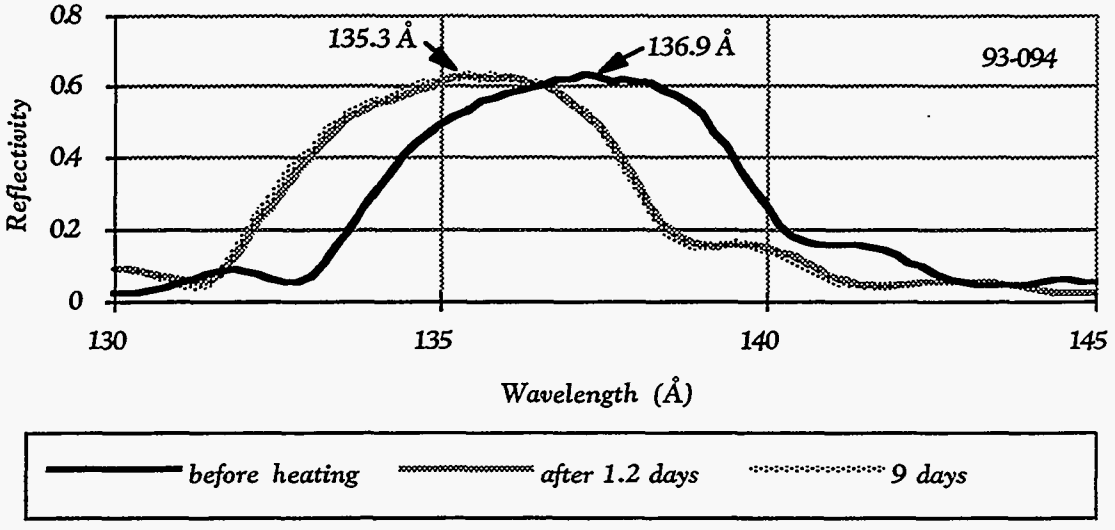

Figure 7. Continuous heating at 36° C over two weeks does not affect the reflectivity of Si-top multilayer mirrors. However, shifts in the reflection peaks by ~1.5 Å were observed. The dark solid lines show reflectivity of the samples before heating, the dashed lines the reflectivity after 1 day of heating and the light solid lines the reflectivity after 5 to 9 days of heating.

3.6 Conclusion

Mo/Si multilayer mirrors with Mo as the top layer suffer significant reductions in peak reflectivity over time when stored in ambient air. The cause for this reduction was determined to be oxidation of elemental Mo in the top layer into MoO_3 and MoO_2. The high peak reflectivity can be preserved simply by depositing Si as the top layer. Experiments showed the thickness of the top Si layer should equal that of Si layers in the rest of stack for maximum reflectivity. Reflectivity can be also be partially restored by removing the Mo oxide layer by wet etching.

Si-top Mo/Si coatings showed increases in reflectivity of 1% over the first few days following deposition. Slight continuous heating at 36°C produced 1.5 Å wavelength shifts in the reflection peaks of the coatings. The physical basis of these effects are not well-understood at this time and deserve further studies.

References

1. D.G. Stearns, R.S. Rosen, and S.P. Vernon, "Multilayer mirror technology for soft x-ray ojection lithography," Applied Optics, 32(34), pages 6952-6960 (1993).

2. J.B. Kortright, D.G. Stearns, and D.L. Windt, ed., *Physics of X-ray Multilayer Structures (Jackson Hole, Wyoming, USA, March 2-5, 1992)*, OSA Technical Digest Series, vol. 7, 186 pages (Optical Society of America, Washington, D. C., 1992).

3. J. Kortright, D. Stearns, and E. Ziegler, ed., *Physics of X-ray Multilayer Structures (Jackson Hole, Wyoming, USA, March 14-17, 1994)*, OSA Technical Digest Series, vol. 6, 188 pages (Optical Society of America, Washington, D. C., 1994).

4. J.H. Underwood, E.M. Gullikson, and K. Nguyen, "Tarnishing of Mo/Si multilayer x-ray mirrors," Applied Optics, 32(34), pages 6985-6990 (1993).

5. E.M. Gullikson, J.H. Underwood, P.C. Batson, and V. Nikitin, "A soft x-ray/EUV reflectometer based on a laser-produced plasma source," Journal of X-ray Science and Technology, 3, pages 283-299 (1992).

6. C.D. Wagner, W.M. Riggs, L.E. Davis, J.F. Moulder, and G.E. Mullenberg, *Handbood of X-ray Photoelectron Spectroscopy*, (Perkin-Elmer Corporation, MN, USA, 1979).

7. R.S. Rosen, D.G. Stearns, M.A. Viliardos, M.E. Kassner, S.P. Vernon, and Y. Cheng, "Silicide layer growth rates in Mo/Si multilayers," Applied Optics, 32(34), pages 6975-6980 (1993).

8. J.B. Kortright, S.T. Joksch, and E. Ziegler, "Stability of tungsten/carbon and tungsten/silicon multilayer mirrors under thermal annealing and x-ray radiation exposure," Journal of Applied Physics, 69(1), pages 168 (1991).

Chapter 4

Effect of Substrate Defects on Aerial Images — Electromagnetic Simulations

4.1. Introduction

Masks for EUV lithography are made by depositing patterned absorber layers above multilayer reflective coatings. The periods of the coatings are optimized to provide high reflectivity at the operating wavelength of the lithographic printer. Such masks have been successfully fabricated and imaged [1-4].

For semiconductor manufacturing, the masks must be defect-free. In other words, there can be no defect on the mask that would cause variations in the resist image greater than a certain limit. In lithography, this limit is typically 10-15% of the minimum feature size [5-8]. In order to determine the maximum allowable defect size on a mask, printability studies are conducted, and many such studies have been performed for optical/DUV lithography [5-21].

In an EUVL mask, mask defects can occur either on the substrate below the multilayer reflective coating, in the coating itself, or on the absorber layer. Preliminary studies

have shown that defects in the *absorber layer* can be repaired with ion-assisted processes similar to those used for optical/DUV mask repairs [22, 23].

Defects in the mask's *multilayer reflective coating* present a more serious problem for there is no multilayer coating repair technique presently available. Coating defects could arise from contaminants in the deposition chamber and from other sources of environmental contaminants in the cleanroom. While such defects on an optic would result in a distributed degradation of system performance, defects on a mask might cause variations in the printed patterns and affecting the achievable yield of the fabricated devices.

In this chapter, results are reported from a detailed simulation study of the effect of coating defects on aerial images. Aerial images from masks with coating defects were calculated for different defect positions, defect sizes, and defect coverage profiles. This chapter contains the results and discussions of the various cases studied, together with descriptions of the mask geometries and the techniques used.

4.2. Mask Geometry and Simulation Techniques

4.2.1 Simulated Mask Geometry

The masks simulated in this study were absorber overlayer masks. The reflective coatings consisted of 40 layer pairs of Mo/Si with 7 nm-period and Γ, the ratio of Mo layer thickness to layer pair thickness, of 0.5. The absorber layers were 60 nm thick of germanium with 10° profile tilts to simulate imperfections in the absorber deposition and patterning process. However, electromagnetic simulation results reported in chapter 2 already showed that such imperfections have little effect on the image [24].

In order to understand the manner in which the multilayer coating process covers the defects, transmission electron microscopy (TEM) was used to study the profiles of programmed defect [5]. This work will be described in more detail in chapter 5. The TEM work was done in collaboration with Tai D. Nguyen, a graduate student in Materials Science at UC Berkeley/Center for X-ray Optics. Examples of observed propagation profiles for defects are shown in figure 4.1. Figure 4.1(a) is a cross-sectional TEM image of a Mo/Si coating over an *unprogrammed* defect of roughly 20 nm thick and 80 nm wide. Some lateral spreading of defect geometry occurred due to film deposition,

resulting in a top layer perturbation of ~ 100 nm wide. Figure 4.1(b), a TEM cross-sectional image of a Mo/Si coating deposited over a *programmed* 40 nm thick gold step, shows observable distortions in the multilayer structure due to the presence of the defect edge. Such distortions would result in lower reflectivity from the defective area. The darker appearance towards the bottom of both images is due to the wedge shape of the samples, which are slightly thicker at the bottom than at the top. This is an artifact of the ion-milling process used to thin down the samples for TEM observation.

To simulate profiles of defects covered by multilayer coatings in this study, I have used a model with two parameters empirically fitted to the observed coverage profile. The film deposition rate was assumed to be the same both on the substrate and on top of the defect. Deposition rate on the sidewall of the defect was assumed to be some fraction of the deposition rate on top of the defect.

Horizontal propagation of defect geometry at each subsequent layer is denoted as Δx, where

$$\Delta x = \frac{d}{2} f_{side} f_{damp}^{n} \qquad (1)$$

where $d/2$ is the thickness of each layer on the substrate and on top of the defect — 3.5 nm in this study. The parameter f_{side} is the ratio of deposition rate on the sidewalls over that on the substrate. The parameter f_{damp} is an artificial damping constant chosen to fit the simulated profile to the observed profile, and n is the number of deposited layer measured from the substrate. These parameters are illustrated in figure 4.2.

A reasonable fit to the observed profiles was obtained with f_{side} of 0.4 and f_{damp} of 0.8. Unless stated otherwise, these values were used for all cases in this study. This model, however, did not take into account possible step height reduction and smoothing around the edges of the defects due to multilayer coating deposition.

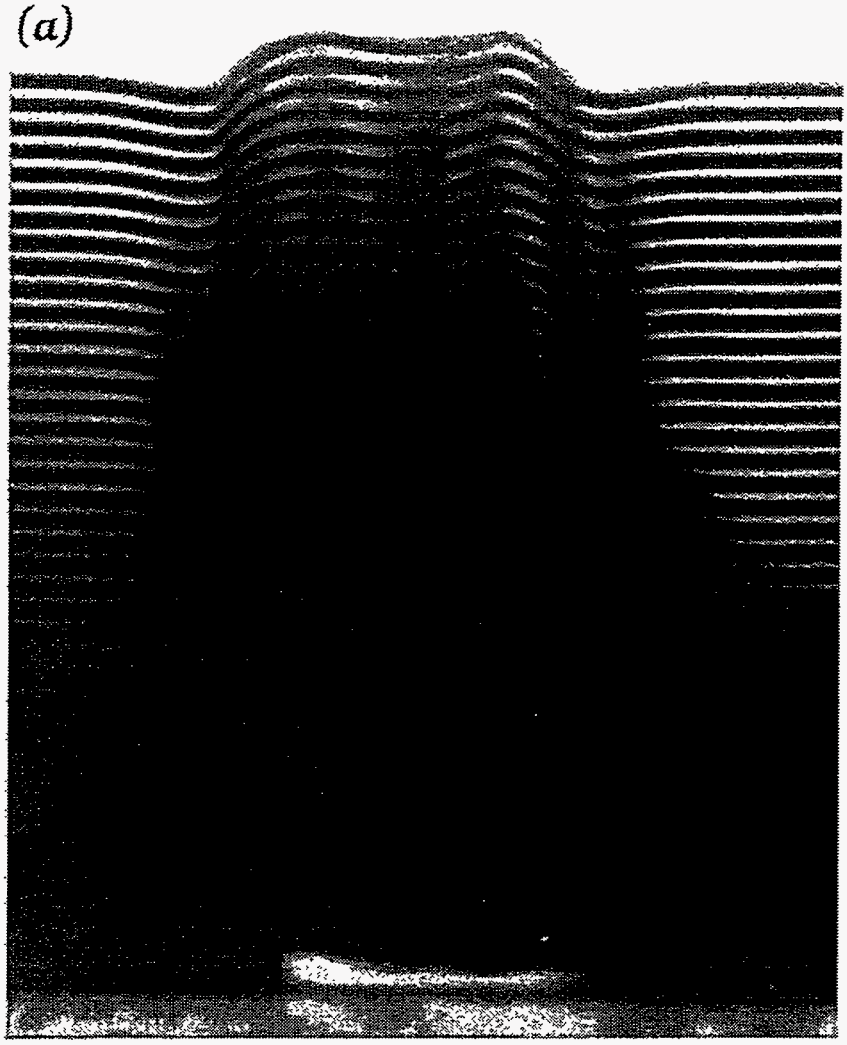

Figure 4.1. (a) TEM cross-sectional image of an unprogrammed defect covered by a 40-bilayer, 7-nm period Mo/Si coating. Defect is 20 nm high and 80 nm wide on the substrate. Lateral spreading of profile due to film coverage increase defect with to ~ 100 nm at the top of coating. (b) TEM cross-sectional image of 40-bilayer, 7-nm period Mo/Si deposited above a 40 nm thick gold step, showing distortions in multilayer structure.

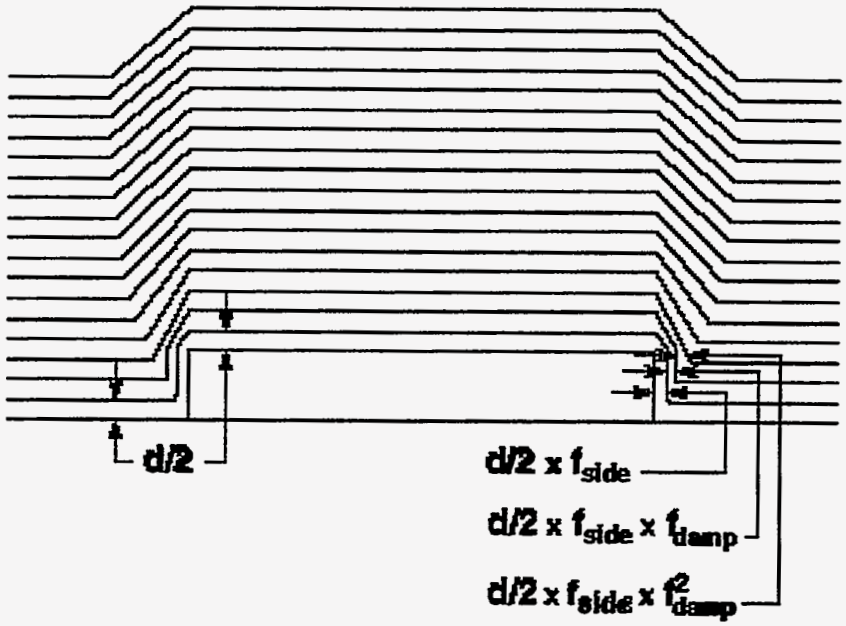

Figure 4.2. The model used to simulate defect coverage profile. The simulated defect profiles are fitted to observed defect profiles by adjusting f_{damp} and f_{side}.

The deposition could be more accurately simulated using SAMPLE, a program for Simulation and Modeling of Profiles in Lithography and Etching that was developed by the research groups of Professors W. G. Oldham and A. R. Neureuther at the University of California at Berkeley. An example of the coverage profile over a 10 x 30 nm line defect simulated with SAMPLE is shown in figure 4.3. The parameters of simulated profile can be adjust to produce an adequate fit to the observed TEM profiles. I have used the simple two-parameter model because it was sufficient for studies of relative effects. A more accurate profile simulation technique would be required if absolute magnitude of the effects were desired.

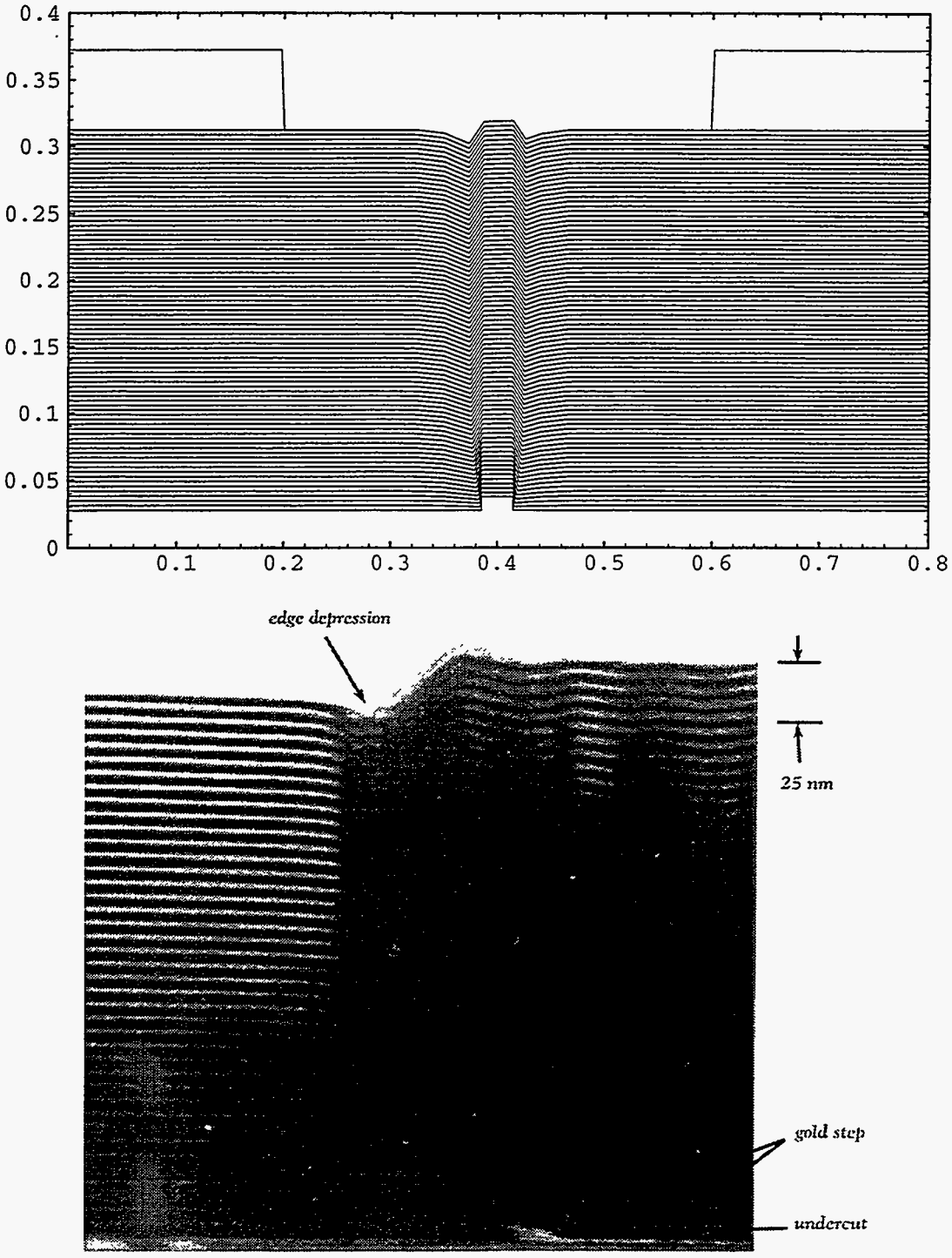

Figure 4.3. (a) An example of deposition profiles simulated by SAMPLE. The defect is a 10 nm high by 30 nm wide line. An interesting feature seen here is the slight depressions formed at the edges of the defect. Similar depressions were observed in TEM cross-sectional images of defects. (b) A TEM cross-sectional image of 40 bilayers of Mo/Si deposited over a 20 nm thick gold step, showing edge depression. (TEM taken by Tai D. Nguyen, UCB/LBL).

4.2.2 Aerial Image Simulation Process

As was described in chapter 2, aerial images of the reflective masks were calculated in a two-step process. First, the reflected field from the mask was calculated using TEMPEST, a two-dimensional time-domain finite-difference program for solving Maxwell equations [7, 8]. TEMPEST was used because it is capable of calculating the effect of topography on images. The mask structures were input to TEMPEST in terms of the refractive indices and thickness of the materials. Examples of input profiles are shown in figure 4.4.

The aerial images were synthesized from the reflected fields using Hopkins's technique [9], taking partially coherent illumination into account. Aberration-free 4:1 reduction imaging at 13.5 nm wavelength was simulated, with partial coherence factor σ of 0.5 and numerical aperture of 0.1 corresponding to nominally 0.1 μm resolution.

It is important to note that since this version of TEMPEST simulates only 2-dimensional structures and that periodic boundary conditions were imposed on the side boundaries of the simulation domain, the masks simulated here were repeating series of lines and spaces with repeating line defects on the substrate. Since real defects are most commonly isolated and particle-like in shapes, the effect of these simulated defects on aerial images are likely to be much more severe than would be encountered in real defects. Furthermore, defect printability studies for optical lithography have shown that defects are more likely to be printed when they occur in periodic patterns [5]. For these reasons, the results reported here are useful for comparing the relative imaging characteristic of the different types of defects, not for their absolute effect on the image.

4.3. Effect of Substrate Defects on Aerial Images

4.3.1. Comparison of Substrate Defects and Absorber Defects

The effects of substrate defects on images were first estimated by comparing their aerial images with those for absorber defects of the same size. Figure 4.4 shows the mask geometries and simulated aerial images for a mask with a 10 x 30 nm substrate line defect and a mask with an absorber defect of the same size. The aerial images for masks with no defect and 10 x 50 nm defect are also shown. Since a 4:1 imaging system with 0.1 μm

resolution is simulated here, the minimum feature size on the mask is 0.4 μm, and a 30 nm wide defect corresponds to less than 1/10 of the minimum feature size.

Figure 4.5 shows that peak image intensity was reduced by 17% in the presence of a 10 x 30 nm absorber defect line and by 60% in the presence of a substrate defect line of the same size.

Since the multilayer coating may suffer abrupt profile changes in the region around the substrate defect, as seen in figure 4.1(b), the multilayer structure would be distorted and its reflectivity reduced. To simulate the reduced reflectivity, a thin gold absorber layer was added over the defective region (figure 4.6(a)). A 10 nm gold absorber reduces coating reflectivity from 70% to approximately 30%. Figure 4.6(b) shows the aerial images from masks with a 10 x 30 nm substrate defect covered by gold absorber layer of different thicknesses. In all cases, the capped defects resulted in higher image intensity. A thicker cap resulted in less reflected light from the defective region, thus lessening the defect' s effect on the image. This suggests that phase effects play important roles in the large decreases in image intensity caused by the substrate defects.

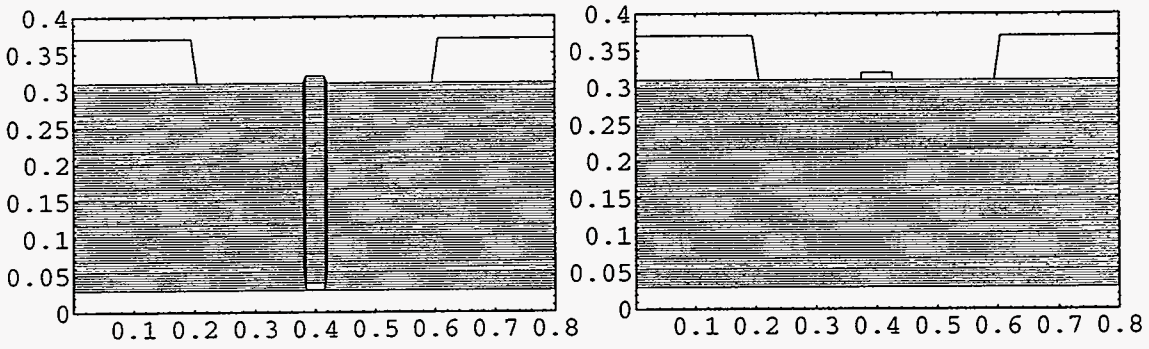

Figure 4.4. Simulated mask geometries for substrate defect and absorber defect. The simulated defect lines are 10 nm thick by 30 nm wide substrate defect and 10 nm x 50 nm absorber defect

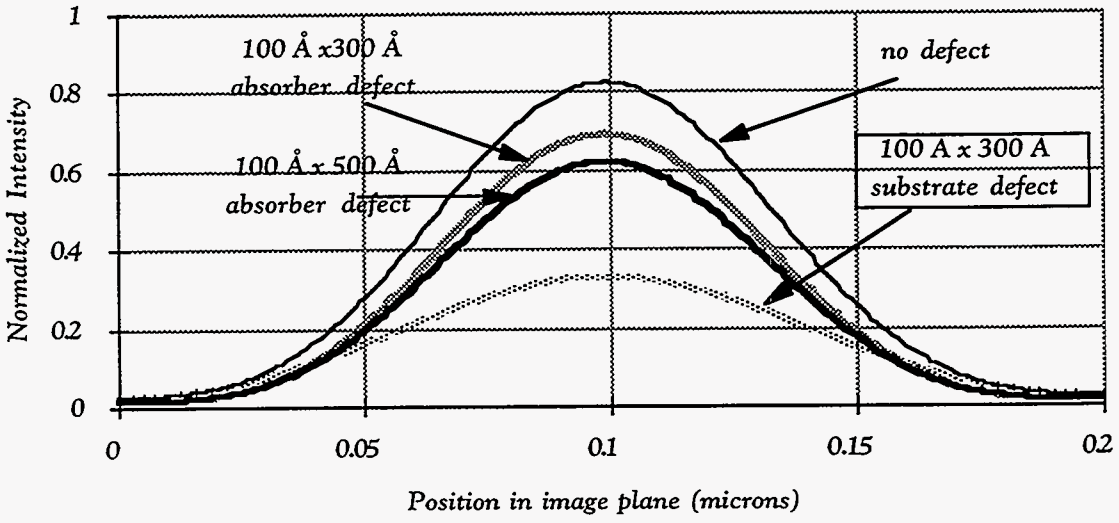

Figure 4.5. A 10 x 30 nm substrate defect reduces peak aerial image intensity by 60% compared to 17% for an absorber defect of the same size. A 10 x 50 nm absorber defect reduces image intensity by 25%.

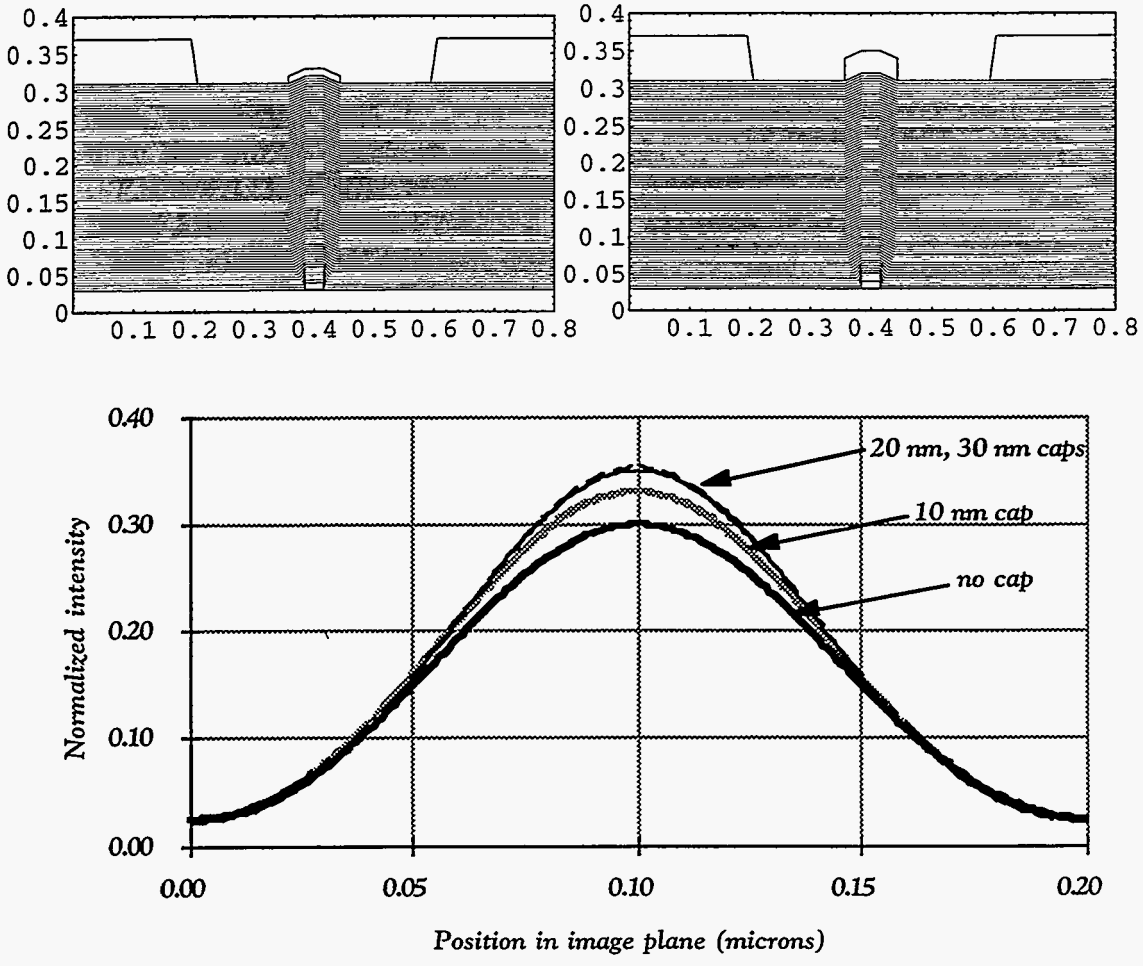

Figure 4.6. Simulated geometry and aerial images for capped defects. Input geometries for 10 nm cap and 30 nm cap are shown. Capping the defect reduces the reflected field from the defective area and lessens its effect on the image.

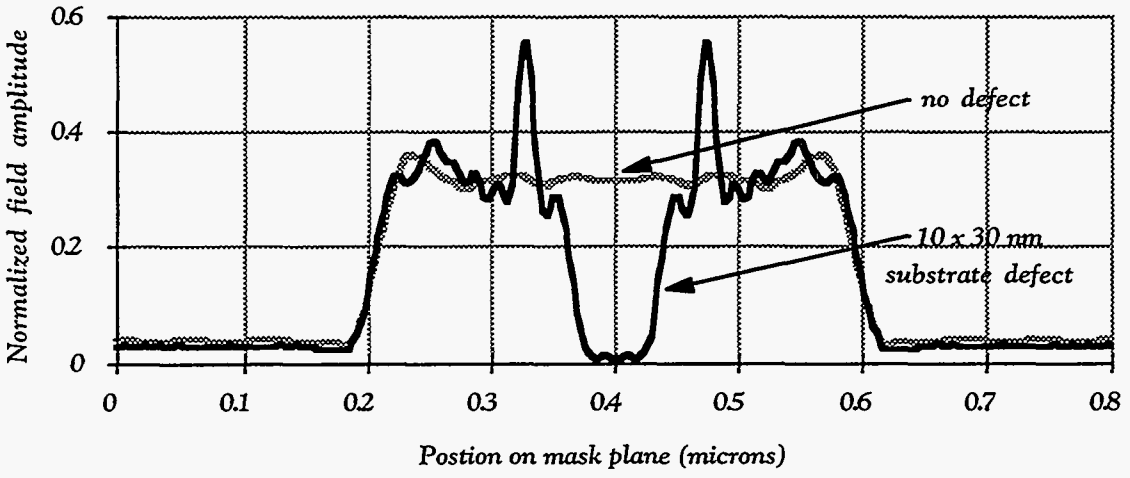

Figure 4.7. Reflected field intensities from masks with and without defect. The defect creates phase changes and zero crossings in the reflected field, thus reducing the aerial image intensity.

The reflected field intensity from the uncapped 10 x 30 nm defect in figure 4.7 shows that the defect produces phase reversal in the field amplitude and causes zero crossings. While the defect is smaller than the resolution of the imaging system, the zero crossings effectively direct more power into higher diffracted orders of the reflected field and reduces power in the lower orders collected by the imaging optics. As a result, the intensity and contrast of the aerial image is significantly reduced in the presence of a substrate defect.

Due to phase effects, the magnitude of the reduction in image intensity may be sensitive to the illumination wavelength. The illumination bandwidth on the mask in an EUVL printer would be controlled by the passband of the condensers coated with multilayer reflective coating. To simulate illumination with finite bandwidth, aerial images were calculated for masks with 4 X 30 nm substrate defects illuminated with 13 nm to 13.9 nm wavelength radiation. A thickness of 4 nm corresponds to approximately a $\lambda/2$ phase shift for these wavelengths.

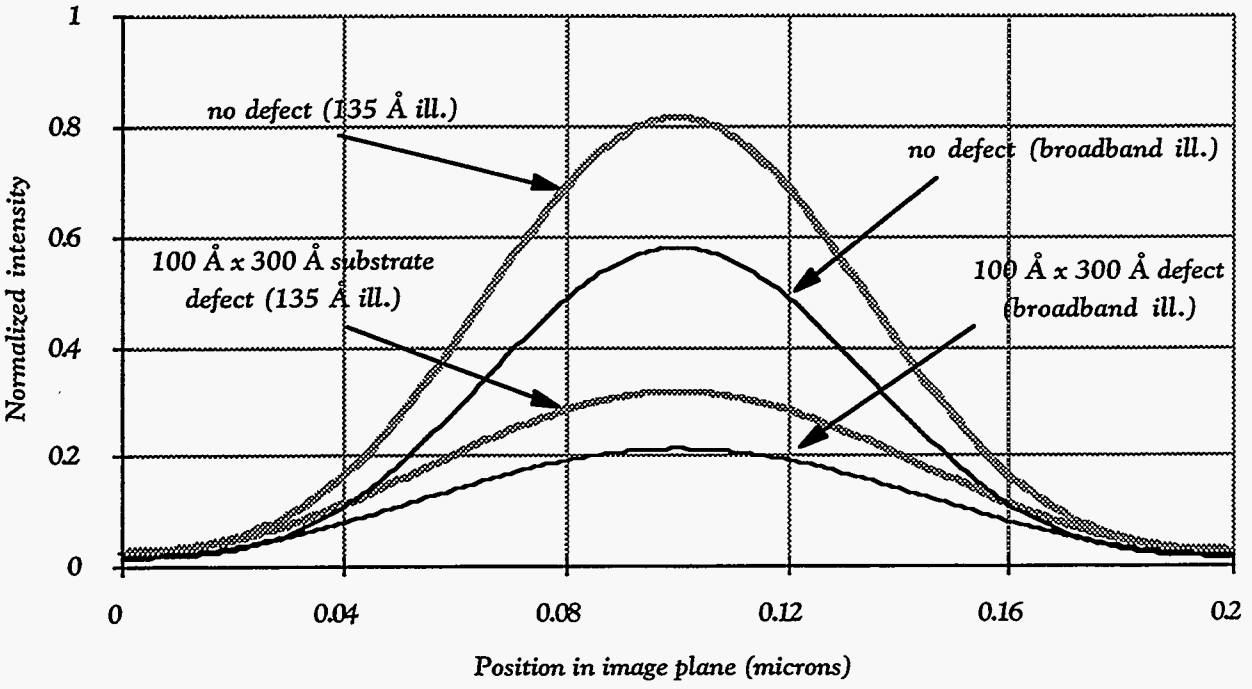

Figure 4.8. Effect of substrate defect on images under broadband and monochromatic illumination for a 100 X 300 Å substrate defect. The reflective peak for the coating is centered around 135 Å. Under either illumination condition, the peak image intensity is reduced by 60% by the presence of the defect.

The aerial images were calculated for ten wavelengths, from 13 nm to 13.9 nm in 0.1 nm increment . The results were then added and averaged over the number of wavelengths. Interactions between different wavelengths were ignored, since interferences between different wavelengths would result in moving patterns that average out over the length of the exposure time. Figure 4.8 shows that for both single- and multi-wavelength illumination, the presence of a 4 x 30 nm defect line produces ~ 60% reduction in image intensity.

The results in this section show that substrate defects result in larger reduction in aerial image intensity compared to absorber defects of the same size. In the following sections, the results of a systematic study of the effect of multilayer defects on aerial images will be described, showing how the aerial images vary for different defect sizes, defect positions, and film coverage profiles. Since the difference between the image intensity reductions for multi-wavelength and single-wavelength illumination is small, all the calculations to follow were made with single-wavelength illumination.

4.3.2. Image vs. Defect Size

4.3.2. (a) Image vs. Defect Height.

The effect of defect height was studied by calculating the aerial images from masks with *30 nm wide* defects of different heights. Figure 4.9 shows the aerial images from masks with defects of 1 nm, 3 nm, 4 nm, and 7.5 nm heights. Since phase effects dominate the imaging process for thin coating defects, defects causing a phase shift of greater than $\lambda/4$, i.e. defects thicker than $\lambda/8$ on a reflective mask, would introduce zero crossings into the reflected field. At 13.5 nm illumination wavelength, $\lambda/8$ corresponds to 1.7 nm.

As seen in figure 4.9, while a 1 x 30 nm defect line has little effect on the aerial image, a 3 x 30 nm defect line reduces the image intensity by more than 50% by introducing a phase shift of nearly π . A 4 x 30 nm defect line results in even larger intensity reduction. A 7.5 nm high defect, however, results in smaller intensity reduction than both the 3 nm and 4 nm defects because it causes a phase shift slightly more than 2π for the radiation reflected from the area above the defect. However, π phase shifts occur at the edges of defect due to lateral spreading of defect geometry in the simulated coverage profile. As a result, the reduction in image intensity with a 7.5 nm defect is larger than that with a 1 nm high defect. Thicker defects also result in more scattering from their topographies. The combination of zero crossings at the edges and increased scattering for thicker defects results in the damped oscillatory behavior for image intensity as a function of defect height shown in figure 4.10.

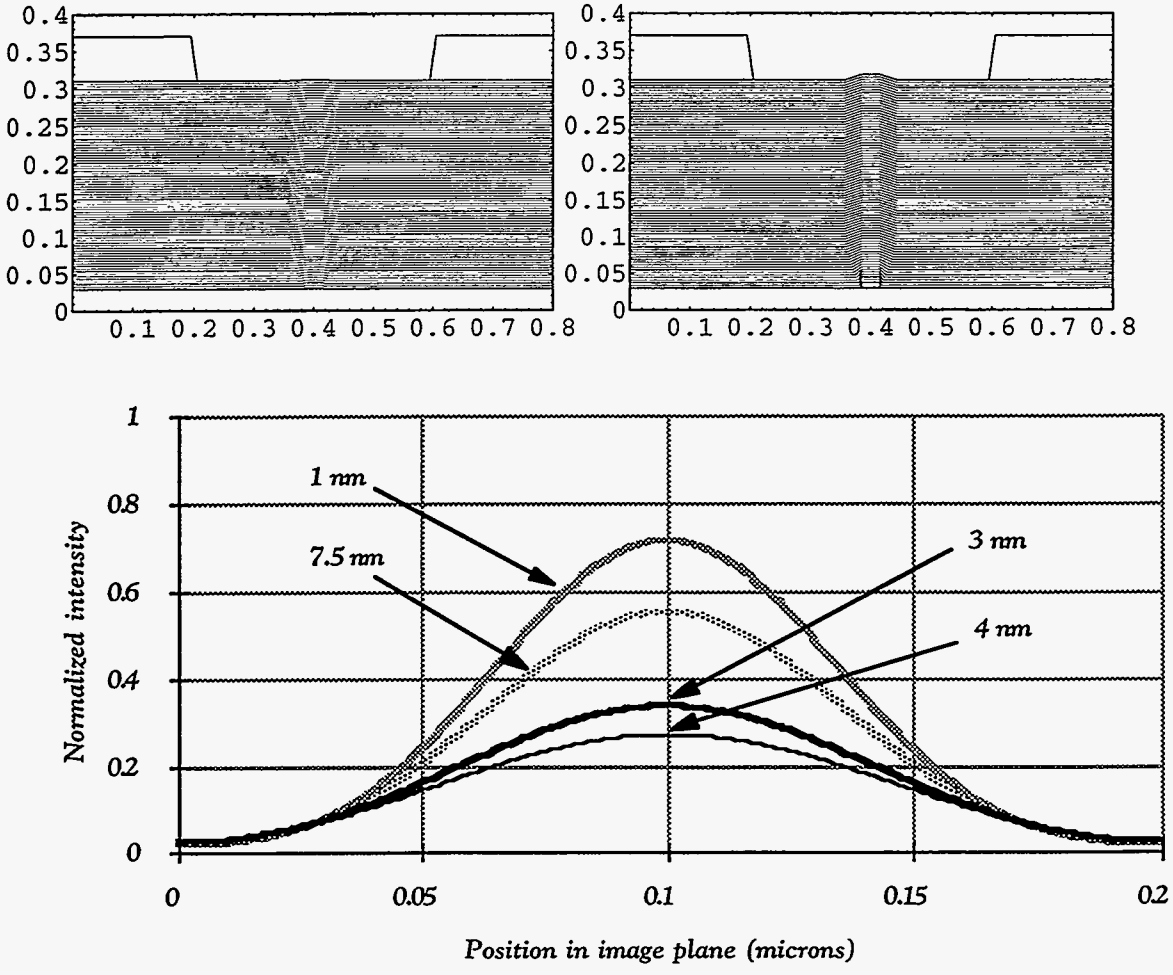

Figure 4.9. Images from masks with 30 nm wide substrate defect with different heights. Simulated mask geometries for 1 nm and 7.5 nm high defects are shown, together with aerial images for defects of 1 nm, 3 nm, 4 nm and 7.5 nm heights. Defects of 3 nm and 4 nm heights result in large intensity reductions because they introduce near-180° phase shifts into the reflected field.

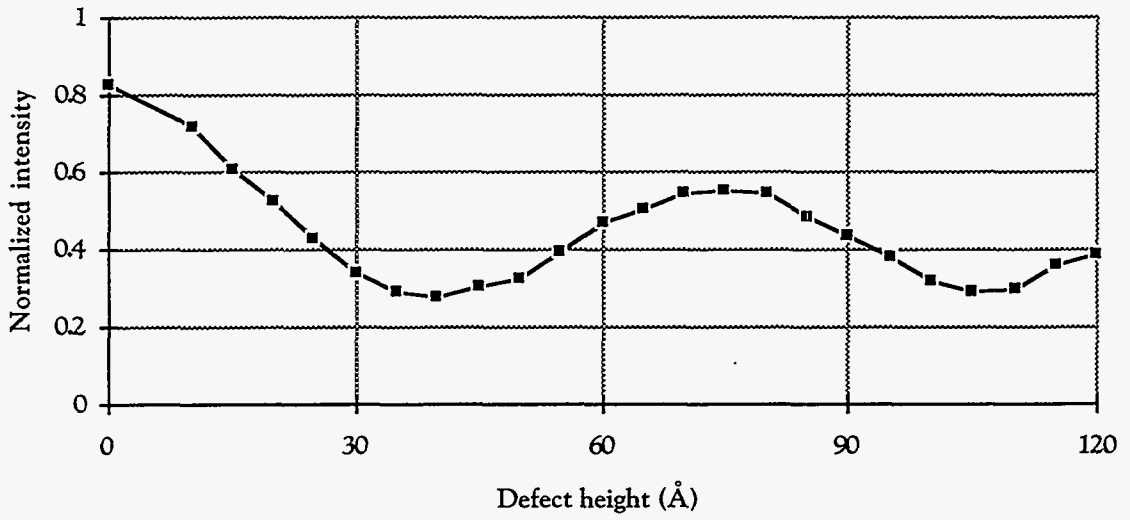

Figure 4.10. Peak image intensity vs. defect height for a 30 nm wide substrate defect. The damped-oscillatory behavior vs. defect height is due to the phase nature of the defects and increased scattering with thicker defects.

4.3.2. (b) Image vs. Defect Width.

The effect of defect width on aerial images was studied by comparing the calculated aerial images of masks with *4 nm* high substrate defects of different widths. Figure 4.11 shows the aerial images and reflected field amplitudes for masks with defects of *5 nm*, *10 nm*, and *20 nm* widths. As expected, wider defects resulted in larger image intensity reduction.

The results show that a 4 x 5 nm defect line causes a 50% reduction in peak image intensity. It is somewhat surprising that such a small line defect can cause such a large decrease in image intensity. However, at small defect dimensions, the physical accuracy of the coverage profile model is questionable. In the two-parameter model, the smoothing of edges and reduction of defect step height were not taken into account. As will be shown in chapter 5, significant smoothing does occur as defects of nm dimensions are covered by 40-bilayer, 7-nm period multilayer coatings.

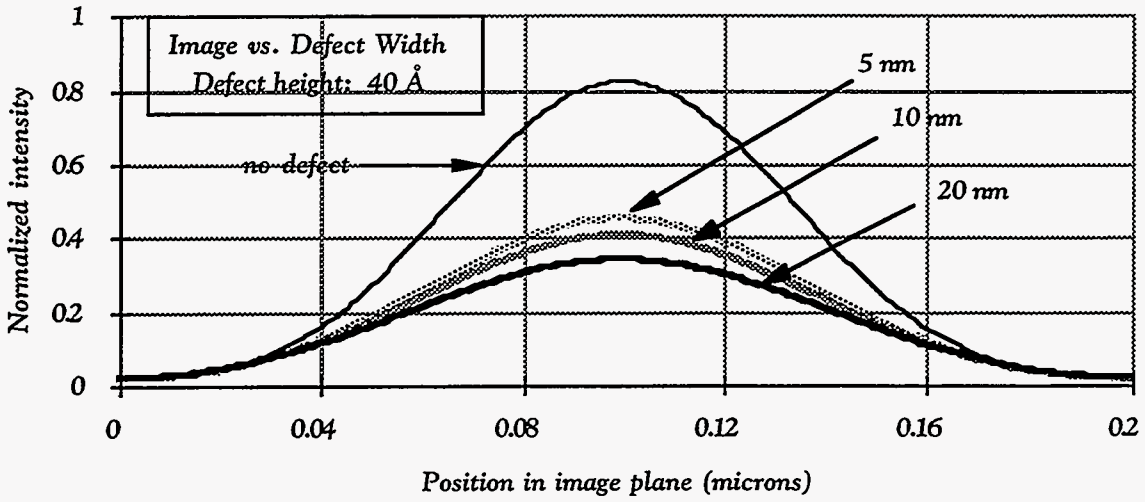

Figure 4.11. Image vs. defect width for 4 nm high substrate defect, showing that very small defects may cause large intensity reduction. However, smoothing of defects was not taken into account in the coating coverage model used in this calculation (figure 4.2).

An example of such a smoothing process is shown in figure 4.12, a TEM cross-sectional image of a 2 nm high by 3 nm wide defect covered by a Mo/Si coating. In this case, the defect is progressively smoothed over as layers of materials are deposited above it. Since most of the reflected light comes from the top layers, such smoothing would result in smaller effective defect height and would reduce the effect of such defects on the aerial image.

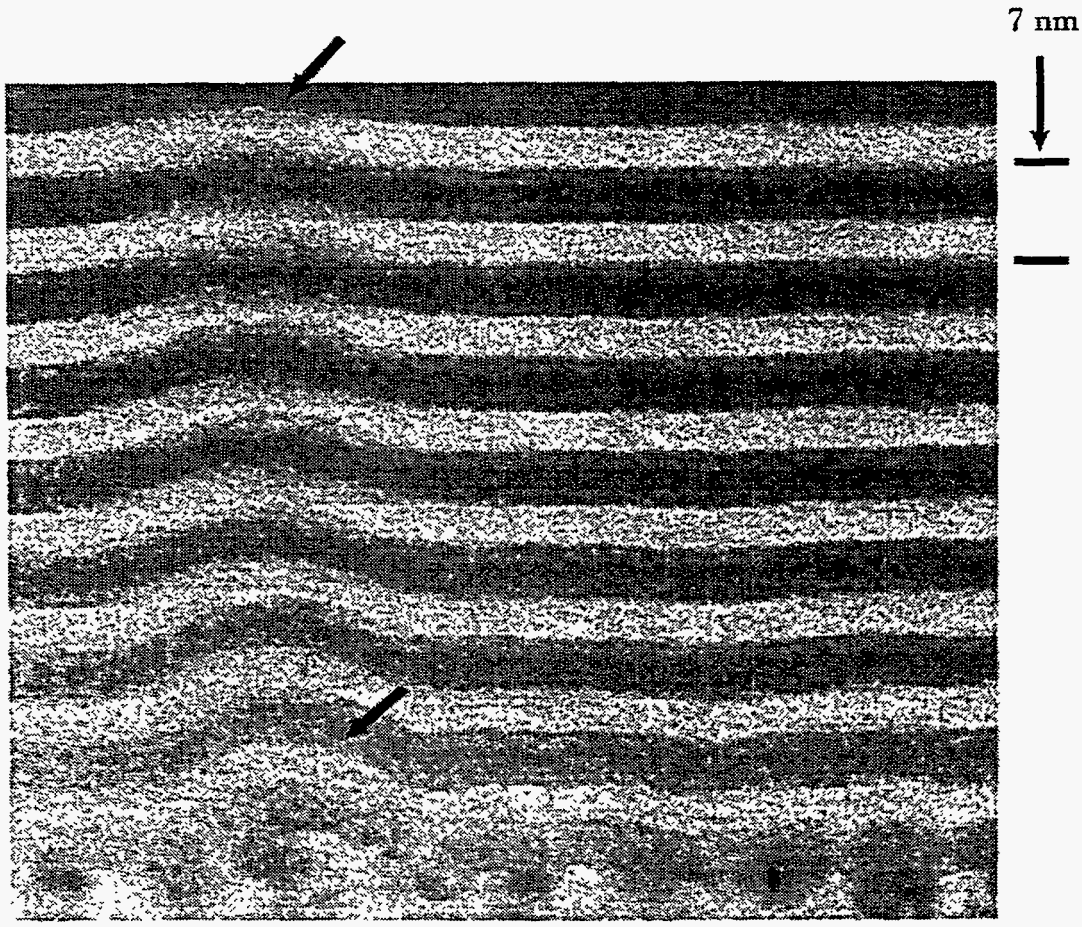

Figure 4.12. A cross-sectional TEM image of Mo/Si coating deposited over rough evaporated gold film. A 2 nm high by 3 nm wide bump, indicated with arrows, is smoothed over as Mo/Si layers are deposited above it. (TEM taken by Tai D. Nguyen)

4.3.3. Image vs. Defect Position

4.3.3 (a). Image vs. Defect Horizontal Position.

The aerial images of masks with 10 x 30 nm defects placed at different vertical and horizontal positions relative to the absorber pattern were calculated to study the effect of defect positions. Figure 4.13 shows images of masks with substrate defects located different horizontal positions. The notations in the figure indicate how far the defect is displaced from the center of the clear region on the mask. Thus a "–0.05 μm" defect is a defect displaced by 0.05 μm to the left of the center on the clear region, and a "+0.15 μm" defect is a defect displaced by that distance to the right. Distances were as measured on the masks. Results show that the largest intensity reduction occurs with the defect centered in the clear region of the mask. Similar behaviors have been observed for phase defects on phase–shifting masks in optical lithography [12]. The closer the defect is to the absorber pattern, the smaller the reduction in intensity. The intensity peaks also shift with defect positions.

Figure 4.14(a) shows the effect of defect position on image intensity. The image intensity increased by a factor of 2 as the defect is shifted by 0.15 μm from the center of the mask's clear region. The increase in intensity was slightly different when the defect was shifted in opposite directions due to the 5° off-normal incident angle in this study.

The locations of the image intensity peak also varied with defect positions. As the defect was shifted away from the center of the clear region, the image intensity peak was shifted in the opposite direction. Figure 4.14(b) shows that the largest change in peak positions occurs as the defect is shifted around the center of the clear region. As the defect shifts to the left (to the negative x-direction) by 0.05 μm on the mask, it shifts to the right (positive y-direction) by 0.015 μm on the image plane. At 4:1 reduction imaging, 0.05 μm on the mask correspond to 0.0125 μm on the image plane. Therefore, a shift of defect position on the mask has resulted in a slightly larger shift in the opposite direction for the image peak. Further shifts of defect position away from the center of the clear region have less impact on the image peak's position. In fact, as the defect is moved more than 0.1 μm *away* from the center of the clear region, the image peak shifts *toward* the center of the clear region.

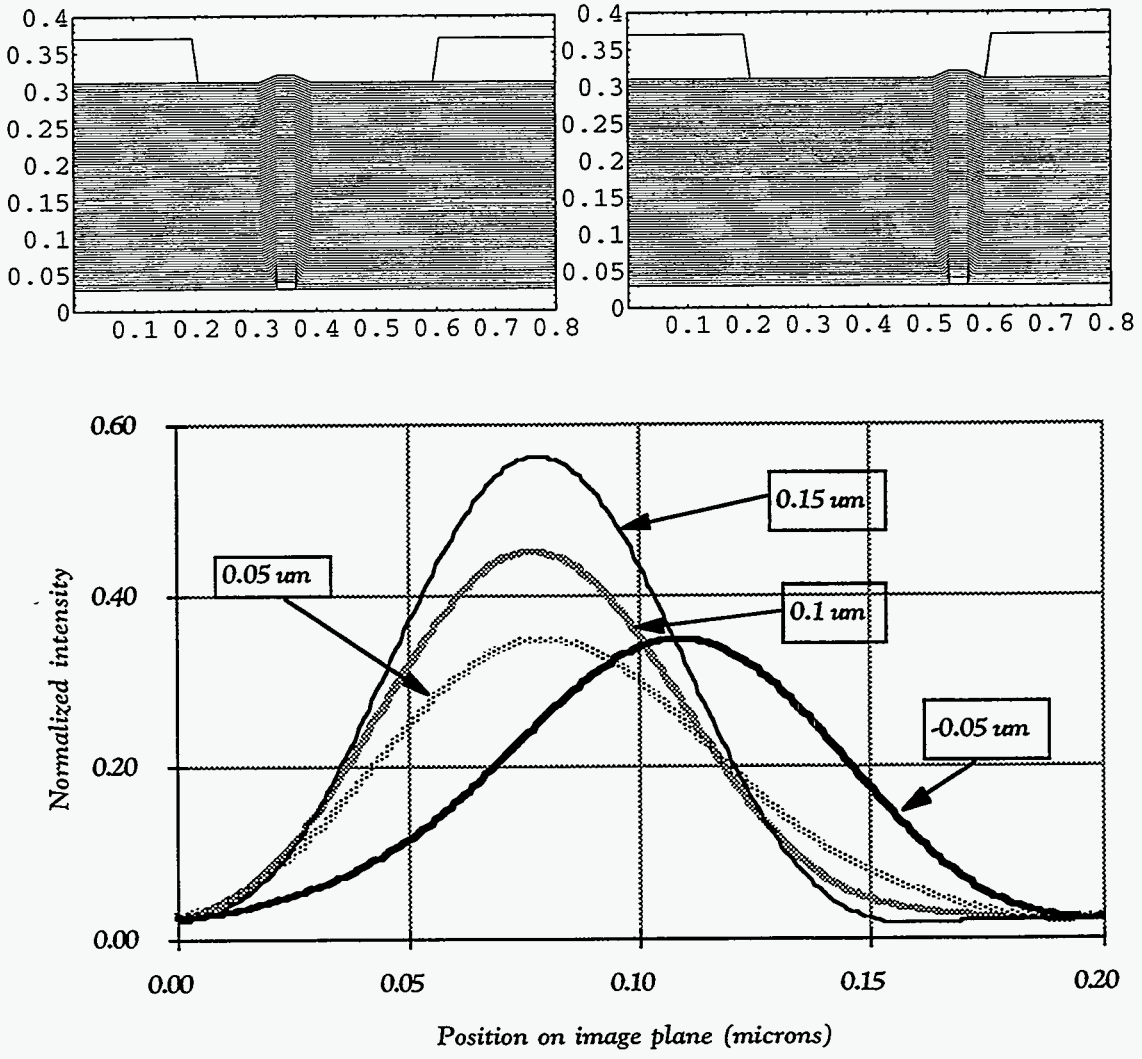

Figure 4.13. Images from masks with 10 x 30 nm substrate defects at different horizontal positions relative to the center of the clear region on the mask. The notations indicate how far the defect is displaced from the center to clear region on the mask. Geometries corresponding to defect positions of – 0.05 μm and 0.15 μm are shown.

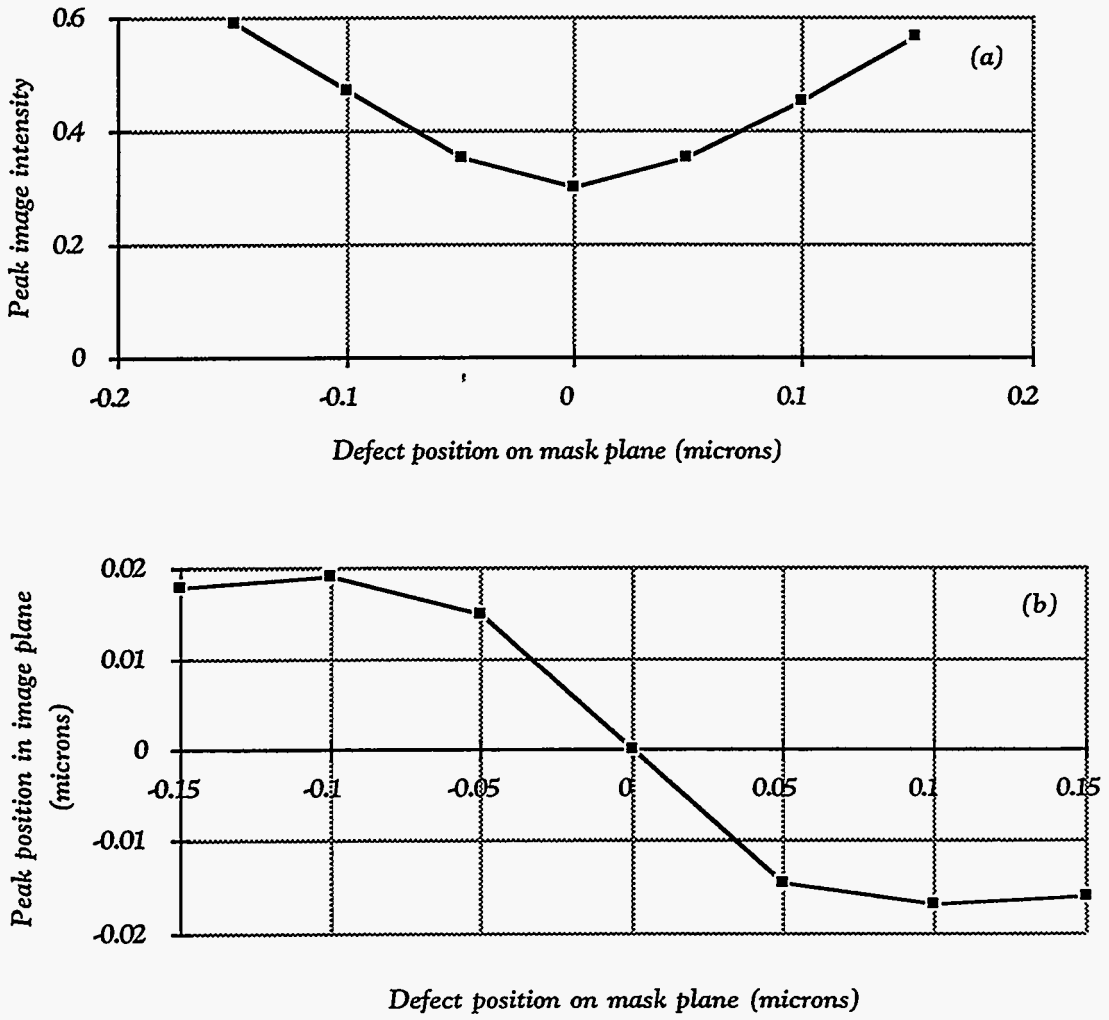

Figure 4.14. (a) Effect of defect position on image intensity peaks. The substrate defect is 10 x 30 nm as measured on the mask. Largest reduction in image intensity occurs when defect is located at the center of the clear region. (b) Effect of defect position on aerial image position. The position of image intensity peaks shift in the opposite direction of the defect position. The largest change in peak position occurs as the defect position is moved around the center of the clear region, i.e. from -0.05 μm to 0.05 μm from the center of the clear region on the mask. Further shifts in defect position have lesser effects.

The behavior of the peak intensity and peak position can be explained in part by examining the reflected fields (figure 4.15). The defect, by creating zero crossings in the reflected field, has effectively created two smaller lines from one 0.4 μm line on the mask. As the defect is shifted from the center, the position of the zero crossing shifts along with it, making one line larger at the expense of the other.

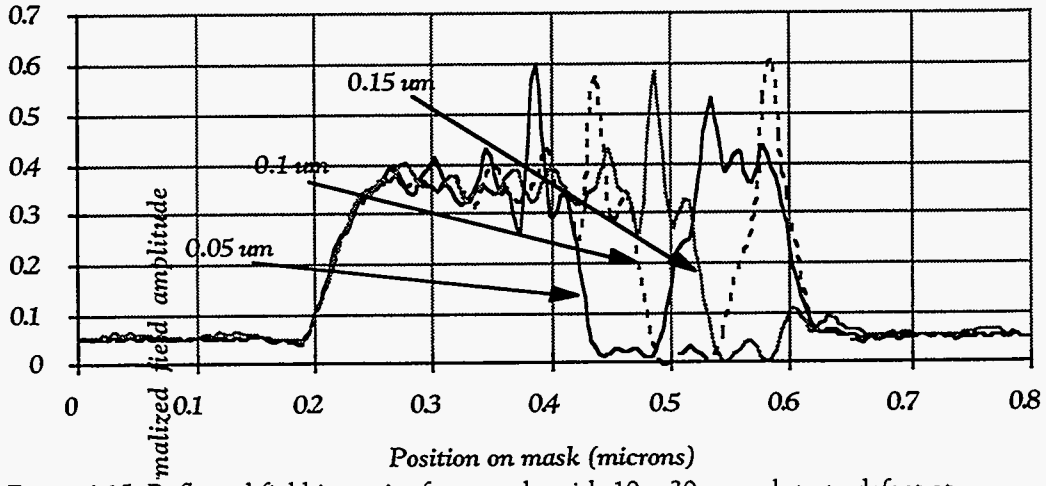

Figure 4.15. Reflected field intensity from masks with 10 x 30 nm substrate defect at different horizontal positions, relative to the center of the clear region of the mask Numbers on the graph indicated displacement from center of the clear region on the mask.

The results show that the image intensity was dominated by the larger feature and increased with larger defect shifts from center because that feature was effectively larger. The peak position was similarly dominated by the larger feature. As the defect was shifted toward the absorber, the center of the larger line shifted first in the opposite direction of the defect, and then in the same direction with the defect as shown in figure 4.13(b). A defect under the absorber layer had no effect the image.

4.3.3 (b). Image vs. Defect Vertical Position.

The effect of the defect's vertical position was studied by comparing aerial images from masks with *10 x 30 nm* defects *centered in the clear region* located at *different vertical positions* in the multilayer stack. Figure 4.16(a) shows masks with 10 x 30 nm defects located at the 10^{th} bilayer and 30^{th} bilayer from the top. Figure 4.16(b) shows the images from masks with 10 x 30 nm defects at different vertical positions – on top of the multilayer coating, above the 10^{th} layer pair, above the 20^{th} layer pair, and above the

30th layer pair. The results show that the deeper the defect is located in the coating, the larger the reduction in image intensity. They also show that the reduction in intensity is largest when the defect is shifted from the top layer to the 10th layer, and is smaller when the defect is shifted from the 10th to 20th layer, and smaller still for subsequent shifts.

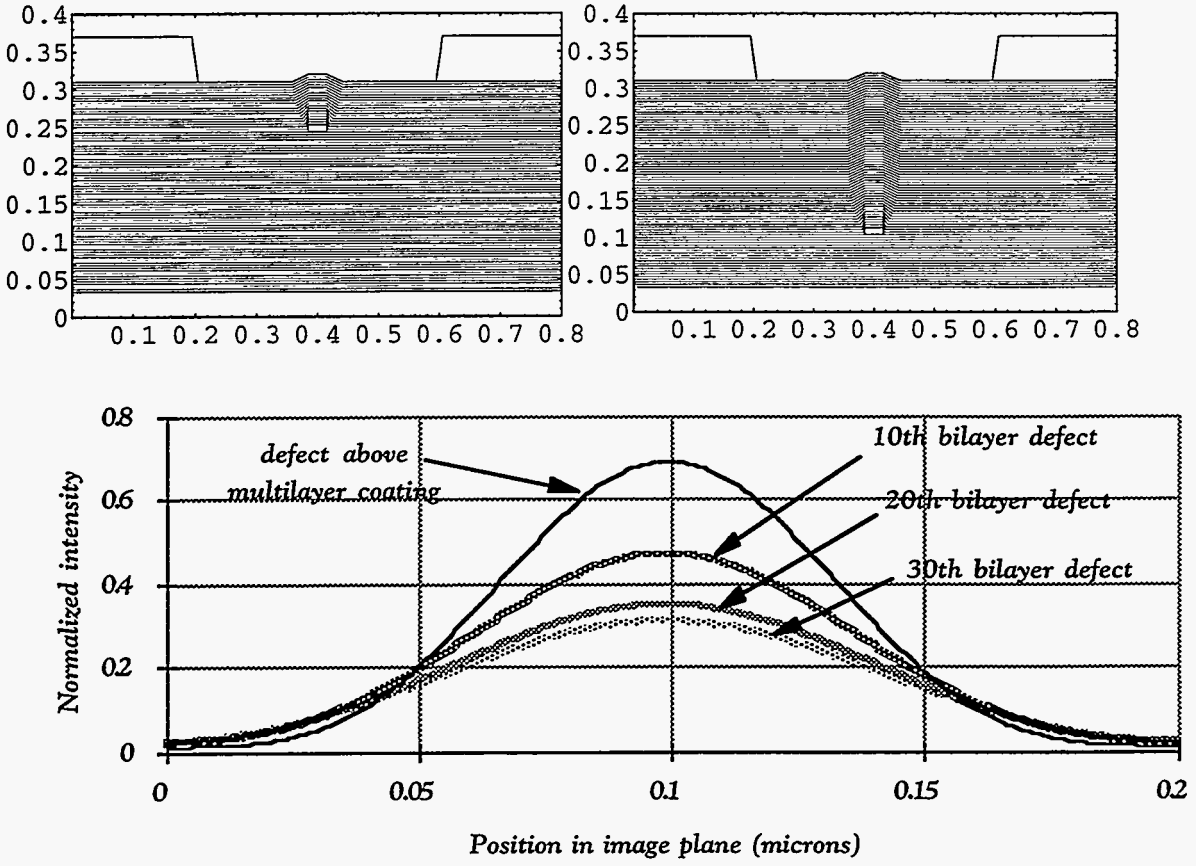

Figure 4.16. Images of masks with 10 x 30 nm defect at different vertical positions in the multilayer stack. Geometries for defect at 10th and 30th bilayers from the top are shown. f_{damp} is 0.8 for all cases.

At least two factors contributed to this behavior. First, since the out-of-phase component of the reflected radiation results from reflections off the layers above the defect, deeper defects result in larger out-of phase components in the reflected fields, hence larger reductions in image intensity. This result is analogous to those obtained for capped defects (see figure 4.6). The second factor contributing to the larger intensity reduction with deeper defect is the lateral spreading of defect profiles.

To estimate the relative contributions of these two effects, the calculations were repeated for a 10 x 30 nm with f_{damp} of 0.2 corresponding to virtually no lateral propagation (see figure 4.17). Any differences in image intensity reduction between cases with f_{damp} of 0.8 and f_{damp} of 0.2 can be attributed primarily to lateral propagation of the defect topography.

Figure 4.18 shows that lateral spreading of defect profile results in an additional 15% image intensity reduction for defects located on the 10th bilayer from the top, 30% for 20th bilayer defects, and 40% for 30th bilayer defects. With no lateral spreading, the decrease in image intensity saturated with deeper defects since the lower layers of the coatings contributed less and less to the reflected field. With lateral spreading, deeper defects resulted in larger effective defect sizes at the upper layers, thus effected the larger image intensity reductions.

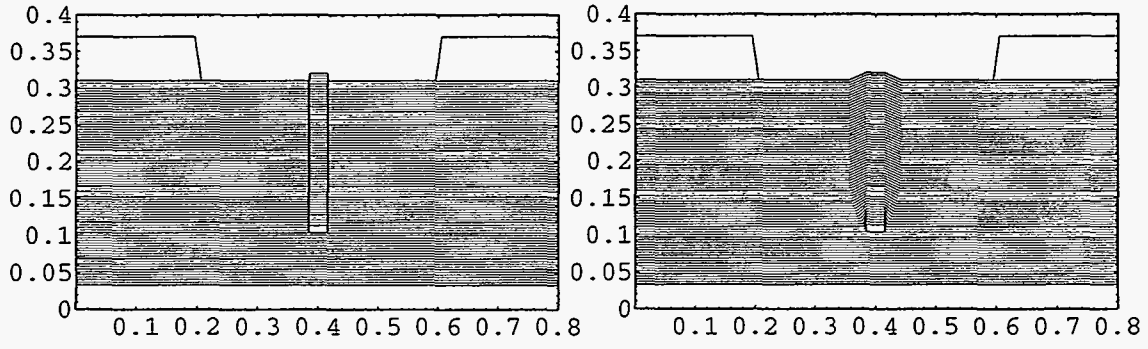

Figure 4.17. Simulated masks for calculations of images under different vertical defect position, for two different coverage profiles — f_{damp} = 0.2 and f_{damp} = 0.8.. Defects located at the 30th bilayer from the top are shown.

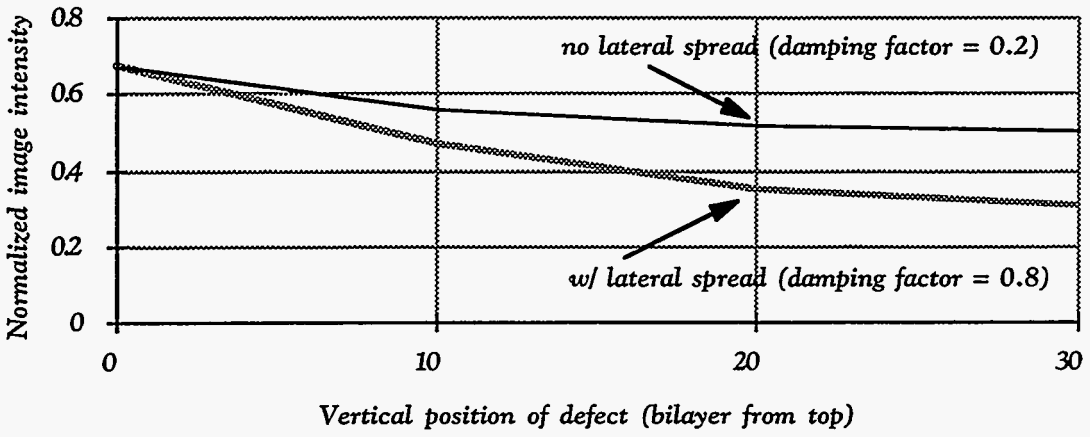

Figure 4.18. Aerial image intensity vs. vertical defect position for two different coverage profiles. With defects at the same position, lateral spreading of defect geometry (f_{damp} = 0.8 vs. f_{damp} = 0.2) results in larger reduction in image intensity.

4.3.4. Image vs. Defect Coverage Profile

Results from the previous section suggest that different multilayer coating coverage profiles would result in different aerial images for the same defect on the substrate. To study the effect of coverage profile, aerial images from masks with 10 x 30 nm substrate defect were calculated for four different damping factor f_{damp} — 0.3, 0.6, 0.8 (the standard coverage profile), and 0.9 (figure 4.19).

Figure 4.20 shows that larger lateral spreading of the defect geometry due to coating deposition resulted in larger reductions in image intensity by increasing the defect's effective size. An experimental study into the defect coverage profile of sputtered deposited Mo/Si multilayer reflective coatings is the subject of the next chapter [25].

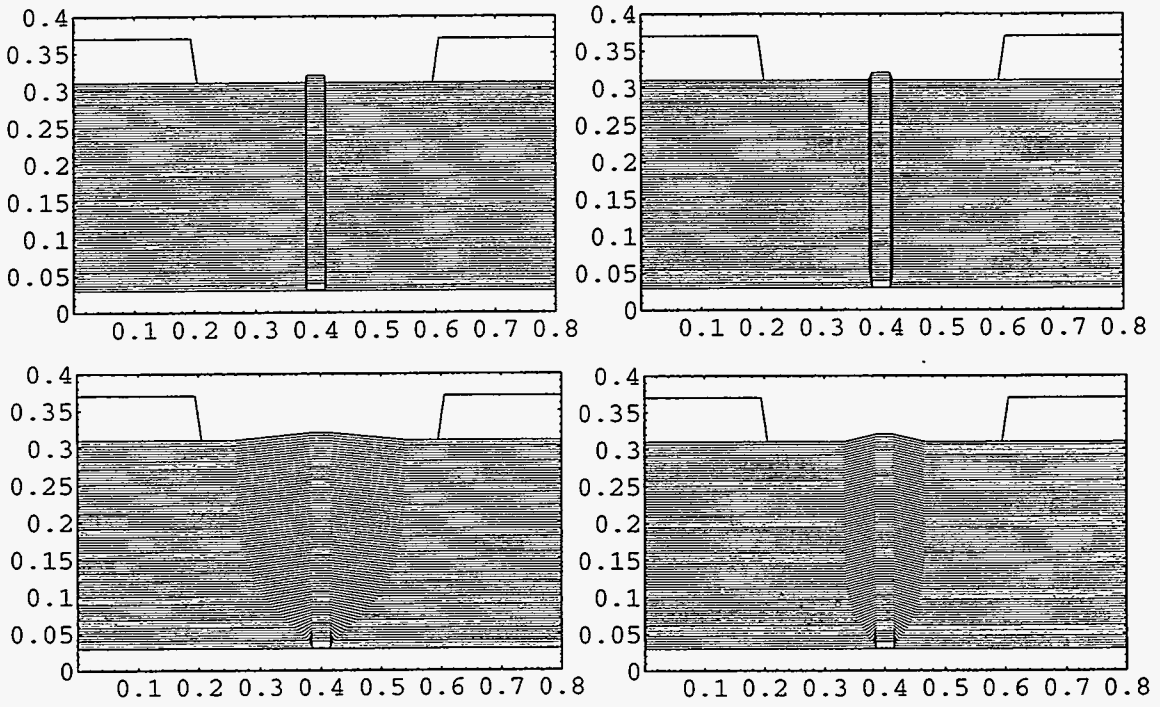

Figure 4.19. Masks with 10 nm x 30 nm substrate defects for four different coverage profiles. To obtain the profiles, f_{side} was set to be 0.4 and f_{damp} set to be 0.3, 0.6, 0.85 and 0.9. Larger f_{damp} corresponds to greater lateral propagation of defect geometry.

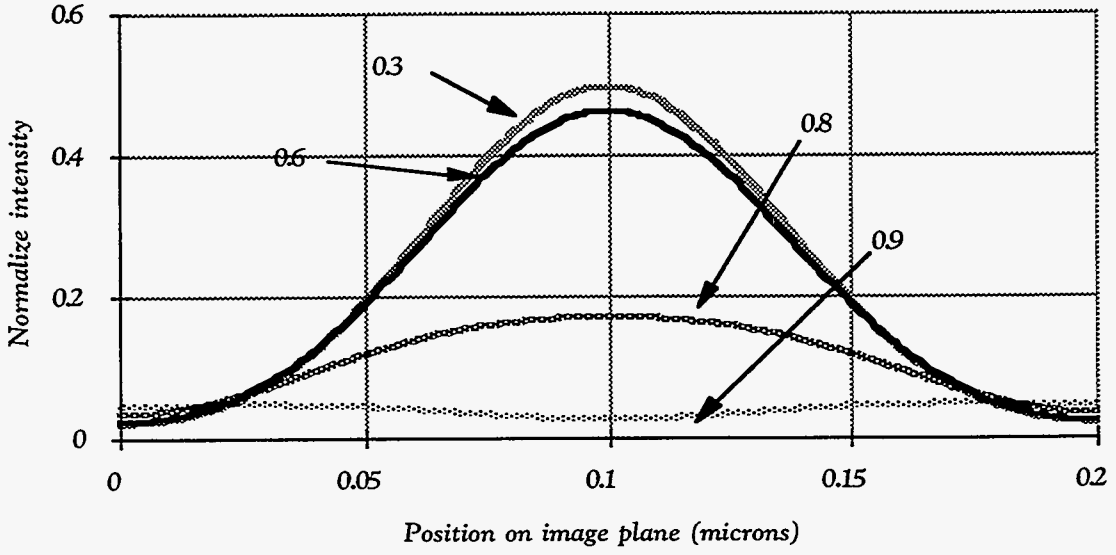

Figure 4.20. Images from masks with 10 nm x 30 nm substrate defect for different coverage profiles. corresponding to different damping factor f_{damp}.

4.4. Conclusion

Electromagnetic simulations of aerial images from EUVL masks with defects in the reflective coatings show that substrate and coating defects can have significant effects on the images. Since coating defects produce phase variations in the reflected field, defects thicker than $\lambda/8$ on a reflective mask can cause large reductions in image intensities. At an illumination wavelength of ~ 13 nm, defects of 2 nm thick can have a significant effect on the image.

Aerial image intensity decreases in a damped-oscillatory manner with increasing defect height and in a monotonic manner with increasing defect width. Defects located on the substrate and at the center of clear region on the mask cause the largest image intensity reductions.

The manner in which the substrate defect is covered by the multilayer coating deposition process also affects the image. Since the upper layers of the multilayer stack contribute the major share of the reflected light, a larger lateral.spreading of the defect increases its effective size at the top layers and thus increasing its effect on the aerial image.

Figure 4.21 summarizes the results of this chapter. It shows a high–printability defect – one that is on substrate, in the center of the clear region with large lateral spreading, and a low-printability defect – one that is close to the top of the coating, close to the absorber pattern with little lateral spreading.

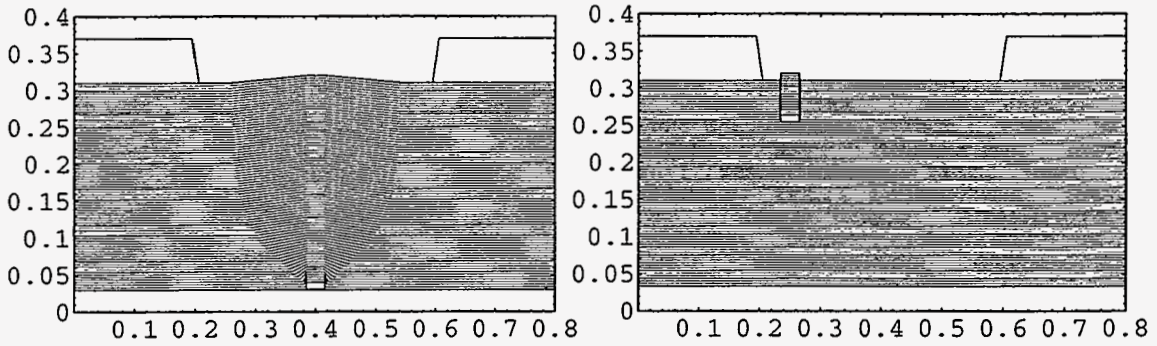

Figure 4.21. High printability defect vs. low printability defect. (a) A high printability defect — a defect in the center of the clear area, having large lateral spreading due to coverage profile and located on the substrate, (b) a low printability defect — one that is close to the absorber line, has little lateral propagation and is located in the upper layers of the multilayer coating.

References

1. A.M. Hawryluk, N.M. Ceglio, and D.P. Gaines, "Reflection mask technology for x-ray projection lithography," Journal of Vacuum Science and Technology B, **7**(6), pages 1702-1704 (1989).

2. A.M. Hawryluk, N.M. Ceglio, D.W. Phillion, D.P. Gaines, R. Browning, R.F. Pease, D. Stewart, and N. Economou, "Reflection mask technology for soft x-ray projection lithography," *Soft x-ray projection lithography* (Monterey, CA, USA), *OSA Proceedings*, vol. 12, J. Bokor ed., pages 45-50 (Optical Society of America, Washington, D. C., USA, 1991).

3. D.M. Tennant, J.E. Bjorkholm, R.M. D'Souza, L. Eichner, R.R. Freeman, J.Z. Pastalan, L.H. Szeto, O.R. Wood II, T.E. Jewell, W.M. Mansfield, W.K. Waskiewicz, D.L. White, D.L. Windt, and A.A. MacDowell, "Reflective mask technologies and imaging results in soft x-ray projection lithography," Journal of Vacuum Science and Technology B, **9**(6), pages 3176-3183 (1991).

4. D.M. Tennant, J.E. Bjorkholm, L. Eichner, R.R. Freeman, T.E. Jewell, A.A. MacDowell, J.Z. Pastalan, L.H. Szeto, W.K. Waskiewicz, D.L. White, D.L. Windt, and

O.R. Wood II, "Comparison of reflective mask technologies for soft x-ray projection lithography," *BACUS Symposium on Photomask Technology , SPIE Proceedings*, vol. 1604, pages 91-104 (The International Society of Optical Engineering (SPIE), Bellingham, WA, 1991).

5. R. Murphy, D. Flesberg, T. Reilly, and J. Reynolds, "The printability of particles on 5X reticles," *12th Annual BACUS Symposium* (San Jose, CA, USA), *SPIE Proceedings*, vol. 1809, pages 146-157 (The Internatinal Society for Optical Engineering, Bellingham, WA, USA, 1992).

6. R.J. Socha, A.R. Neureuther, and R. Singh, "Printability of phase-shift defects using a perturbational model," *13th Annual BACUS Symposium on Photomask Technology and Management, Proceedings* (San Jose, CA, USA), *SPIE Proceedings*, pages 277-287 (The International Society of Optical Engineering, Bellingham, WA, USA, 1994).

7. J.N. Wiley, T.Y. Fu, T. Tanaka, S. Takeuchi, S. Aoyama, J. Miyazaki, and Y. Watakabe, "Phase shift mask pattern accuracy requirements and inspection technology," *Integrated Circuit Metrology, Inspection and Process Control V* (San Jose, CA, USA, 4-5 March 1991), *SPIE Proceedings*, vol. 1464, W.H. Arnold ed., pages 346-355 (The International Society for Optical Engineering, Bellingham, WA, USA, 1991).

8. J.N. Wiley, and J.A. Reynolds, "Device yield and reliability by specification of mask defects," Solid State Technology, (July), (1993).

9. G. Arthur, and B. Martin, "Modelling the printability of sub-micron 5X reticle defects at I-line exposure wavelength," Microelectronic Engineering, 23, pages 167-170 (1994).

10. P. Canestrari, S. Carrera, G. Degiorgis, and V. Visentini, "Impact of reticle defects on submicron 5x lithography," *Integrated Circuit Metrology, Inspection and Process Control IV* (San Jose, CA, USA, 5-6 March, 1990), *SPIE Proceedings*, vol. 1261, W.H. Arnold ed., pages 225-237 (The International Society for Optical Engineering, Bellingham, WA, USA, 1990).

11. S.K. Dunbrack, A. Murray, C. Sauer, R.L. Lozes, J. Nistler, W.H. Arnold, D. Kyser, A. Minvielle, M. Preil, B. Singh, and M.K. Templeton, "Phase-shift mask

technology: requirements for e-beam mask lithography," *Integrated Circuit Metrology, Inspection and Process Control V* (San Jose, CA, USA, 4-5 March 1991), *SPIE Proceedings*, vol. 1464, W.H. Arnold ed., pages 314-326 (The International Society for Optical Engineering, Bellingham, WA, USA, 1991).

12. T.Y. Fu, "Pattern design and tolerancing analysis of phase-shifting masks," BACUS News, 8(1), pages 1-8 (1992).

13. B.J. Grenon, K.D. Badger, and M.J. Trybendis, "Reticle defect sizing and printability," *11th Annual Symposium on Photomask Technology* (Sunnyvale, CA, USA, 25-27 Sept. 1991), *SPIE Proceedings*, vol. 1604, pages 179-195 (The International Society for Optical Engineering, Bellingham, WA, USA, 1991).

14. Y.M. Ham, I.B. Hur, Y.S. Kim, D.J. Ahn, Z. Cha, S.S. Choi, H. Kim J., and Y.J. Jeon, "Dependence of defects in optical lithography," Japanese Journal of Applied Physics, Part 1 (Regular Papers & Short Notes), **31**(12B), pages 4137-4142 (1992).

15. T. Kikuchi, K. Shigematsu, M. Tominaga, H. Maruyama, T. Furukawa, and I. Yanagida, "Effects of sub-half-micron mask defects on wafer images during VLSI circuit production," *Optical/Laser Microlithography II* (San Jose, CA, USA), *SPIE Proceedings*, vol. 1088, B.J. Lin ed., pages 48-57 (The International Society for Optical Engineering, Bellingham, WA, USA, 1989).

16. M. Kohno, N. Kodachi, K. Yajima, and S. Miura, "Subhalf micron stepper with a reticle monitor," *Optical/Laser Microlithography VI* (San Jose, CA, USA), *SPIE Proceedings*, vol. 1927, J.D. Cuthbert ed., pages 568-581 (The International Society for Optical Engineering, Bellingham, WA, USA, 1993).

17. K.-D. Roth, W. Maurer, and C. Blasing-Bangert, "Metrology on phase shift masks," *Integrated Circuit Metrology, Inspection and Process Control VI* (San Jose, CA, USA, 9-11 March 1992), *SPIE Proceedings*, vol. 1673, M.T. Postek ed., pages 214-220 (The International Society for Optical Engineering, Bellingham, WA, USA, 1992).

18. H. Watanabe, Y. Todokoro, and M. Inoue, "Detection and printability of shifter defects in phase-shifting masks," Japanese Journal of Applied Physics, Part 1 (Regular Papers & Short Notes), 30(11B), pages 3016-3020 (1991).

19. H. Watanabe, E. Sugiura, T. Imoriya, Y. Todokoro, and M. Inoue, "Detection and printability of shifter defects in phase-shifting masks. II.Defocus characteristics," Japanese Journal of Applied Physics, Part 1 (Regular Papers & Short Notes), **31**(12B), pages 4155-4160 (1992).

20. J.N. Wiley, "Effect of stepper resolution on the printability of submicron 5X reticle defects," *Optical/Laser Microlithography II* (CA, USA), vol. 1088, pages 58-73 (The International Society of Optical Engineering, Bellingham, WA, USA, 1989).

21. L.S. Zubrick, "Detection and criticality of transmission variations on 5X reticles," BACUS News, **9**(9), pages 1-9 (1993).

22. D.M. Tennant, L.A. Fetter, L.R. Harriott, A.A. MacDowell, P.P. Mulgrew, W.K. Waskiewicz, D.L. Windt, and O.R. Wood II, "Defect repair for soft x-ray projection lithography masks," Journal of Vacuum Science and Technology B, **10**(6), pages 3134-3140 (1992).

23. A.M. Hawryluk, and D. Stewart, "Repair of opaque defects on reflection masks for soft x-ray projection lithography," Journal of Vacuum Science and Technology B, **10**(6), pages 3182-3185 (1992).

24. K.B. Nguyen, A.K. Wong, A.R. Neureuther, and D.T. Attwood, "Effects of absorber topography and multilayer coating defects on reflective masks for soft X-ray/EUV projection lithography," *Electron-Beam, X-Ray, and Ion-Beam Submicrometer Lithographies for Manufacturing III* (San Jose, CA, USA), *SPIE Proceedings*, vol. 1924, D.O. Patterson ed., pages 418-34 (The International Society for Optical Engineering, Bellingham, WA, 1993).

25. K.B. Nguyen, and T.D. Nguyen, "Defect coverage profile and propagation of roughness of sputter-deposited Mo/Si multilayer coating for extreme ultraviolet projection lithography," Journal of Vacuum Science and Technology, **11**(6), pages 2964-2970 (1993).

Chapter 5

Defect coverage profiles in sputter-deposited Mo/Si multilayer coatings

5.1. Introduction

Electromagnetic simulations described in chapter 4 indicate that defects in the multilayer reflective coatings on EUVL masks can cause significant reductions in image intensity. The magnitude of the reductions depends on the size and position of the defects, and on the defect coverage profiles.

This chapter describes an experimental study of the defect coverage profiles for sputtered deposited Mo/Si multilayer coatings with atomic force microscopy (AFM) [1, 2] and transmission electron microscopy (TEM) [3]. The coverage profiles were characterized in terms of changes in the step heights, edge slopes, linewidths. The evolution of roughness due to the deposited coatings was also studied by measuring the roughness of the samples before and after multilayer coating deposition. An AFM was used to measure these quantities and a TEM was used to qualitatively confirm the observed trends.

5.2. Experimental Setup

5.2.1. Sample preparation

Four different samples with programmed defects were observed with an AFM before and after multilayer coating depositions to quantify how the deposited coatings affect the profiles of the defects. Sample geometries are shown in figure 5.1. Two of the samples had on them *0.15 μm wide and 30 nm thick* nickel lines-and-spaces patterned with electron beam lithography, electroplating and lift-off (figure 5.1(a)). One of these two samples was coated with 40 bilayers of Mo/Si with bilayer thickness of 7 nm, resulting in a total film thickness of 280 nm (figure 5.1(c)). The other sample was coated first with a 200 nm Si buffer layer before the 40 bilayers of Mo/Si was deposited, resulting in a total film thickness of 480 nm (figure 5.1(d)). Both samples were coated in a single deposition run. These samples were used to study how the step heights, edge slopes and linewidths are affected by the deposited film.

Two other samples had on them *2 μm wide and 20 nm thick* gold lines-and-spaces patterned with optical lithography, evaporation and lift-off (figure 5.1(b)). Once again, 40 bilayers of Mo/Si with 7 nm-period were deposited on the samples, one of which was also coated with an additional 200 nm Si buffer layer (figure 5.1(c), 5.1(d)). The gold films were quite rough and were useful for studying how roughness and small features with sizes of a few nanometers are affected by the coating deposition process.

Approximately ten other samples were prepared for TEM observations. These consisted of 40 bilayers of 7 nm-period Mo/Si multilayer coatings deposited over gold steps. The step heights ranged from 2 nm to 15 nm. All multilayer coatings in this study were deposited under conditions similar to those described in chapter 3.

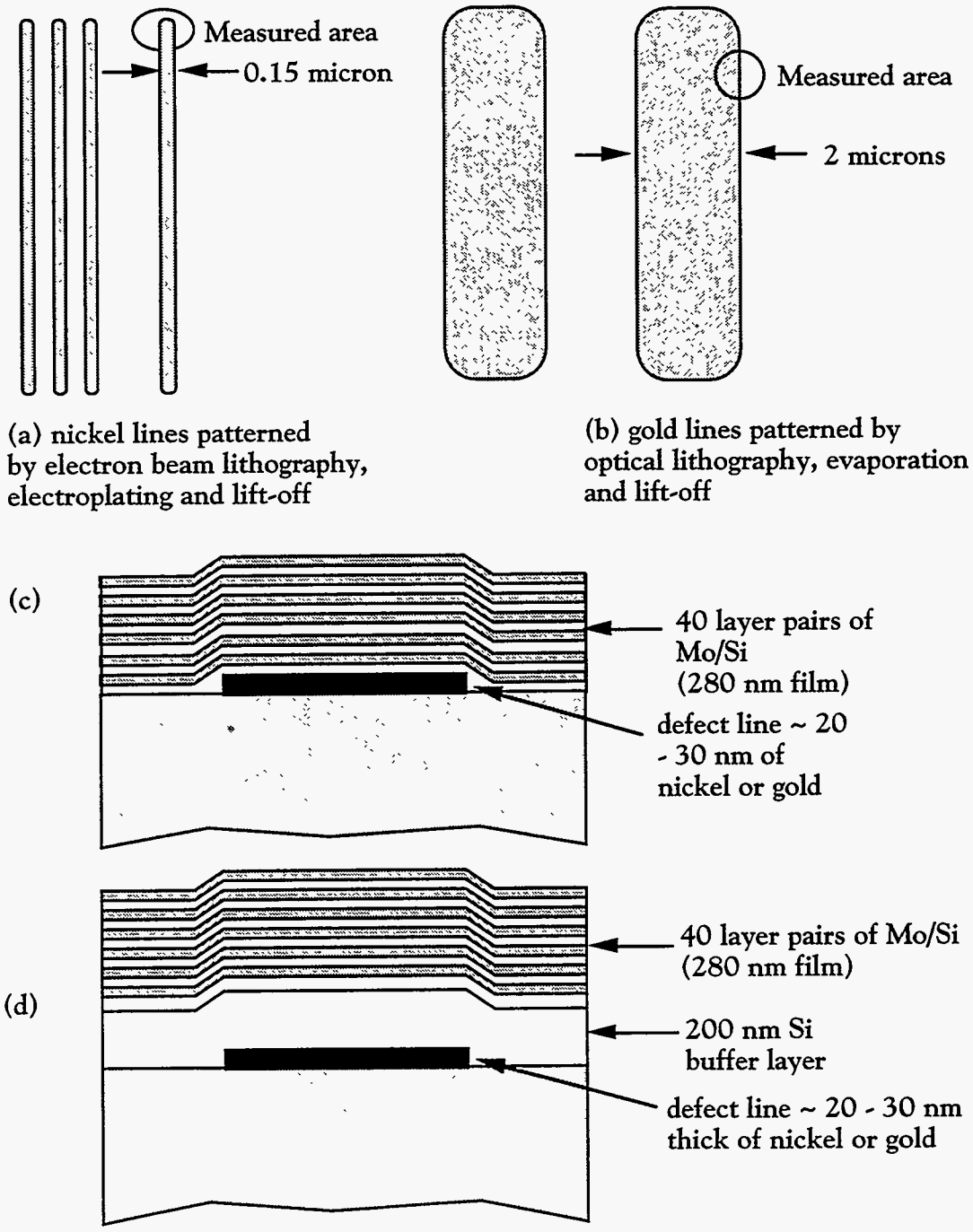

Figure 5.1. A diagram of sample geometries for the four samples observed under AFM, (a) top view of electroplated 0.15 μm wide, 30 nm high nickel lines, (b) top view of evaporated 2 μm wide, 20 nm high gold lines, (c) cross sectional view of sample covered by multilayer coating, (d) cross sectional view of sample covered by 200 nm Si buffer layer together with the multilayer coating.

5.2.2. Observation Techniques

A commercial AFM from Park Scientific was used to measure step heights, edge slopes, linewidths and film roughness. Features measured in this study were at least a few nanometers in size and can be clearly resolved by the instrument.

The scan direction is along the cross section of the lines, making it easier to measure changes in step heights and edge slopes. In order to eliminate possible differences in the vertical baseline between different line scans, all quantities were calculated from data obtained over individual line scans. The values for steps heights, edge slopes, linewidths and film roughness were then obtained by averaging over the line scans in the region of interest.

The samples were prepared for cross-sectional TEM observation by the standard process of mechanical thinning followed by ion milling. High resolution TEM observations were performed by Tai D. Nguyen, with a JEOL JEM 200 CX microscope operating at 200 kV.

5.3. Defect Coverage Profile

AFM measurements were performed on samples with nickel lines 0.15 μm wide and nominally 30 nm thick, before and after film deposition to study changes in step heights, edge slopes and line widths caused by the multilayer coating deposition process. Since there are differences among the lines on the samples, only the tip area of a marked line on each sample was observed in order obtain meaningful results (see figure 5.1 for measured areas). Due to some non-uniformity in the electroplating process, the lines had 70 nm high raised features at their ends. These extra features were useful for observing how the film coverage profiles vary for different initial step heights. The results for samples with and without the 200 nm buffer layer are tabulated in table 1 . The AFM images of the features themselves are in figure 5.2 and 5.3.

Table 1. Changes in step heights, edge slopes and linewidths of 0.15 μm wide, ~ 30 nm high features due to the multilayer film deposition process is tabulated. Each value is an average over ten line scans with indicated standard deviation.

Without 200 nm Si buffer layer						
	Before deposition		After deposition			
	Average	Std	Average	Std	Δ	
Line						
Step height (nm)	33.5	2.5	18.1	0.8	-12.9	(46%)
Edge slope (deg.)	60.4	1.1	12.6	0.7	-47.8	(83%)
End plateau						
Step height (nm)	73.2	18	55.7	3.8	-17.4	(24%)
Edge slope (deg.)	63.2	4.4	28.5	4.1	-37.7	(60%)
With 200 nm Si buffer layer						
	Before deposition		After deposition			
	Average	Std	Average	Std	Δ	
Line						
step height (nm)	27.9	1.8	15.0	0.9	-12.9	(46%)
edge slope (deg.)	53.1	3.7	9.0	0.7	-47.8	(83%)
End plateau						
step height (nm)	59.5	7.5	25.5	1.1	-33.9	(57%)
edge slope (deg.)	57.7	5.6	13.0	1.2	-44.7	(77%)

Figure 5.2(a) and 5.2(b) show the profile of one end of a 0.15 μm wide nickel line before and after multilayer coating deposition, without the buffer layer. The higher end plateaus on both figures are the ends of the line. The steps in the x-direction in figure 5.2(b) around 300 nm and 350 nm are artifacts resulting from glitches in the AFM's probe movement. Figure 5.3(a) and 5.3(b) show a 0.15 μm wide nickel line before and after multilayer coating deposition. This sample was coated with a 200 nm Si buffer layer in addition to the 40 bilayers of Mo/Si.

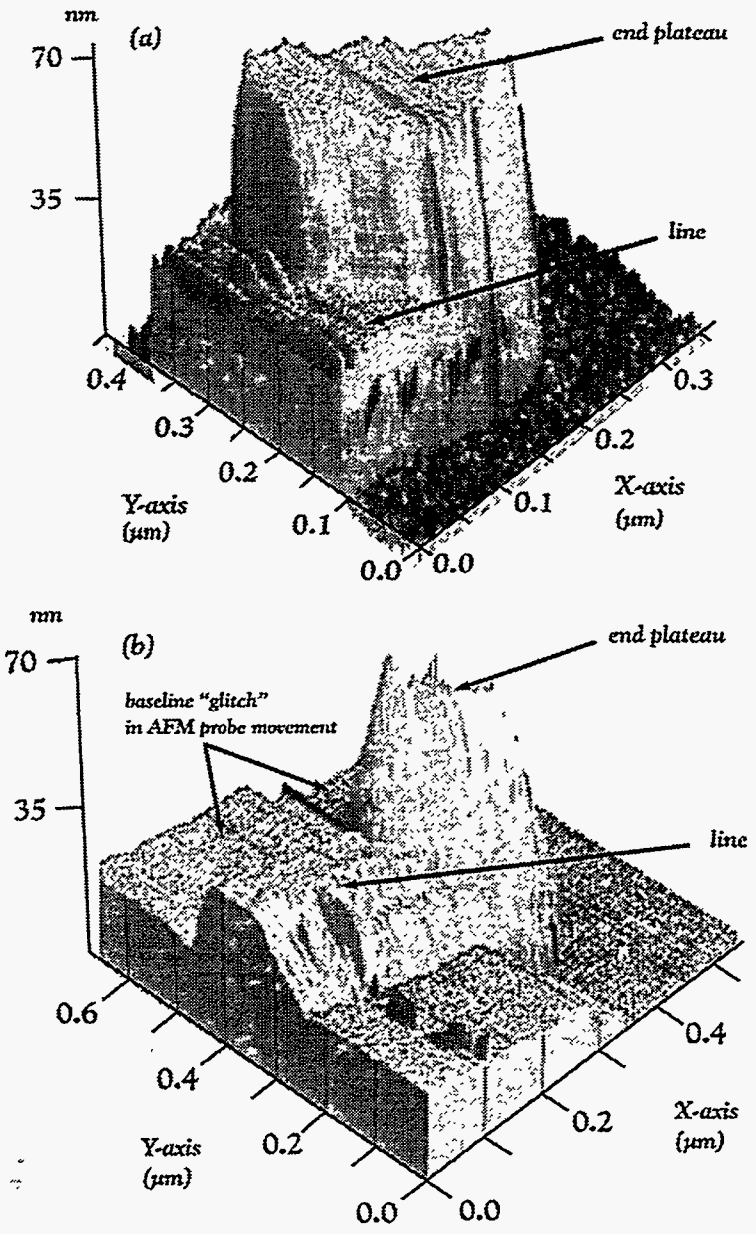

Figure 5.2. AFM image of electroplated 0.15 μm lines showing the 70 nm high raised end plateau and 30 nm high nickel lines, (a) before deposition, (b) after deposition without buffer layer. The deposited coating consisted of 40 bilayers of Mo/Si with d-spacing of 7 nm, resulting in a total coating thickness of 280 nm. Changes in the baseline along the X-axis in (b) is a measurement artifact due to glitches in AFM tip movements.

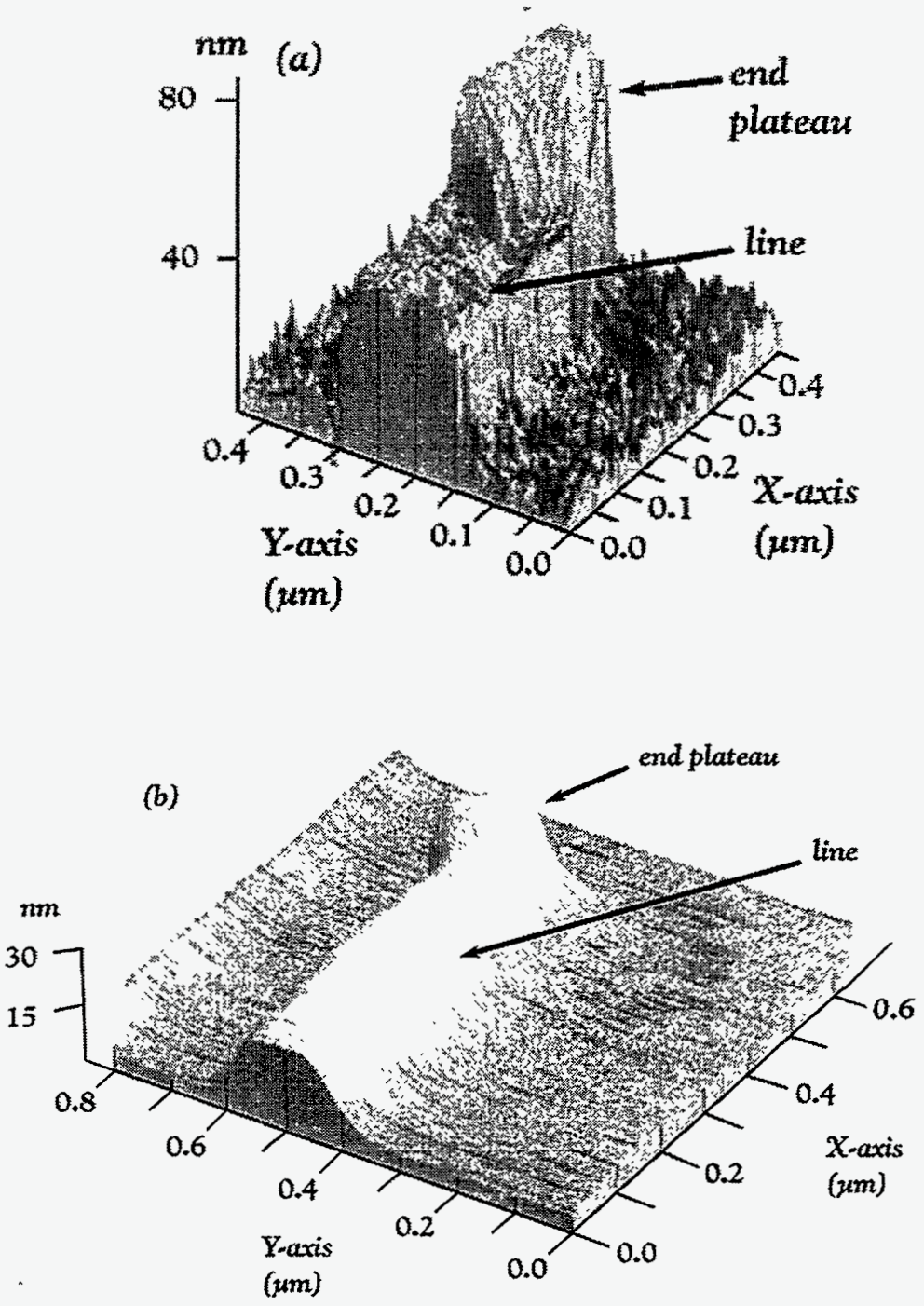

Figure 5.3. AFM image of electroplated 0.15 μm lines, (a) before coating deposition, (b) after coating deposition, with 200 nm Si buffer layer. The deposited film consisted of 200 nm Si buffer layer and 40 bilayers of Mo/Si with d-spacing of 7 nm, resulting in total film thickness of 480 nm.

Significant reductions in step heights were observed after multilayer coating deposition for both samples. *Without the buffer layer*, the height for the line (as opposed to the end plateau) decreased from *33.4 nm to 18 nm* (15 nm decrease). The height for the end plateau decreased from *73.1 nm to 55.7 nm* (17.4 nm decrease). The above values for step heights were averaged over ten line scans with the standard deviation shown in table 1.

With the 200 nm buffer layer, similar reductions in step heights were observed. The height of the line was reduced from *27.9 nm to 15 nm* (13 nm decrease), and the height of the end plateau was reduced from *59.4 nm to 25.5 nm* (33.9 nm decrease). On the sample coated with the buffer layer, the reduction in the step height was much larger for the end plateau compared to the rest of the line, 33.9 nm compared to 13 nm.

The measured step height reduction implies lower effective deposition rate over the defect, and that the multilayer stack is thinner over the defective area. It is possible that surface mobility of the sputtered-deposited atoms is affected by defect topography, that while their diffusion onto the defect is obstructed by the step, diffusion off the defect is not.

Changes in edge slopes were also measured for both samples. The data show that thicker deposited film resulted in greater edge slope reduction. On the sample *without the buffer layer* (figure 5.2(a) and 5.2(b)), the edge slope decreased from 60° to 12.5° for the line, and from 63° to 28° for the end plateau. The angle of ~ 60° corresponds to the maximum measurable edge slope for the AFM tip used in this experiment.

On the sample *with the 200 nm Si buffer layer* (figure 5.3(a) and 5.3(b)), edge slopes decreased from 53° to 8° for the line and from 57° to 13° for the end plateau. With and without the buffer layer, the edge slope reduction for the end plateau is less than that for the line. For both the line and the end plateau, the addition of the buffer layer resulted in additional edge slope reduction.

For the line, the addition of the buffer layer resulted in a small additional reduction in the edge slope, from 12.5° to 8°. For the end plateau, however, the addition of the buffer layer reduced the edge slope from 28° to 13°. This suggests that the reduction in the edge slope progresses more rapidly at steeper angles.

Linewidths on the sample with the 200 nm Si buffer layer were measured in terms of two quantities, the full-width half-maximum (fwhm) linewidth and the "extent" of the line. The "extent" of the line is the width of the line beyond which no further disturbance of the topography can be measured. Table 2 shows that while the fwhm linewidth stayed nearly constant before and after coating deposition, the "extent" of the line increased from 176 nm to 300 nm. This linewidth measurement is consistent with the measurements for step height and edge slope. Recalling that after film deposition with the buffer layer, the step height was reduced from 30 nm to 15 nm and edge slope was reduced to 9°. This corresponds to a spreading of 95 nm on each edge, thus the expected linewidth would be 365 nm, compared to the measured linewidth of 300 nm.

Table 2. Changes in linewidth due to coating deposition. The deposited coating consisted of a 200 nm Si buffer layer and a 40-bilayer Mo/Si coating with d-spacing of 7 nm.

		Before deposition		After deposition	
		fwhm	extent	fwhm	extent
linewidth	(nm)	164.6	176.6	151.0	297.0
stand. dev	(nm)	5.9	14.0	3.1	8.0

Transmission electron microscopy (TEM) was used to observe the profiles of multilayer coatings deposited over gold steps of heights ranging from 2 nm to 15 nm. Figure 5.4(a) shows a cross-sectional TEM image of a 40-bilayer, 7 nm-period Mo/Si multilayer coating deposited above a 8 nm evaporated gold step on a Si substrate. It shows the edge slope decreasing gradually with each subsequent deposited layer. This result is consistent with the data obtained with the AFM. Figure 5.4(b) is a plot of edge slope angle versus the number of Mo/Si layer pair deposited on the 8 nm step as taken from figure 5.4(a). A rapid reduction of edge slope was observed between the *12th and 22nd* bilayers, from *50° to 15°*.

Figure 5.5(a) and 5.5(b) are additional TEM cross-sectional images of step coverage profiles. Figure 5.5(a) shows the profile for 40 bilayers of Mo/Si with 7 nm-period deposited above a *20 nm gold step*. The white region at the edge of step is an undercut that occurred during the lift-off process. The lateral spreading of the defect and

distortion of the multilayer coating structure can be seen. Figure 5.5(b) shows the profile for 40 bilayers of Mo/Si with 7 nm-period deposited over a *4 nm gold step*. There is no edge undercut in this case and little lateral spreading of defect profile or distortion of multilayer structure can be observed.

Based on data from the AFM and TEM observations, the evolution of the profiles of multilayer coatings deposited over programmed defects can be divided into three stages. The first stage is characterized by significant disturbance of the multilayer structures, the second by rapid reduction in step heights and edge slopes, and the third by much slower changes in both edge slopes and step heights.

The first stage can be observed in the first five to seven layers in figure 5.4(a). Much disturbance of the multilayer structure occurred and discontinuity in the coating profile can be seen. The magnitude of the disturbance depends on the profile of the defect, the amount of edge undercut and the step height. These dependencies can be qualitatively observed in figure 5.5.

In the second stage, the layered structure is reestablished at the edge and the profile rapidly approach the characteristic profile of the deposition process. For the sputter-deposited coatings studied, the profiles were characterized by edge slopes of *10° to 15°*. Rapid changes in the step height and the edge slope occur with each subsequent layer deposition during this stage. In figure 5.4(a), this can be seen between the 12^{th} and 22^{nd} bilayers.

In the third stage, step heights and edge slopes reduction continued, but at a much slower rate. This can be observed by comparing the changes in step height and edge slope for the 30 nm line regions, with and without the 200 nm Si buffer layer. Little differences in step height and edge slope reduction were observed by the addition of the buffer layer, consistent with a feature that has reached its characteristic profile.

The AFM images in figure 5.2 and 5.3 and the linewidths extracted from them (table 2) show that the lateral spreading of defects with 0.15 μm dimensions are not strongly dependent on the initial defect heights at film thicknesses of 500 nm or less and defect thicknesses of 70 nm or less. This is demonstrated by the fact that the 70 nm end plateaus and the 30 nm lines resulted in nearly equal lateral spreads.

There was not enough data to extend this finding to larger defects and thicker film. If differential mobility due to topography was the mechanism responsible for the observed step height reductions, then the magnitude of the reductions would decrease with increased defect size, and thicker defects with sufficiently large lateral dimensions would result in larger lateral spreading. In addition, the results obtained here showed that step height and edge slope reductions slow down when defect edge slopes of ~10° were reached. It was also found that this characteristic edge slope was more quickly reached with thinner defects, and once the defect has reached its characteristic profile, additional layers cause little change to it. As a result, additional deposited layers of materials affect the profiles of thicker defects more strongly than the profiles of thinner defects. Thus, thicker films than were deposited here may result in more lateral spreading for thicker defects.

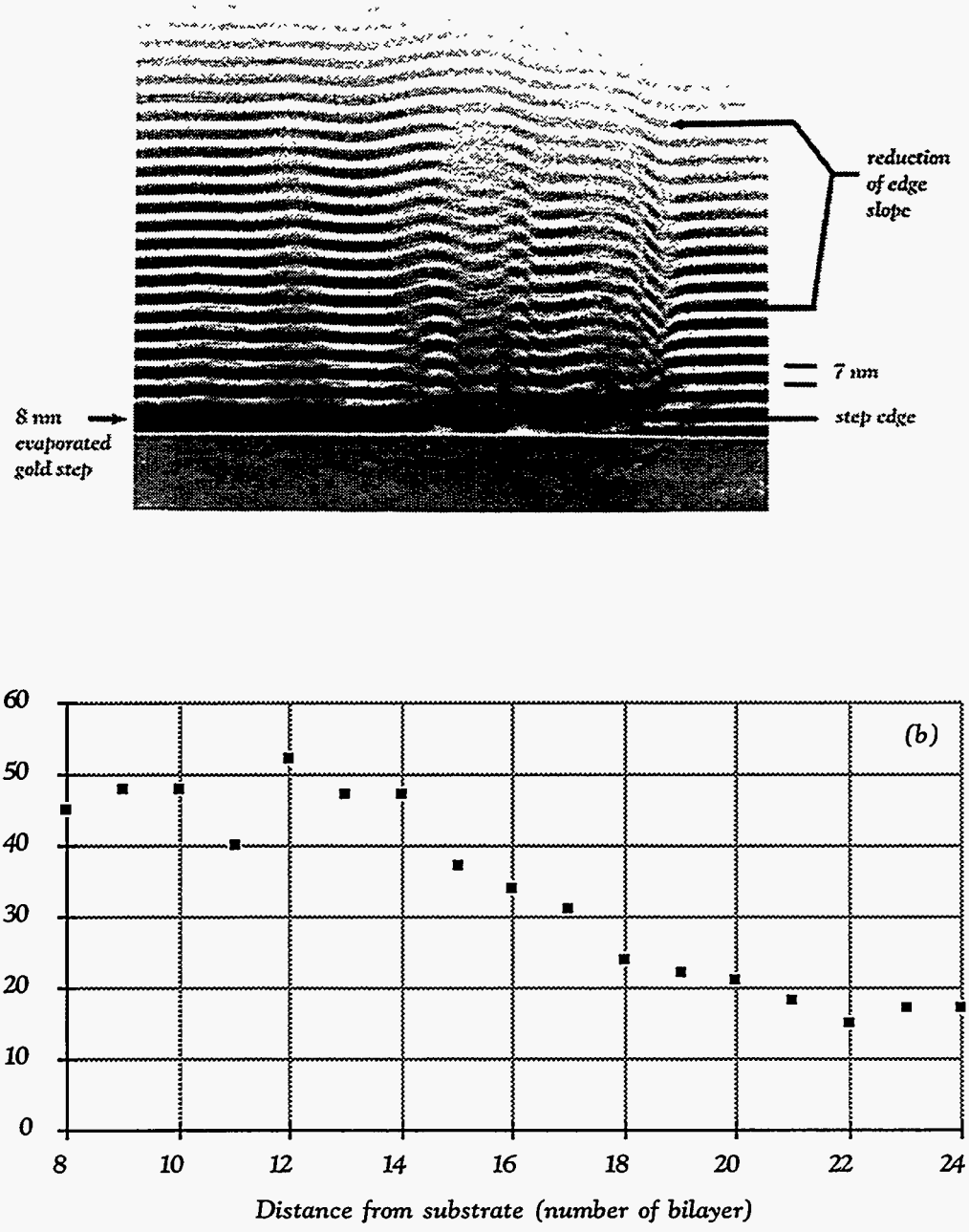

Figure 5.4. TEM images of cross section of sample, showing the defect and the 40 bilayer, 7 nm-period, Mo/Si multilayer coating above it, (a) a multilayer coating deposited above an 8 nm evaporated gold step, (b) the edge slope vs. the number of bilayer deposited on an 8 nm evaporated gold step. Data was taken from (a).

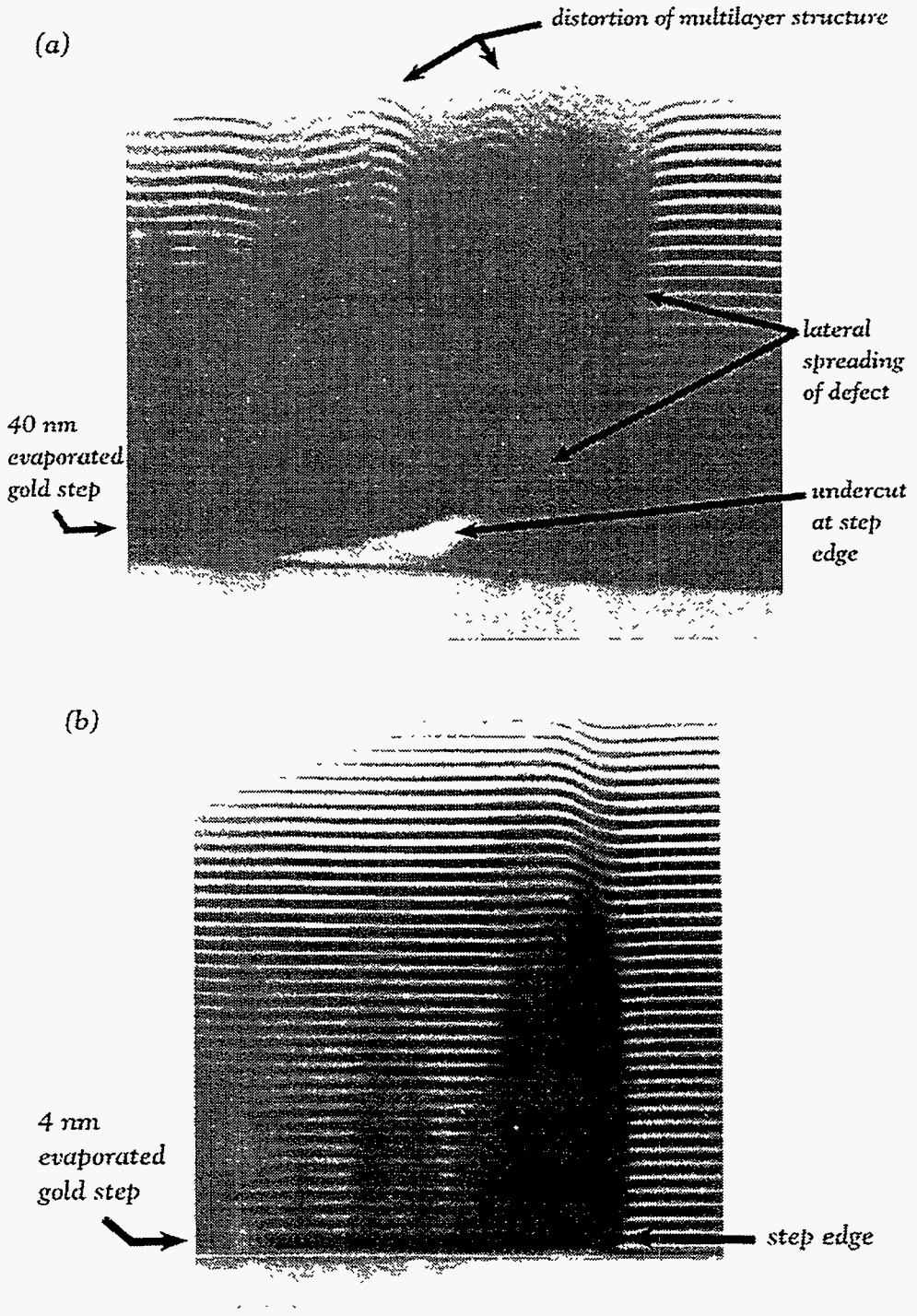

Figure 5.5. TEM cross-sectional images of 40 bilayers of Mo/Si multilayer coatings with 7 nm d-spacing deposited over gold steps. (a) The gold step is 40 nm high, deposited by evaporation and lift-off. Undercut results in lateral spreading and distortion of multilayer structure. (b) The gold step is 4 nm high with no undercut. Little lateral spreading and distortion of multilayer structure is observed.

5.4. Roughness propagation

Two samples with 2 μm lines of ~ 20 nm thick evaporated gold coated with 40 bilayers of 7 nm-period Mo/Si multilayer coatings were examined to study how roughness propagates with the deposited film. One sample was coated with an additional 200 nm Si buffer layer (see figure 5.1). The roughness of the gold lines and the Si substrates were measured, with an AFM, for both samples before and after multilayer coating deposition. Results of the roughness measurements are tabulated on Table 3. A large standard deviation implies the presence of large features on the film. The AFM images of the two samples before and after coating deposition are shown in figure 5.6, for the sample without a buffer layer, and in figure 5.7, for the sample with a 200 nm Si buffer layer. All figures show edges of the 2 μm lines.

Table 3. Roughness over different areas of sample before and after multilayer film deposition. The multilayer coating consisted of 40 bilayers of 7 nm-period Mo/Si. The buffer layer is 200 nm of Si.

	Before deposition		After deposition	
	On wafer	On Au film	On wafer	On Au film
Without 200 nm Si buffer layer				
RMS roughness (nm)	0.31	3.43	0.32	1.75
standard deviation (nm)	0.13	0.87	0.12	0.95
With 200 nm Si buffer layer				
RMS roughness (nm)	0.22	3.27	0.7	0.84
standard deviation (nm)	0.06	0.84	0.14	0.16

Figure 5.6(a) shows the edge of the gold line before deposition, and figure 5.6(b) shows the same edge after 40 bilayers of 7 nm-period Mo/Si was deposited. The large arrows point to two distinguishing features that can be seen before coating deposition. Similarly, figures 5.7(a) shows an edge before deposition, and 5.7(b) shows the same edge after the 200 nm Si buffer and 40 bilayers of Mo/Si was deposited.

Of the two features marked by arrows in figure 5.6(a), one is 5 nm deep and 70 nm long, and the other is 5 nm deep and 30 nm long. Both were significantly smoothed over after coating deposition. The smaller granular features on top of the evaporated film were similarly smoothed out (figure 5.6(b)). Table 3 shows that roughness over the gold film was reduced from 3.4 nm rms to 1.7 nm rms by coating deposition while roughness over the Si substrate stayed nearly constant at 0.3 nm rms.

Further smoothing of the evaporated film occurred when an additional 200 nm Si buffer layer was deposited prior to multilayer coating deposition. Figure 5.7(a) and 5.7(b) show that features along the edge of the line were smoothed out, and so were the small granular features on the evaporated gold film. Roughness over the gold film decreased from 3.2 nm to 0.8 nm, a larger reduction in roughness compared to that obtained for the sample without the buffer layer (Table 3). However, roughness of over the Si substrate *increased* from 0.2 nm to 0.7 nm. Roughness of this magnitude can significantly affect the reflectivity of multilayer reflective coatings deposited above it. In this case, the measured reflectivity of the multilayer coating deposited without a buffer layer was 61.7% compared to 43% for one deposited above the buffer layer.

This increase in substrate roughness is likely to be due to the 200 nm thick Si buffer layer, for no increase in substrate roughness was observed when only the Mo/Si coating was deposited. This result is similar to the increased in the roughness observed in amorphous W/C multilayer coatings and crystalline W film with increased film thickness [4]. It is also consistent with results from a study by Savage et al. which found that interfacial roughness between layers in a W/C multilayer increased with multilayer period [5].

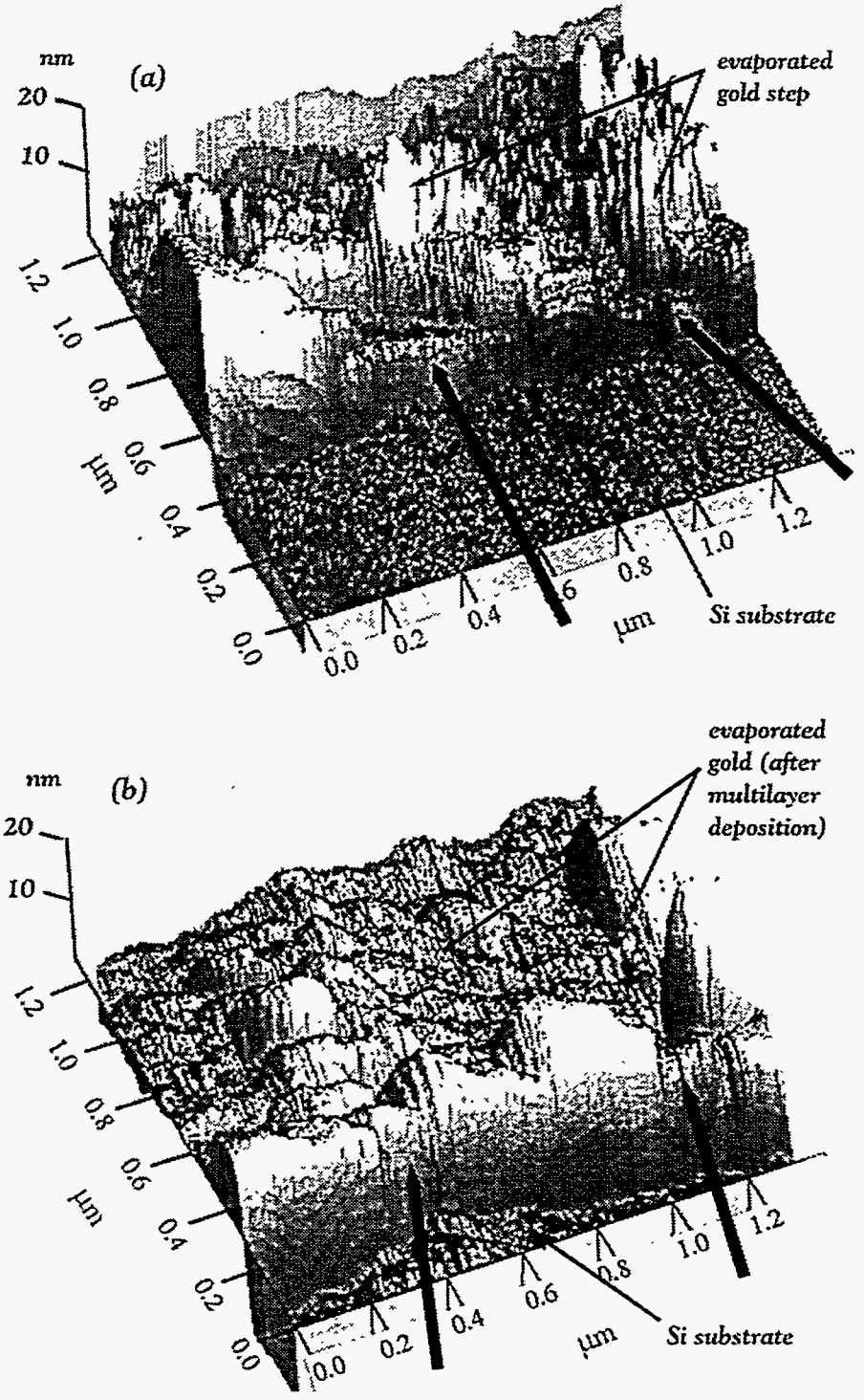

Figure 5.6. AFM image of an edge of a 20 nm high evaporated gold step showing roughness propagation with 40 bilayers of Mo/Si, without the buffer layer, (a) before coating deposition and (b) after coating deposition. Roughness of the gold film decreased from 3.4 nm rms to 1.7 nm rms after Mo/Si deposition. The large arrows point to two features easily seen prior to coating deposition, one 5 nm deep and 70 nm long and the other 5 nm deep and 30 nm long. Both were significantly smoothed out after deposition.

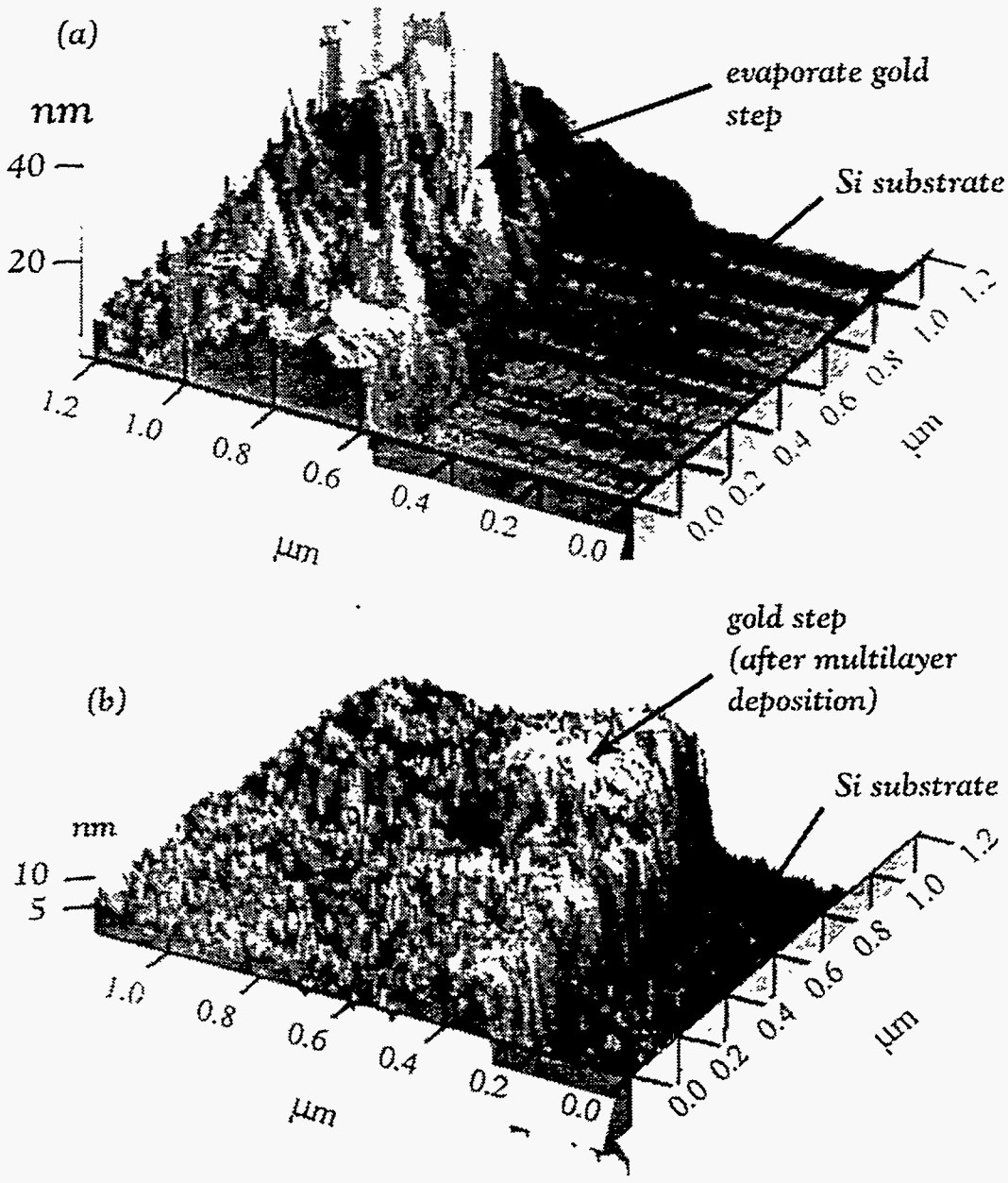

Figure 5.7. AFM image of an edge of a 20 nm evaporated gold step before and after coating deposition. Deposited coatings consist of 200 nm Si buffer layer and 40 bilayer, 7 nm-period Mo/Si multilayer, (a) before Mo/Si deposition and (b) after Mo/Si deposition. Roughness of the gold film decreases from 3.2 nm rms to 0.8 nm rms. However, roughness of Si substrate *increases* from 0.2 nm rms to 0.7 rms. (Vertical baseline not calibrated)

Figure 5.8 shows a TEM cross-sectional image of a 7-nm-period Mo/Si multilayer coating deposited above a 4 nm evaporated gold film. The first layer deposited over the gold film is Mo, a high-Z element. As a result, the boundary between gold and Mo is somewhat difficult to distinguish. Arrows indicate features on the gold film and their smoothing by the deposited coating. This figure provides a qualitative picture of the evolution of roughness in Mo/Si multilayer coatings.

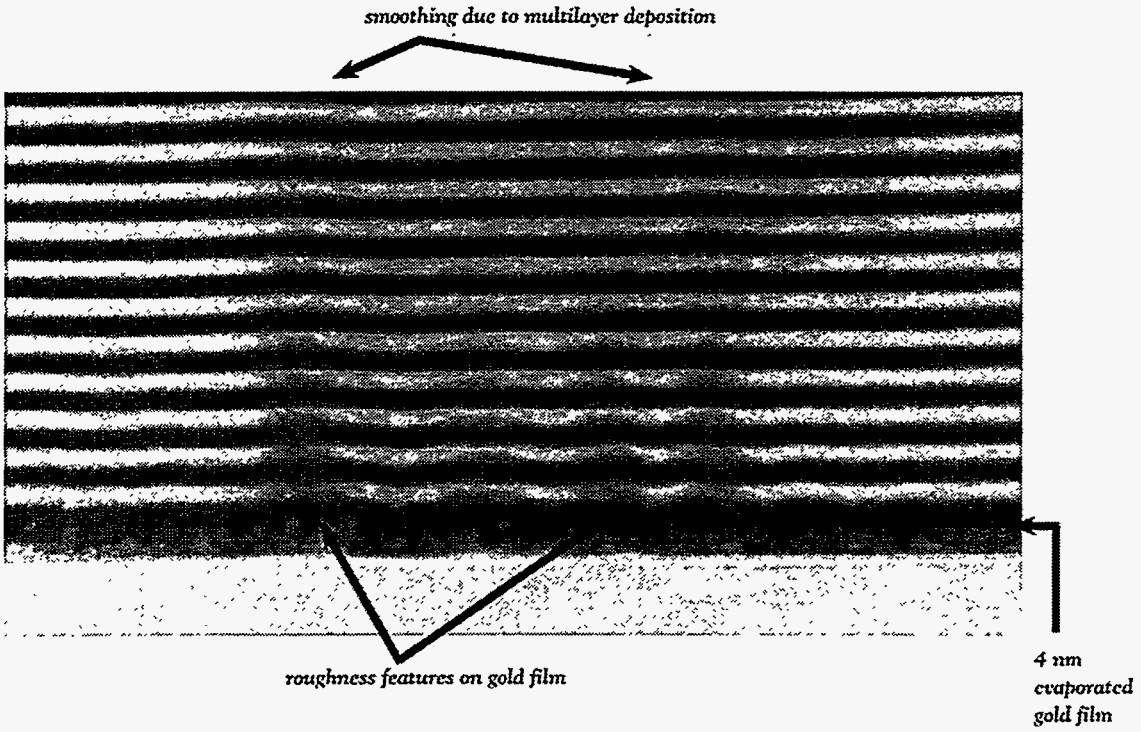

Figure 5.8. TEM cross-sectional image of a 7 nm Mo/Si multilayer coating deposited above a 4 nm evaporated gold film. The first layer deposited over the gold film is Mo, a high-z element. As a result, the boundary between gold and Mo is difficult to distinguish. Arrows indicate features on the gold film and their subsequent smoothing by the deposited film.

5.5. Conclusion

Observations with an AFM of features of 20 nm, 30 nm and 70 nm heights covered by Mo/Si coating show that step heights and edge slopes of 0.15 μm wide programmed defect lines were significantly reduced after multilayer coating depositions. These effects

were confirmed by TEM images of coatings deposited over gold steps of similar heights. The evolution of coverage profile over features as a function of deposited coating thickness can be divided into three stages. The first stage is characterized by much disturbance of the multilayer structure and disruption of the layered structure, the second by reestablishing continuity of the layers and by rapid reduction in edge slope and step height to a characteristic edge slope, and the third by continuing but much slower reduction in step height and edge slope with subsequently deposited layers.

The characteristic edge slope for sputtered-deposited coatings studied here was ~ 10° to 15°. Assuming no step height reduction, lateral spreading of substrate defect can be estimated to be defect thickness divided by the tangent of the characteristic edge slope angle. Step height reduction reduces the lateral spreading of the defect while the presence of undercut at the defect's edge increases it.

The addition of a 200 nm Si buffer layer before depositing the multilayer coating further reduces edge slopes and rms roughness in the area over the rough features (30 nm rms roughness). However, the buffer layer also increases roughness for the smooth substrate (0.3 nm rms roughness), thus reducing the maximum reflectivity of multilayer reflective coating deposited above it.

Reference

1. E.P. Stoll, "Picture processing and three-dimensional visualization of data from scanning tunneling and atomic force microscopy," IBM Journal of Research and Development, **35**(1), pages 67-77 (1991).

2. E. Meyer, "Atomic force microscopy," Progress in Surface Science, **41**(1), pages 3-49 (1992).

3. T.D. Nguyen, R. Gronsky, and J.B. Kortright, "Cross-sectional transmission electron microscopy of X-ray multilayer thin film structures," Journal of Electron Microscopy Technique, **19**, pages 473-485 (1991).

4. T.D. Nguyen, and J.B. Kortright, personal communications (1993).

5. D.E. Savage, N. Schimke, Y.-H. Phang, and M.G. Lagally, "Interfacial roughness correlation in multilayer films: influence of total film and individual layer thicknesses," Journal of Applied Physics, **71** (7), pages 3283-93 (1992).

Chapter 6

Imaging of Extreme Ultraviolet Lithographic Masks with Programmed Substrate Defects

6.1. Introduction

Electromagnetic simulations described in chapter 4 indicate that defects in the mask's multilayer reflective coating can severely degrade aerial images. These calculations show that the largest intensity reductions occur with substrate defects. In this chapter, results are reported from an imaging experiment conducted to verify the effect of substrate defects on the aerial images and to evaluate their printability. Printability studies provide an understanding of the magnitude of linewidth variations caused by the defects. Thus, they are useful for determining the requirements for defect inspection and repair. Many such studies have been conducted for optical lithography [1-17].

In this study, masks with programmed defects of controlled dimensions were imaged with an extreme ultraviolet imaging system operating at 14 nm. The imaging system was a 2–mirror-aspheric system belonging to the Nippon Telephone and Telegraph Corporation (NTT), installed on a bending magnet beamline at the Photon Factory in Tsukuba, Japan [18-21].

6.2. Experimental Conditions

6.2.1. Imaging Conditions

Figure 6.1 is a schematic of the beamline and the optical system used in this experiment. The illumination system consisted of 2 cylindrical mirrors and produced a ring-shape illuminated stripe on the mask. One of the mirrors was movable so as to scan the illuminated ring over the mask. A carbon filter was used to filter out wavelengths over 40 nm.

The reduction imaging system consisted of two aspherical mirrors, one concave and one convex, with matched radius of curvature of about 500 mm to provide a flat field. Mirror diameters were 150 mm for the concave mirror and 60 mm for the convex mirror. The distance between the two mirrors was ~ 400 mm. The distance between mask and wafer was ~ 700 mm. The numerical aperture of the system was ~ 0.1 and the reduction ratio was 5:1. The exposure area was ~ 2 mm by 0.6 mm on the wafer.

The incident angles on both masks and optics were ~ 2° off-normal. The required multilayer periods on all optical components were within a range of 0.2 Å. This makes it possible for all components to be coated in a single coating run, thus enabling precise matching of the reflection peaks [22]. The reflective coatings were 30 bilayers of Mo/Si with of 7.25 nm-period and a Mo-to-Si thickness ratio of 2/3, yielding reflection peaks centered at 14 nm.

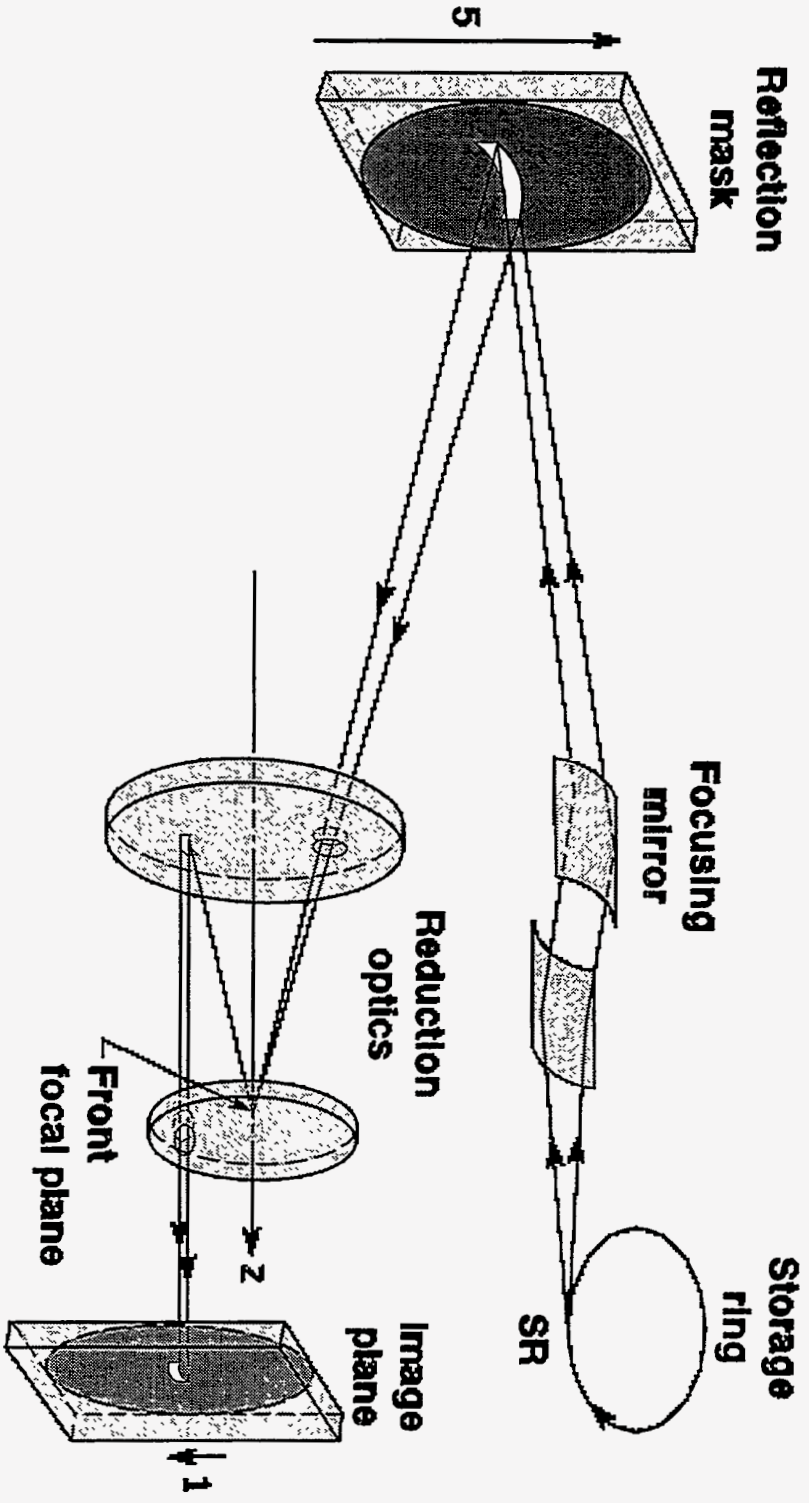

Figure 6.1. Schematic of the imaging system, showing the cylindrical condenser optics, reflective mask and aspherical imaging optics.

Imaging was performed under vacuum. The mask was manually placed in the illuminated area prior to pump-down. The shutter timer and the wafer stage were both computer–controlled so that a series of exposures with different exposure times and focusing conditions could be completely automated. The exposure samples were inserted into the exposure chamber via a load-lock, thus reducing pump-down time.

The imaging system, designed for 0.1 μm resolution, has demonstrated 0.15 μm resolution for lines-and-spaces [21]. The achievable resolution was limited by the surface figure errors on the mirrors and potential assembly errors. Surface figure errors were 3.4 nm rms (29.7 nm peak-to-valley) for the larger concave mirror and 1.8 nm rms (17 nm peak-to-valley) for the convex mirror. Unfortunately, the system was not working at its optimum capability during the period when this experiment was performed. The finest printed lines were 0.6 μm, much larger than had been previously demonstrated. The degraded performance was likely to be a result of misalignments of the mirrors that could have happened at some point during transport, mounting or operation. However, even with the degraded resolution, the effects of the substrate defects were observable.

6.2.1. Mask Fabrication

Figure 6.2 illustrates the fabrication process for masks with programmed substrate defects. The mask used in this experiment consisted of absorber line-and-spaces and contained programmed defects made up of 25 nm thick gold. The multilayer reflective coating was 30 bilayers of Mo/Si with of 7.25 nm-period and was deposited by planar magnetron sputtering at the Center for X-ray Optics at Lawrence Berkeley Laboratory. The deposition process was described in more detail in chapter 1 and 3.

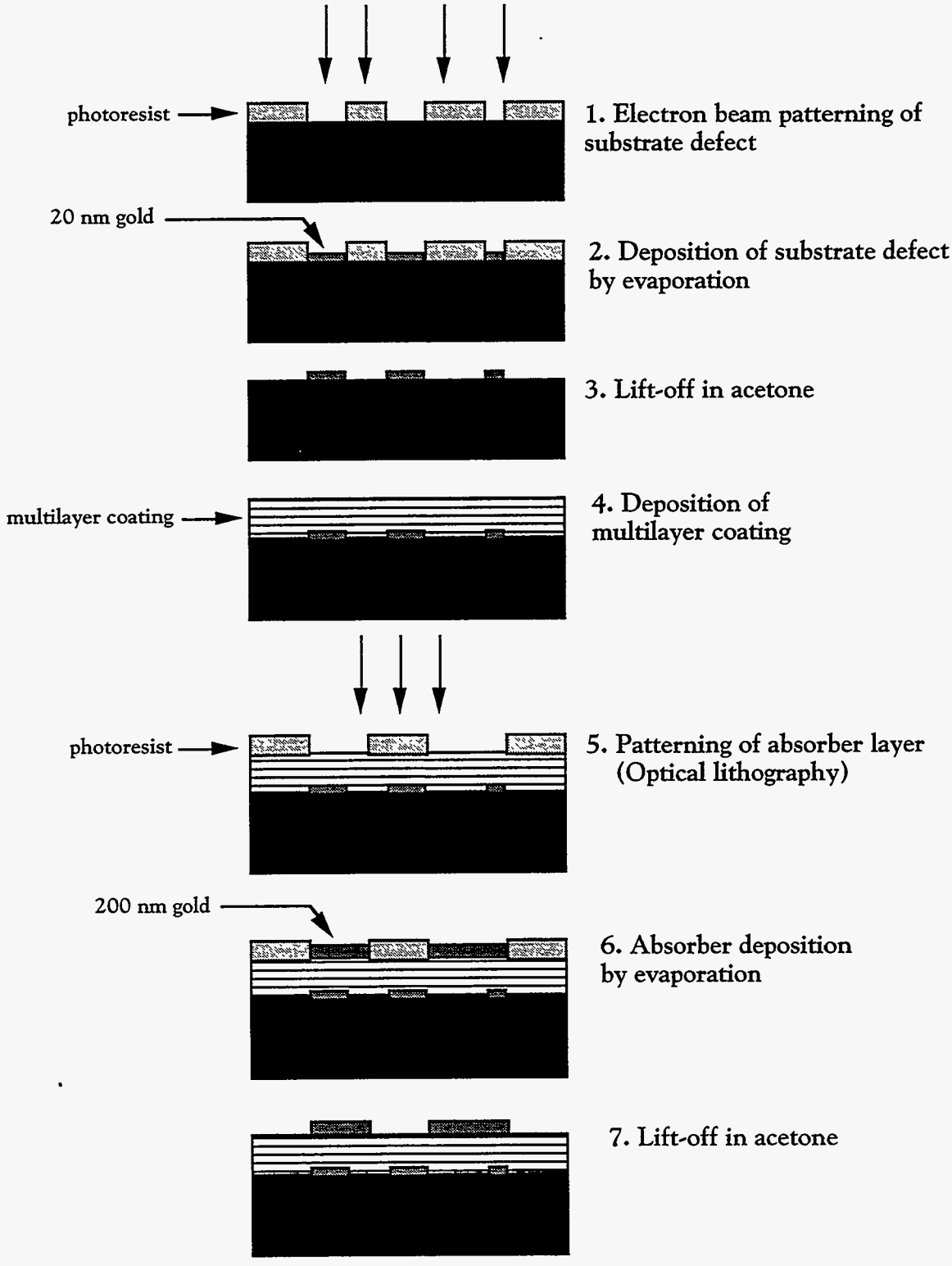

Figure 6.2. Fabrication process for mask with programmed defect.

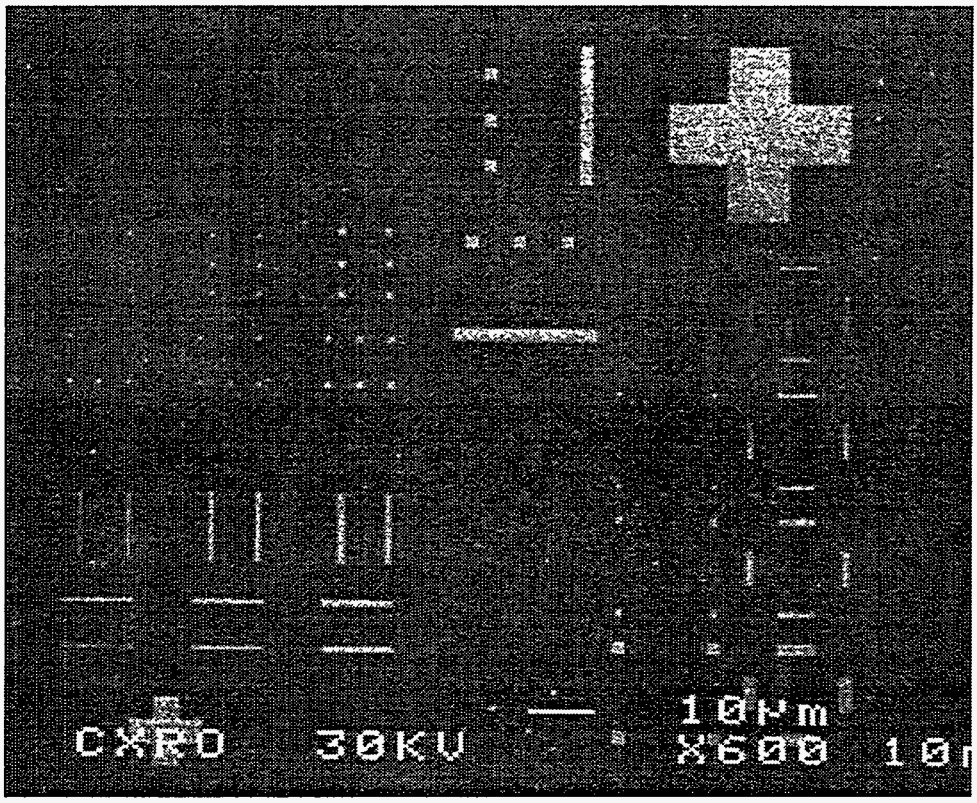

Figure 6.3. Defect patterns after lift-off and before multilayer coating deposition, i.e. after step 3 in figure 6.2.

Evaporation and lift-off were used to deposit the programmed defects. The defect pattern, shown in figure 6.3, consisted of lines, dots and large crosses for alignment. The pattern was written onto a 150 x 150 μm area on the mask using a converted JEOL SEM at the Center for X-ray Optics/LBL. Since the NTT imaging system has a 5:1 reduction factor and had demonstrated 0.2 μm resolution, the smallest defects were 0.2 x 0.2 μm squares as *measured on the mask*, or 1/5 of the expected minimum resolvable feature size. Other defects included squares of 0.5 μm, 1 μm and 2 μm dimensions and horizontal and vertical line defects with widths of 0.2 μm, 0.5 μm, 1 μm and 2 μm. Two alignment crosses, one measured 30 x 30 μm and the other 15 x 15 μm, were also patterned and were used to help in locating the defect field after printing.

The absorber pattern consisted of lines-and-spaces of 150 nm thick evaporated gold. Absorber thicknesses were measured with an atomic force microscope (AFM). Since

the available e-beam writer did not have an alignment capability, absorber patterning was done with g-line lithography and lift-off using the process described in chapter 2. Absorber patterns ranged from 10 μm wide lines-and-spaces to 1 μm wide lines-and-spaces that translated to 2 μm to 0.2 μm lines-and-spaces on the wafer when printed with the NTT 5:1 imaging system.

Figure 6.4(a) is an image of the mask with 25 nm thick defects, taken with an optical phase contrast microscope. The dimensions of the relevant absorber and defect features as measured *on the mask* are indicated. Some of the lines are numbered for easy reference to other figures. The absorber defect on the lower left corner and the 30 x 30 μm cross on the upper right corner are useful for orientation purposes. Figure 6.4(b) shows a SEM image of the same area. The substrate defects were difficult to observe under SEM since there is no contrast mechanism for secondary electron emission, thus pointing out a challenge for defect inspection.

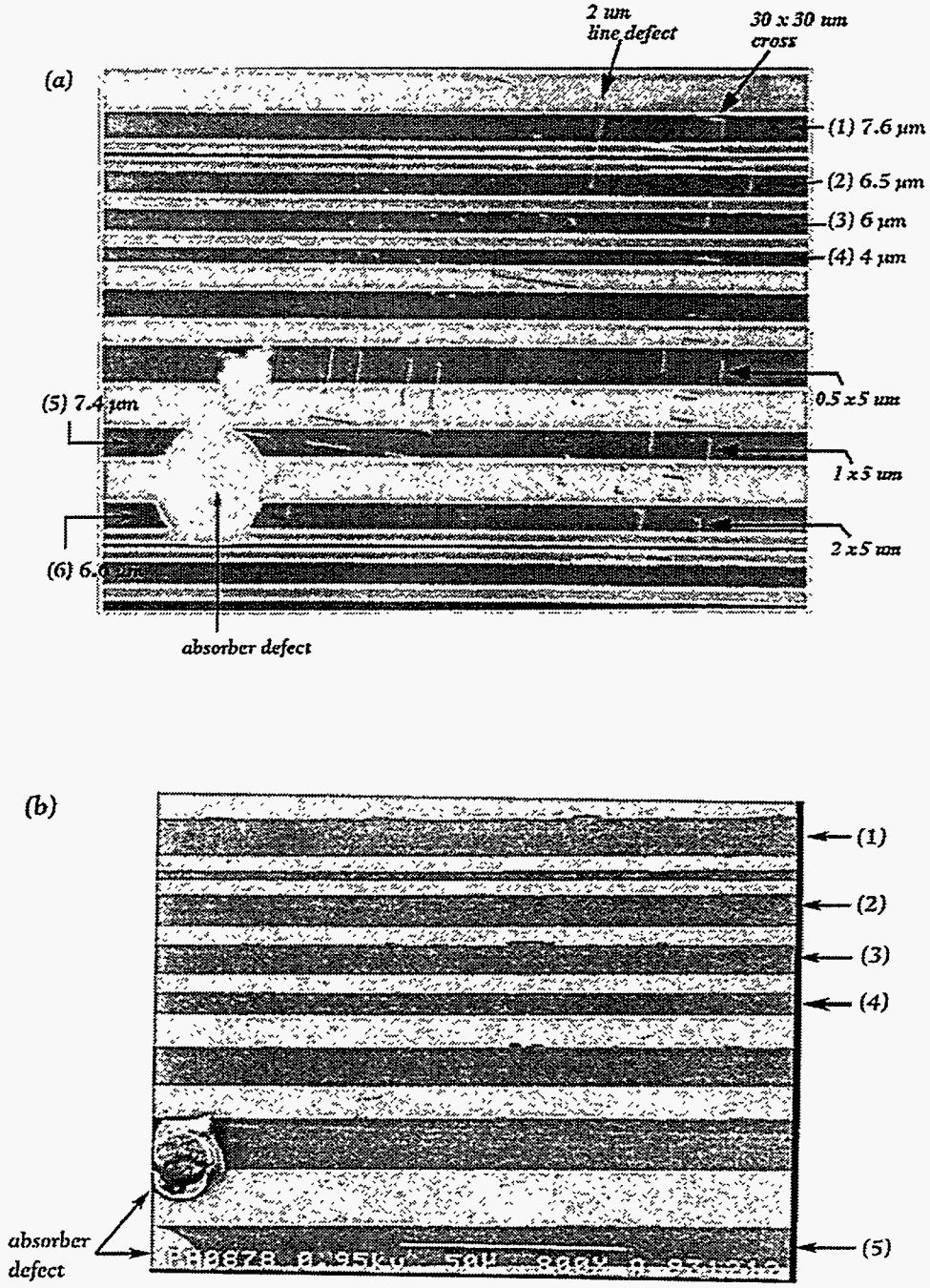

Figure 6.4. (a) Optical phase contrast microscope image of a completed mask, showing the 150 nm thick absorber lines in the foreground and the 25 nm thick programmed defects in the background. Dimensions of relevant defects and absorber features are indicated. Some of the lines are numbered for easy reference with other figures to follow. (b) a scanning electron microscope (SEM) image of the same area. The defects are more difficult to detect under SEM.

6.3. Imaging Results

The imaging experiment was performed over a period of two weeks in Tsukuba, Japan. Exposure doses were optimized for the printing of the smallest lines, 0.6 μm in this experiment. The photoresists were 80 nm thick PMMA and SAL 601. PMMA is a low contrast positive resist and SAL 601 is a high contrast chemically amplified negative resist.

6.3.1. Measurements of Samples

Initial observations of the optimized samples were performed with an SEM at the NTT facility in Atsugi, Japan. More detailed measurements of both masks and wafers were performed with an AFM at the Lawrence Berkeley Laboratory.

Figure 6.5(a) shows an SEM observation of the resist image of the mask with 25 nm thick defects printed in PMMA. The arrows point to the distortions in the resist lines caused by the defects (quoted sizes are as measured on the *mask*). In the upper right-hand corner of figure 6.5(a), the boxed area shows the effects of the large cross (30 μm x 30 μm *on the mask*). The lower arrows point to the variations in the resist lines caused by 2 x 5 μm defects. The numbered lines are images of lines with the same number on the mask (figure 6.4(a), 6.4(b)).

Figure 6.5(b) shows the resist image of the same mask printed in SAL 601, a negative high contrast chemically amplified resist [23, 24], taken with an atomic force microscope (AFM). The areas affected by 30 x 30 μm cross and the 2 x 5 μm defects are indicated.

A more detailed observation of the effect of the 30 x 30 μm cross is shown in figure 6.6. Figure 6.6(a) shows the cross and other defects in its vicinity, and figure 6.6(b) is an AFM image of the SAL 601 resist pattern in the area affected by the cross. Since SAL 601 is a negative resist, the clear regions are printed as resist lines. The effect of substrate defects can be seen on lines 1, 2, and 3. The defects reduced aerial image intensities, and thus reducing the resist linewidths in the affected areas. The linewidth of line 1, a 1.5 μm resist line, was reduced by ~ 20% by the 2 μm line

defect. The 2 μm square defects also caused observable linewidth variations in line 3, a 1.25 μm wide resist line. However, the effect of the three square defects, spaced 5 μm apart, cannot be resolved individually due to the reduced resolution of the imaging optics. As expected, the effect of the 30 x 30 μm cross can be easily observed. The aerial image intensity reductions resulted in near breaks in the resist lines, as can be clearly seen in lines 1, 2, and 3.

The effects of other defects can also be observed. Figure 6.7(a) is an optical microscope image of the 2 x 5 μm defects and their vicinity, and figure 6.7(b) is an AFM image of the SAL 601 resist pattern of the area. Lines 5 and 6 are 7.4 μm and 6.6 μm clear lines on the mask, which translated to 1.5 μm and 1.3 μm resist lines on the wafer. The 2 x 5 μm defects resulted in 15% linewidth variations in line 6. Linewidth variations caused by 1 x 5 μm defects can also be observed, but the effect of the defects cannot be resolved individually.

Nearby breaks in the absorber line provides an interesting comparison between substrate defects and absorber defects. Figure 6.8(a) is an SEM image of the region around the 30 x 30 μm cross, showing the nearby absorber defects. The absorber defects are between 2 μm and 5 μm in size and are 150 nm thick. The cross is 30 μm x 30 μm in size and is 15 nm thick. Due the differences in size, thickness and placement, no quantitative comparison can be made from this image alone. However, it is worth noting that the large cross is nearly invisible under SEM inspection while the absorber defect can be clearly seen. Their effects on the image, however, are comparable.

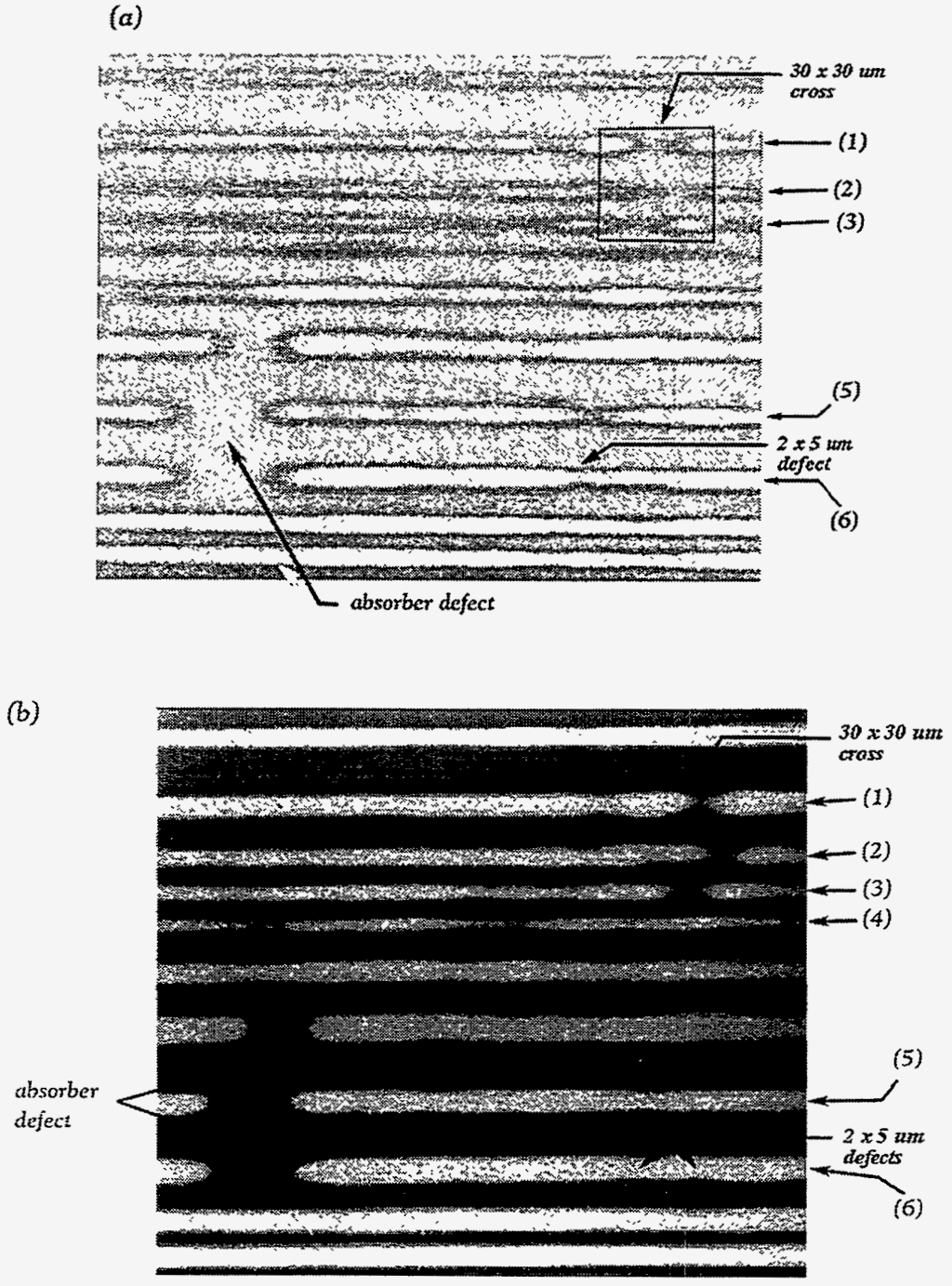

Figure. 6.5. SEM images of the entire programmed defect area for (a) PMMA resist and (b) SAL 601 resist. The areas affected by the substrate defects are indicated. Quoted defect sizes are as measured on the mask. The numbered lines correspond to the numbered lines in figure 6.4. These numbers will be used throughout this chapter.

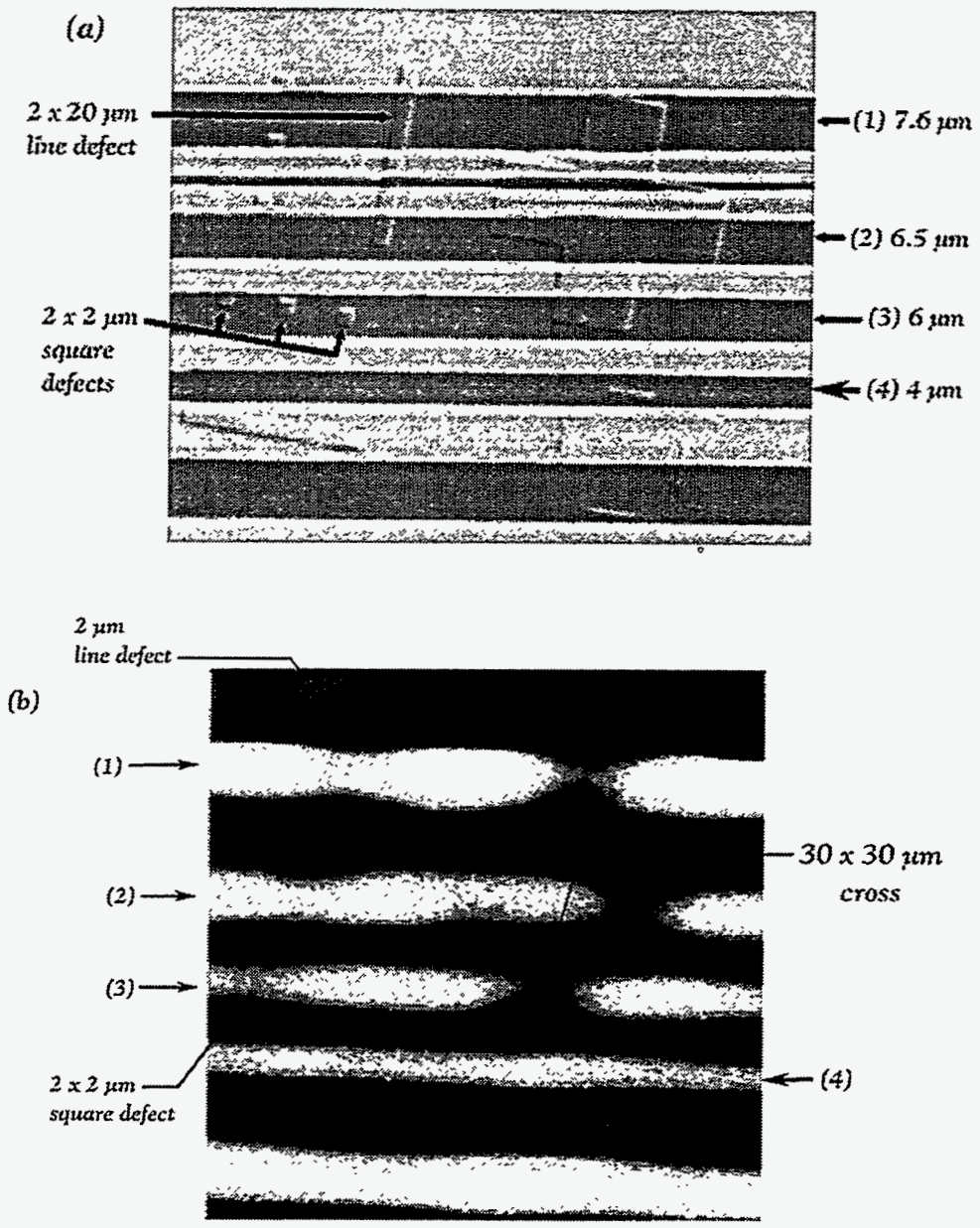

Figure 6.6. The 30 x 30 μm cross (a) on the mask (optical microscope image) and (b) its effect SAL 601 resist image (AFM image). The effect of the substrate defects are indicated. Quoted sizes are as measured on the mask. The numbered lines correspond to the numbered lines in figure 6.4. Line defect of 2 μm width caused 20% linewidth variation on line 1, a 1.5 μm wide resist line. Effects of 2 μm square defects can also be observed.

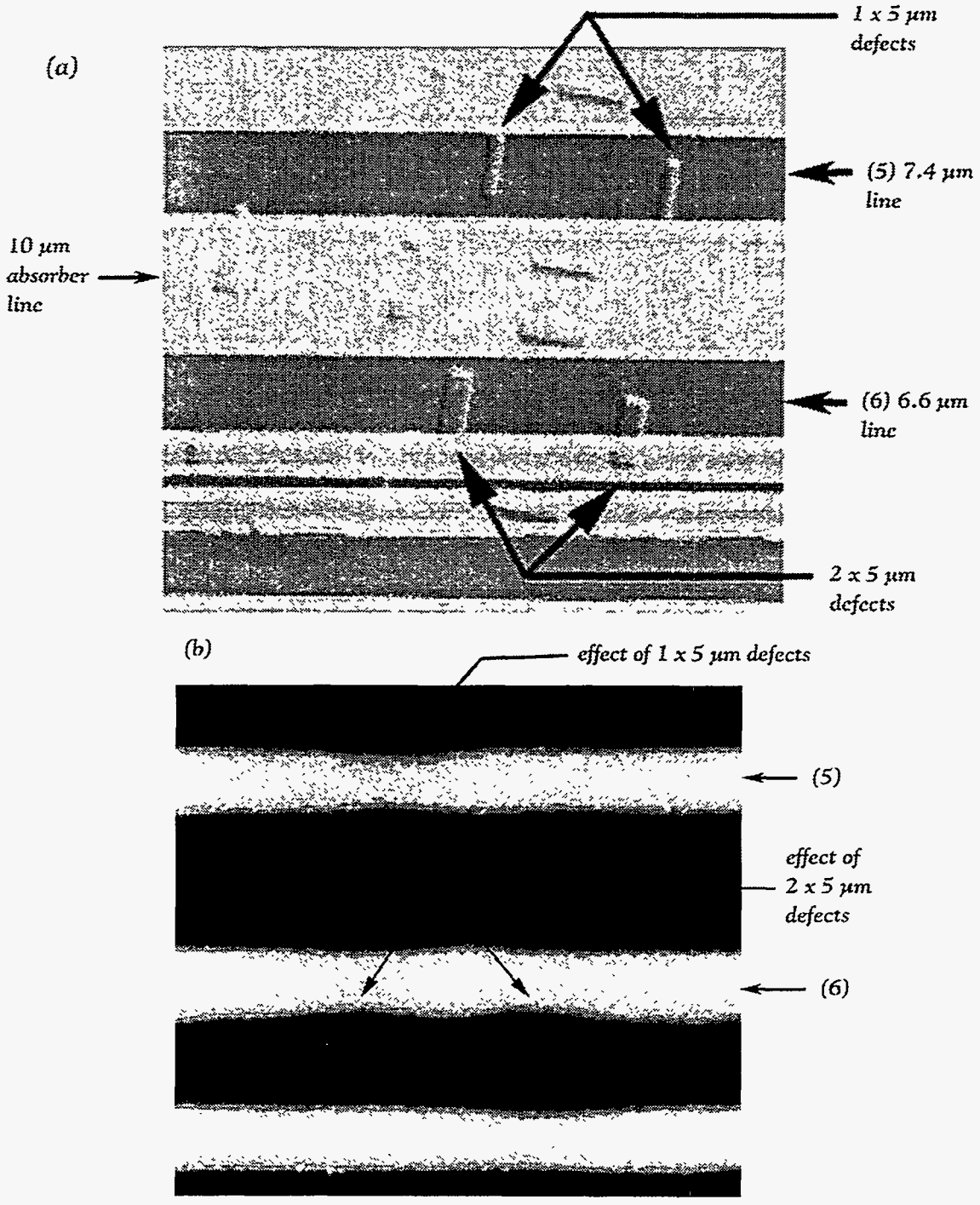

Figure 6.7. The effect of 2 x 5 μm and 1 x 5 μm defects on resist image. (a) Optical microscope image of the mask of showing two 2 x 5 μm defects in line 6 and two 1 x 5 μm defects in line 5. Defects are spaced 10 μm apart., (b) SAL 601 resist image (AFM) showing linewidth variations caused by defects. Indicated defect sizes are as measured on the mask. The 2 x 5 μm defects caused 15% linewidth reduction in a 1.3 μm resist line. The effect of 1 x 5 μm defects was also observable but was not individually resolved.

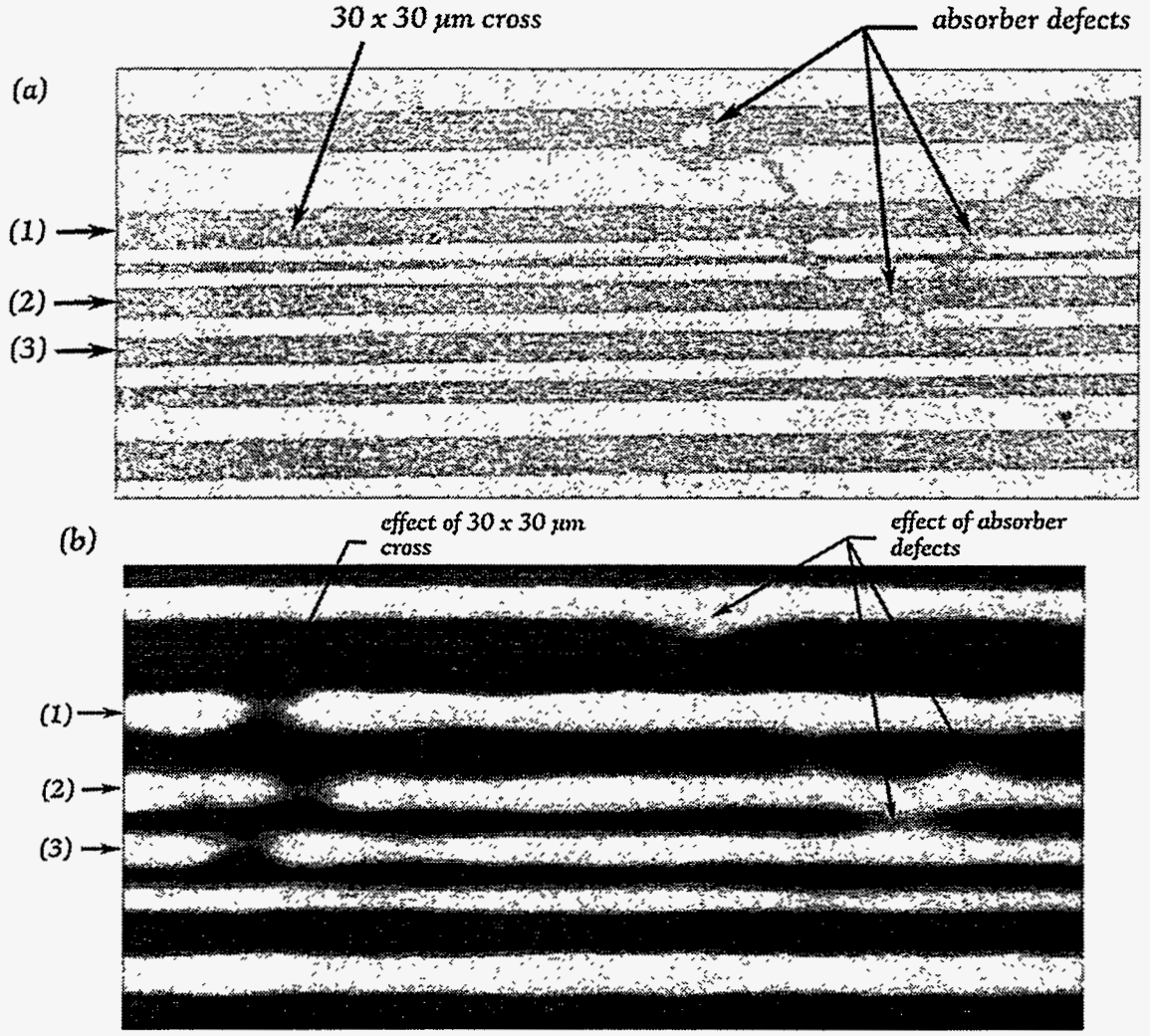

Figure 6.8. An observation of absorber defects and substrate defect in a single exposure. (a) SEM image of an area showing absorber defects in the vicinity of the alignment cross. Note that the cross cannot be seen under SEM. (b) SAL 601 resist image of the same area, showing the effect of the cross substrate defect and the absorber defects.

6.4. Conclusions

Results from this experiment show that 25 nm thick substrate defects of half the size of the minimum resolvable feature resulted in 15% linewidth variations on the resist image. Although not directly comparable to TEMPEST results, the results reported here demonstrated the printability of sub-resolution substrate defects in EUVL masks.

Current optical mask specifications require the elimination of all defects larger than 1/3 of the minimum feature size for conventional masks [16]. Printability studies for phase-shift masks indicate that phase defects of 1/7 of the minimum feature size may cause 10% linewidth variations [11]. The data from this study indicate that the printability of substrate defects in EUVL mask are comparable to defects on optical mask . However, the imaging system was operating at a reduced resolution because of misalignments in the optics, and the resulting phase front distortions may have partially concealed the effects of substrate defects. As a result, further printability studies at 0.1 μm resolution need to be performed to quantify the magnitude of the effects of substrate defects.

The inspection for substrate defects would require techniques sensitive to topographical features with heights of 100 Å or less. Preliminary investigation showed that substrate defects were difficult to detect by SEM operating in secondary electron imaging mode (SEI) and were more easily seen with phase contrast white light microscopy.

References

1. G. Arthur, and B. Martin, "Modelling the printability of sub-micron 5X reticle defects at I-line exposure wavelength," Microelectronic Engineering, 23, pages 167-170 (1994).

2. P. Canestrari, S. Carrera, G. Degiorgis, and V. Visentini, "Impact of reticle defects on submicron 5x lithography," *Integrated Circuit Metrology, Inspection and Process Control IV* (San Jose, CA, USA, 5-6 March, 1990), *SPIE Proceedings*, vol.

1261, W.H. Arnold ed., pages 225-237 (The International Society for Optical Engineering, Bellingham, WA, USA, 1990).

3. S.K. Dunbrack, A. Murray, C. Sauer, R.L. Lozes, J. Nistler, W.H. Arnold, D. Kyser, A. Minvielle, M. Preil, B. Singh, and M.K. Templeton, "Phase-shift mask technology: requirements for e-beam mask lithography," *Integrated Circuit Metrology, Inspection and Process Control V* (San Jose, CA, USA, 4-5 March 1991), *SPIE Proceedings*, vol. 1464, W.H. Arnold ed., pages 314-326 (The International Society for Optical Engineering, Bellingham, WA, USA, 1991).

4. T.Y. Fu, "Pattern design and tolerancing analysis of phase-shifting masks," BACUS News, 8(1), pages 1-8 (1992).

5. B.J. Grenon, K.D. Badger, and M.J. Trybendis, "Reticle defect sizing and printability," *11th Annual Symposium on Photomask Technology* (Sunnyvale, CA, USA, 25-27 Sept. 1991), *SPIE Proceedings*, vol. 1604, pages 179-195 (The International Society for Optical Engineering, Bellingham, WA, USA, 1991).

6. Y.M. Ham, I.B. Hur, Y.S. Kim, D.J. Ahn, Z. Cha, S.S. Choi, H. Kim J., and Y.J. Jeon, "Dependence of defects in optical lithography," Japanese Journal of Applied Physics, Part 1 (Regular Papers & Short Notes), **31**(12B), pages 4137-4142 (1992).

7. T. Kikuchi, K. Shigematsu, M. Tominaga, H. Maruyama, T. Furukawa, and I. Yanagida, "Effects of sub-half-micron mask defects on wafer images during VLSI circuit production," *Optical/Laser Microlithography II* (San Jose, CA, USA), *SPIE Proceedings*, vol. 1088, B.J. Lin ed., pages 48-57 (The International Society for Optical Engineering, Bellingham, WA, USA, 1989).

8. M. Kohno, N. Kodachi, K. Yajima, and S. Miura, "Subhalf micron stepper with a reticle monitor," *Optical/Laser Microlithography VI* (San Jose, CA, USA), *SPIE Proceedings*, vol. 1927, J.D. Cuthbert ed., pages 568-581 (The International Society for Optical Engineering, Bellingham, WA, USA, 1993).

9. R. Murphy, D. Flesberg, T. Reilly, and J. Reynolds, "The printability of particles on 5X reticles," *12th Annual BACUS Symposium* (San Jose, CA, USA),

SPIE Proceedings, vol. 1809, pages 146-157 (The Internatinal Society for Optical Engineering, Bellingham, WA, USA, 1992).

10. K.-D. Roth, W. Maurer, and C. Blasing-Bangert, "Metrology on phase shift masks," *Integrated Circuit Metrology, Inspection and Process Control VI* (San Jose, CA, USA, 9-11 March 1992), *SPIE Proceedings*, vol. 1673, M.T. Postek ed., pages 214-220 (The International Society for Optical Engineering, Bellingham, WA, USA, 1992).

11. R.J. Socha, A.R. Neureuther, and R. Singh, "Printability of phase-shift defects using a perturbational model," *13th Annual BACUS Symposium on Photomask Technology and Management, Proceedings* (San Jose, CA, USA), *SPIE Proceedings*, pages 277-287 (The International Society of Optical Engineering, Bellingham, WA, USA, 1994).

12. H. Watanabe, Y. Todokoro, and M. Inoue, "Detection and printability of shifter defects in phase-shifting masks," Japanese Journal of Applied Physics, Part 1 (Regular Papers & Short Notes), **30**(11B), pages 3016-3020 (1991).

13. H. Watanabe, E. Sugiura, T. Imoriya, Y. Todokoro, and M. Inoue, "Detection and printability of shifter defects in phase-shifting masks. II.Defocus characteristics," Japanese Journal of Applied Physics, Part 1 (Regular Papers & Short Notes), **31**(12B), pages 4155-4160 (1992).

14. J.N. Wiley, "Effect of stepper resolution on the printability of submicron 5X reticle defects," *Optical/Laser Microlithography II* (CA, USA), vol. 1088, pages 58-73 (The International Society of Optical Engineering, Bellingham, WA, USA, 1989).

15. J.N. Wiley, T.Y. Fu, T. Tanaka, S. Takeuchi, S. Aoyama, J. Miyazaki, and Y. Watakabe, "Phase shift mask pattern accuracy requirements and inspection technology," *Integrated Circuit Metrology, Inspection and Process Control V* (San Jose, CA, USA, 4-5 March 1991), *SPIE Proceedings*, vol. 1464, W.H. Arnold ed., pages 346-355 (The International Society for Optical Engineering, Bellingham, WA, USA, 1991).

16. J.N. Wiley, and J.A. Reynolds, "Device yield and reliability by specification of mask defects," Solid State Technology, (July), (1993).

17. L.S. Zubrick, "Detection and criticality of transmission variations on 5X reticles," BACUS News, 9(9), pages 1-9 (1993).

18. H. Kinoshita, K. Kurihara, Y. Ishii, and Y. Torii, "Soft x-ray reduction lithography using multilayer mirrors," Journal of Vacuum Science and Technology B, 7(6), pages 1648-1651 (1989).

19. H. Kinoshita, K. Kurihara, T. Mizota, T. Haga, Y. Torii, H. Takenaka, and Y. Ishii, "Soft x-ray reduction lithography using a reflection mask," *Soft x-ray projection lithography* (Monterey, CA), *OSA Proceedings*, vol. 12, J. Bokor ed., pages 11-15 (Optical Society of America, Washinton, D. C., 1991).

20. H. Kinoshita, K. Kurihara, T. Mizota, T. Haga, H. Takenaka, and Y. Torii, "Large-area, high-resolution pattern replication, by the use of a two-aspherical-mirror system," Applied Optics, 32(34), pages 7079-7083 (1993).

21. H. Kinoshita, "SXPL in Japan," *Soft X-ray projection lithography* (Monterey, CA, USA), *OSA Proceedings*, vol. 18, A.M. Hawryluk, and R.H. Stulen ed., pages 74-78 (Optical Society of America, Washington, D. C., USA, 1993).

22. K. Kurihara, H. Kinoshita, T. Mizota, T. Haga, and Y. Torii, "Two-mirror telecentric optics for soft x-ray reduction lithography," Journal of Vacuum Science and Technology B, 9(6), pages 3189-3192 (1991).

23. G.D. Kubiak, R.Q. Hwang, M.T. Schulberg, D.A. Tichenor, and K. Early, "Chemically amplified soft x-ray resists: sensitivity, resolution, and molecular desorption," Applied Optics, 32(34), pages 7036-7043 (1993).

24. G.D. Kubiak, E.M. Kneedler, R.Q. Hwang, M.T. Schulberg, and K.W. Berger, "Characterization of chemically amplified resists for soft x-ray projection lithography," Journal of Vacuum Science and Technology B, 10(6), pages 2593-2599 (1992).

Appendix A – Formulas for Bending Magnet Power Output

Power output from bending magnets in electron storage rings can be calculated using well-verified formulas [1],

$$\frac{dF_B}{d\theta} = \frac{\sqrt{3}}{2\pi}\alpha\gamma\frac{\Delta\omega}{\omega}\frac{I}{e}G_1(y) \qquad (1)$$

where,

F_B	=	photon flux (photons/sec)
θ	=	horizontal angle (rad.)
α	=	fine structure constant $= \frac{e^2}{2\varepsilon_o hc} \cong \frac{1}{137}$
γ	=	electron energy/mec2
ω	=	frequency of photon
I	=	storage ring current (Ampere)

$G_1(y)$ is given in terms of modified Bessel function of the second kind $K_{5/3}$,

$$G_1(y) = y\int_y^\infty K_{5/3}(y')dy' \qquad (2)$$

where,

y	=	ω/ω_c
ω_c	=	critical frequency of the storage ring, the frequency that divides the emitted power into two equal halves
	=	$\frac{3\gamma^3 c}{2\rho}$
ρ	=	radius of curvature of the electron trajectory
	=	3.3 E(GeV) B(T)
E	=	energy of the storage ring (eV)
B	=	magnetic field of the bending magnet (Tesla)

The flux per horizontal collection angle $dF_B/d\theta$ can be simplified to,

$$\frac{dF_B}{d\theta} = 2.457x10^{13} E(GeV) I(A) G_1(y), \qquad (3)$$

for units of photons/(sec-mrad- 0.1% BW).

Reference

1. K.J. Kim, *Characteristics of synchrotron radiation*, *Physics of Particle Accelerators*, M. Month and M. Dienes eds., (American Institute of Physics, New York, USA, p. 565 (1989).